POLITECNICO DI MILANO
DEPARTMENT OF MECHANICAL ENGINEERING
DOCTORAL PROGRAMME IN MECHANICAL ENGINEERING

USING BIO-INSPIRED DESIGN ELEMENTS IN THE FABRICATION OF CELLULAR MATERIALS WITH SPECIAL PROPERTIES AND FUNCTIONALITIES

Doctoral Dissertation of:
Mohammad J. Mirzaali

Supervisor:
Prof. L. M. Vergani
Prof. M. Strano

Tutor:
Prof. M. Vedani

The Chair of the Doctoral Program:
Prof. B. M. Colosimo

Year 2017 – cycle XXX

To my mother and sisters

Abstract

BIOMIMETICS is the study of biological substances with the aim of synthesizing and imitating similar elements, structures, systems and models in the fabrication of advanced artificial materials to achieve new properties.

Biological materials combine different design elements such as hierarchies at different length-scales, heterogeneities, functional gradient, randomness, cellular structures, specific geometries and so forth. Their composition also consists of two primary solid and soft phases. All these elements are combined in natural substances and result in a wide range of mechanical properties and functions.

In this thesis, I implemented, modeled and tested some of these essential design elements, in particular randomness, functional gradient and auxetic shapes of microstructures in the construction of bio-inspired materials.

New advanced materials were aimed at different mechanical or functional properties:

- enhanced directional strength as an imitation of trabecular bones;
- tailored elastic properties (elastic modulus and Poisson's ratio) using random design of unit cells;
- predictability of final complex shapes of materials under mechanical loading by rational design of geometrical features;
- functionalized internal surfaces of 3D cellular materials.

To reach these goals, we adopted different production techniques, such as foaming process through the powder route, additive manufacturing and crumpling.

Summary

Building blocks of cellular biological materials are mainly limited to few numbers of biopolymers (protein and sugar-based polymers) as the soft phase, minerals and ions as the hard phase and cross-linking agent to integrate these materials. In addition, there is limited amount of geometrical, morphological and topological arrangements in the microstructure of natural substances also known as essential design elements. Some of the most fundamental design elements are functionally gradient, randomness and multiple length-scale hierarchies at different length levels. Besides, particular shapes can be observed in the biological materials such as tabular, circular, honeycomb or re-entrant forms.

Despite these limited number of variations in material constituents and microstructural organizations in nature, biological materials offer a wide range of mechanical and functional properties as a result of proper, smart and optimized combination of chemical composition and microstructural design features to satisfy specific functions and design motifs.

Modern engineering materials with specific functionality and properties have always been on demand for various medical and industrial applications. Learning from nature, via biomimetics, has still been considered as a powerful tool to understand fundamental characteristics responsible for their attractive properties and functionalities. This has led to the fabrication of advanced engineering materials through the history. Biomimetics approaches aim to study biological substances and synthesize and imitate similar structure/ elements, systems and models of nature in order to fabricate advanced artificial human-made products with particular functionalities and properties. To mimic these unique features in a synthetic material, it is essential to implement proper com-

binations of existing manufacturing processes. However, to date there is no unique manufacturing method that can merge all these design features such as multi-scaling, heterogeneity, anisotropy, gradient, and hierarchy in *de-novo* materials. Therefore, development of new manufacturing methods for such an implementation is of high interest.

Recently, due to the new development in manufacturing techniques, studies related to the creation of bio-inspired materials have gained a numerous deal of attention. These needs are appreciated by scientist and engineers working in the area of material science, mechanics, architecture, and biology. Improving mechanical properties and functionalities have always been regarded by material scientists, mechanical engineers, and architects because of its applicability in industry. Bio-inspiration is also crucial for the design of new scaffolds, and (patient-specific) implants as it is required to accurately mimic the microstructure of tissues in order to have appropriate tissue regeneration.

Within different studies in this thesis, we aimed to take into account the most important design elements in natural materials, i.e., functionally gradient, randomness together with special shapes found in natures and implement those features in the fabrication of new advanced materials. In each study, we targeted certain mechanical or functional properties using the current manufacturing techniques. Different studies in this thesis are summarized as following:

- In chapter 1, we reviewed the state-of-the-art of bio-inspiration in material science and engineering. We also reviewed some of the key design elements in natural materials and provided few examples of the previous works on this area. A brief summary of outline of the thesis, and summarizing the content of other chapters are also provided at the end of this part. All materials in chapters 2 to 5 are taken from published documents in peer-reviewed journals.

- In chapter 2, we investigate the application of conventional foaming processes in the production of new closed-cell aluminum foams which their microstructures are mimicked to the ones of microstructures of trabecular bone. For that aim, we modified the current technique in order to design, manufacture and test two different types of bone-inspired aluminum closed cell foams. We also compared the microstructural feature and mechanical properties of that bone-inspired aluminum closed cell foams with bone samples.

- In chapter 3, we introduced patterned randomness as a strategy for independent tailoring of the elastic properties of soft metamaterials, i. e. the elastic modulus and Poisson's ratio. As the randomness is one the features that can be found in

the biological substances, the results of this study show how randomness in general and patterned randomness, in particular, can be served as design strategies to reach various mechanical properties in soft mechanical metamaterials, i. e. elastic modulus and Poisson's ratio. For this goal, we designed, tested and manufactured several samples and computational models to predict the topology-property relationship in a wider range. For the manufacturing of these structures, we used in-direct manufacturing technique.

- In chapter 4, we introduced functional gradient in soft mechanical metamaterials in order to predict predefined boundaries under mechanical stimuli. For this purpose, we designed, manufactured and tested few prototypes which later have been used for the validation of computational models. Then, we used computational results to predict pre-defined random shapes using forward-maps approaches. We also showed how these materials can be used for the approximation of boundaries of real objects.

- In chapter 5, we studied physics of crumpling of porous sheets. We proposed crumpling as a fast and easy fabrication technique for manufacturing crumpled-based bio-materials due to their robust mechanical properties. We also compared the process of crumpling of sheets without a hole, with the one with 2D porosity and investigated how holes can affect this process. The method of crumpling can also be considered as a powerful method for converting 2D surface functionalization to 3D.

- In chapter 6, concluding remarks are presented and few suggestions for future works are provided.

Acknowledgment

I did a Ph.D. for the pleasure of finding things out and proposing new solutions to the current challenges. I hope, in the near future, these results can be used in the real applications and end up to a more comfortable, relaxing and happier life for individuals. I have to admit that this thesis project changed my view point toward Nature which is personally highly regarded.

Now, I would like to take this space and appreciate the people who assisted me in this period. First, I express my most profound gratitude to my supervisors, Prof. Laura Vergani, and Prof. Matteo Strano for giving me the opportunity to do the Ph.D. at the Department of Mechanical Engineering, Politecnico di Milano. I won't forget your support and trust. Furthermore, I would like to thank Prof. Amir A. Zadpoor who warmly hosted me at his group, at the Department of Biomechanical Engineering, Technical University of Delft. Working with you was a great pleasure to me, and I learned a lot from you. You showed me how simple ideas could lead to advance discoveries. Thanks for all inspirations, guidance and motivations; Next, I sincerely thank Prof. Pasquale Vena, Department of Chemistry, Materials and Chemical Engineering Giulio Natta, Politecnico di Milano, who was like a friend and always available for me. Your kind advice and comments helped me so much in this period. I would also like to thank my colleagues Dr. Flavia Libonati at Polimi, and Dr. Shahram Janbaz, at TU Delft intensely for their support, discussion, and assistance within these years. I enjoyed working with you all. I would like to thank my external reviewers, Prof. John Banhart and Prof. Zoran Ren for evaluating my thesis.

I would like to show my gratitude to my colleagues at Polimi, Sara, Federico, Klara, Chiara and Pietro and other floormates. I also express my appreciation to my colleagues at TU Delft, Francois, Nazli, Sebastian, Vahid, Ingmar and other floormates for being

with me. I will miss you all. My thanks also go to the technical staff of the Department of Mechanical Engineering of Politecnico di Milano, and Biomechanical Engineering Department of TU Delft who helped me with testing machines and laboratory tools. Many thanks to Davide Ferrario (Polimi), Isabelle van Dongen, Maike Edens and Alba Herranz Delanava (TU Delft), the MSc students who assisted me with various projects. I would like to thank all my friends in Iran, Milan, Delft as well for their endless support and encouragement.

The most important thanks to my lovely mother and sisters for their warm support and for tolerating my physical absence during the last three years. Words are not enough to express my love for you.

Contents

CHAPTER 1

Biomimetics in Cellular Materials

1.1 Introduction

The terms 'Biomimetics' and 'biomimicry' drive from two Ancient Greek words of 'bios' and 'mimesis' meaning 'life' and 'imitation'. Biomimetics or biomimicry is the study of biological substances and materials for the purpose of synthesizing and imitating similar structures/ elements, systems, and models of nature in the fabrication of artificial human-made products [1].

Natural materials contain well-adapted living organisms and materials that satisfy their functionality. Understanding the biological solution at macro and nanoscales by biomimetics have been led to new technologies and new advanced materials with enhanced properties and functionalities through the history. Humans, all through our existence, have looked at nature to find an answer to problems. Nature has solved engineering problems such as self-healing abilities, environmental exposure tolerance, and resistance, self-assembly, etc. Those solutions can be considered as a source of inspiration for the production of engineering materials.

Material constituents of biological substances are limited into soft phase (mainly bio-polymer proteins), hard phase (minerals) and other cross-linking agents [2]. Interestingly, a combination of these limited number of materials results in a wide range of materials properties and functionalities. In addition to the chemical composition, there

are typical geometrical, topological and morphological organizations in the microstructure of biological materials [3, 4]. Moreover, particular shapes can be observed in the biological materials such as tabular, circular, honeycomb or re-entrant forms and these specific shapes can appear in a biological structure [5]. Combination of these architectural and compositional properties can lead to the design of advanced materials with enhanced mechanical or functional properties.

The primary objective of this thesis is to find out the most essential design elements and features in the natural design from one hand and implement them in the design of artificial materials from the other hand. Such an implementation needs specific and appropriate manufacturing tools. Therefore, we used the current manufacturing techniques such as Additive manufacturing (AM) or conventional foaming techniques for implementation of such design elements. In addition, we aimed to propose different manufacturing processes that can be used as a platform for the fabrication of bio-inspired materials. Implementation of these natural design elements resulted in materials with different mechanical, structural and functional properties that will be discussed in detail in different chapters of this thesis.

1.2 History

The initial use of biomimicry design in the construction of human-made products might come back to 15th and 16th centuries when Leonardo da Vinci (1452-1519) observed anatomy and flying systems of birds [6]. Later on, based on the inspiration from pigeons, Wright Brothers (1867-1912) had made the first aircraft's prototype [7, 8].

The American biophysics and polymath Otto Schmitt developed the concept of 'biomimetics' during 1950s [1], which he attempted to engineer a device to replicate the biological system of nerve propagation. He defined this term as [9]: 'The study of the formation, structure, or function of biologically produced substances and materials (as enzymes or silk) and biological mechanisms and processes (as protein synthesis or photosynthesis) especially to synthesize similar products by artificial mechanisms which mimic natural ones.' The term 'biomimicry' was popularized by scientist and author Jenine Benyus where she proposed looking to Nature as a 'Model, Measure, and Mentor' [10].

Biomimicry shaped new materials and structures in different fields such as in energy, architecture, transportation, agriculture, medicine, and communication [10]. It has also led to the creation and innovation of new materials and technologies within the past decades. A swimsuit based on the dermal denticles in the skin of sharks that mimics the antimicrobial film [11], Beaver-inspired wetsuits [12], velcro straps [13], bullet trains inspired by Kingfisher birds [14], harvesting water from the air similar to the Stenocara

beetle [15], shock-resistant instruments by mimicking the skull of the woodpecker [16], artificial soft materials with the ability of camouflaging similar to cephalopods [17] are few examples of such kind.

1.3 Structural Design Elements in Biological Materials

Natural materials provide intelligent answers, optimized solutions and a rich source of inspiration to engineering requests as they are designed to satisfy a specific function [2, 4, 18–20]. These materials contain two main building blocks at different length scales from nano- to mesoscales. These building blocks are limited to hard (mineral bio-materials) and soft (polymeric bio-materials such as proteins) phases, which produce a composite biological materials [4,8]. The hierarchical self-assembly of nano- to macro-structural organization is resulted by means of a well adaptation [4,20,21]. In addition, living organisms show an ingenious functional gradient and heterogeneities [4, 20, 22]. Therefore, understanding the key design features in natural substances from one hand, and studying the role of microstructure at different length scales and its relation to the macroscopic ones from the other hand can provide extensive knowledge to design new engineering products with different applications and functionalities. Those synthetic materials are of high interests in the engineering and medical applications.

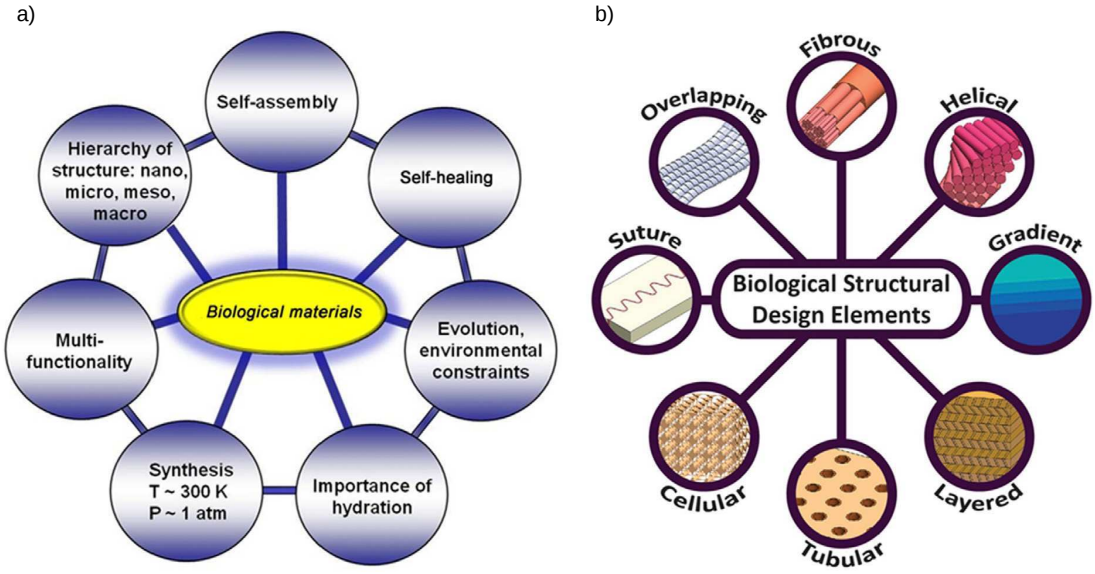

Figure 1.1: *a) Seven unique characteristics of biological substances, b) Eight most common structural design elements in biological materials. Adopted from [4].*

In a recent review by Liu et al., 2017 [4], the unique characteristics and common structural design elements in biological substances are summarized as (Figure 1.1): i) self-assembly, ii) self-healing, iii) evolutionary and environmental constraint, iv) the

importance of hydration, v) mild synthesis conditions (mostly at ~$300K$ temperature and ~1 atm pressure, vi) multi-functionality, vii) hierarchy of microstructures at nano, micro, meso, and macro levels [4, 22], where cannot be found in synthetic materials. Design motifs such as gradient, cellular, helical, layered units are the most common structural design elements in the natural materials (Figure 1.1). These structural units combine to each other through the evolution to satisfy the particular functionalities of the specific biological materials.

Functionally graded materials (FGMs) and heterogeneity are the most essential design features in the natural materials. These occur through the gradient in the material properties of the natural materials and the structural characteristics of them (Figure 1.2).

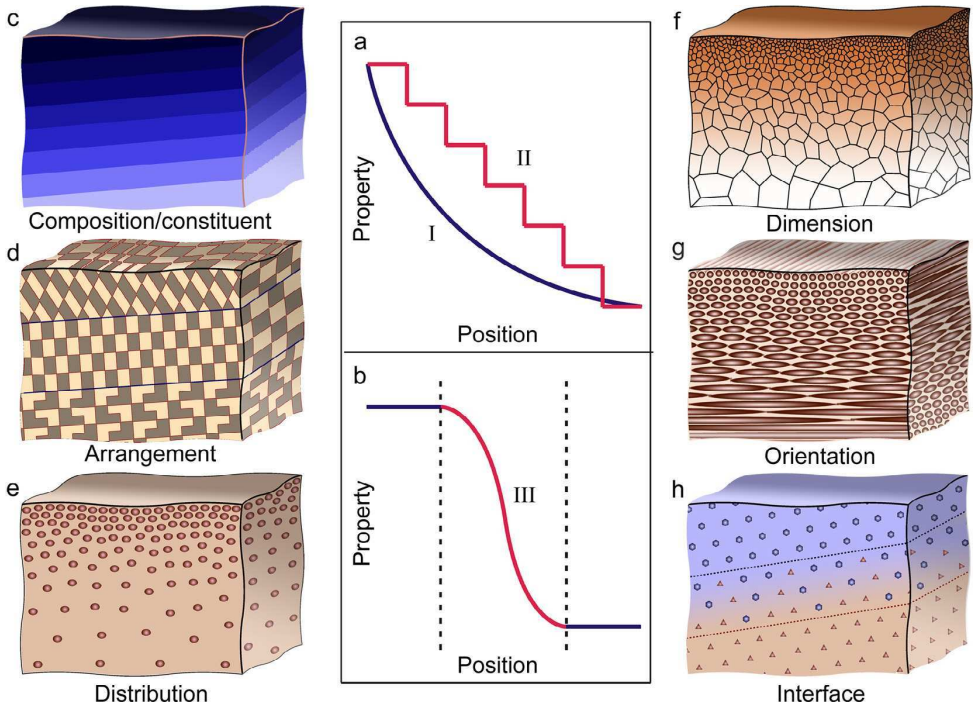

Figure 1.2: *Different forms of the gradient in the biological materials. a) Changes in the local properties can be reached either gradually (I) or step-wise (II). b) Local properties can also change at the interfaces of two dissimilar components such as in the tendon-bone attachment. The gradient in the natural materials can be either by means of chemical or material changes (c) of in the structure of the biological substances (d-g). The change in the structure can be divided via (d) arrangement, (e) distribution, (f) dimension and (g) orientation. Such gradient can also be seen in the interface of a biological substance (h). Adopted from [4, 22].*

The gradient in the chemical composition can follow different patterns and trends from a spatial distribution of the chemical compositions within the material's volume to the gradient of material composition at the interfaces regions where two dissimilar materials meet each other, e. g. tendon-to-bone attachment [23, 24] (Figure 1.3a),

spider web [8], anchoring tooth in bone [25] (Figure 1.3b) and molluscs [26]. The gradients in the chemical composition can be generated via the difference in the degree of mineralization (for example in crayfish mandibles [27]), ion contents gradient (for instance in spider fangs [28]) and degree of hydration (for example in squid beak [29, 30]).

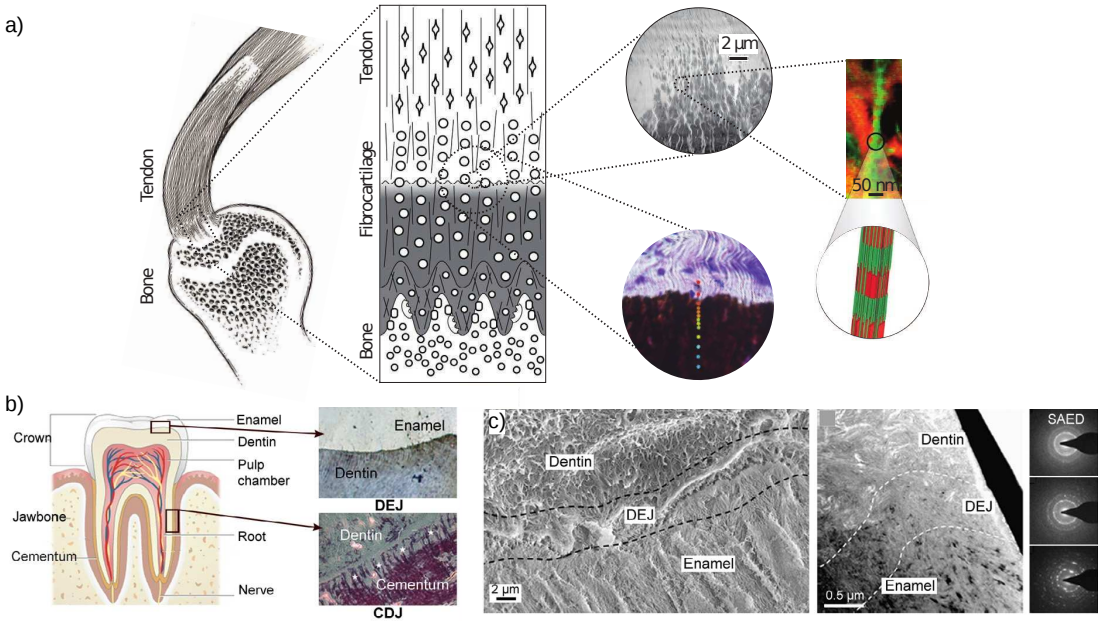

Figure 1.3: *Examples of gradient in the chemical composition of natural materials a) Tendon-bone interface region consists of different distinct zones, i.e., tendon, fibrocartilaginous transitional zone (uncalcified fibrocartilage and mineralized fibrocartilage) and bone [23, 24]. This interface has been shown to be highly heterogeneous in the lateral direction and angle-dependent Seven unique characteristics of biological substances (Adopted from [24]), b) Graded interfaces in the tooth which contains, the dentin-enamel junction (DEJ) and cementum-dentin junction (CDJ). The degree of mineralization, the orientation of collagen fibril, and morphology of mineral crystals have been shown to be different between the dentin and enamel [4, 31]. Adopted from [4].*

The changes in the structural features of natural materials also show various patterns. These alterations in the structural features produce materials with enhanced-performance, site-specific properties even without a change in the chemical compositions [4]. Some of these structural characteristics happen through arrangement, distribution, dimensions, and orientation or a combination of them. For example, the microstructure can be organized either in a structured or random manner. Alligator osteoderm is composed of four different regions with different structural organizations [32] (Figure 1.4a), while wheat awn is an example that shows well aligned fibrils in the cap and random structures at the ridge [33] (Figure 1.4b). Transition region from inner trabecular bone to the cortical bone in the elk antler and also change in the density of

vascular bundles in bamboo stems [34, 35] (Figure 1.4c) are examples of continuous degradation distribution of porosity in a biological material [3, 36].

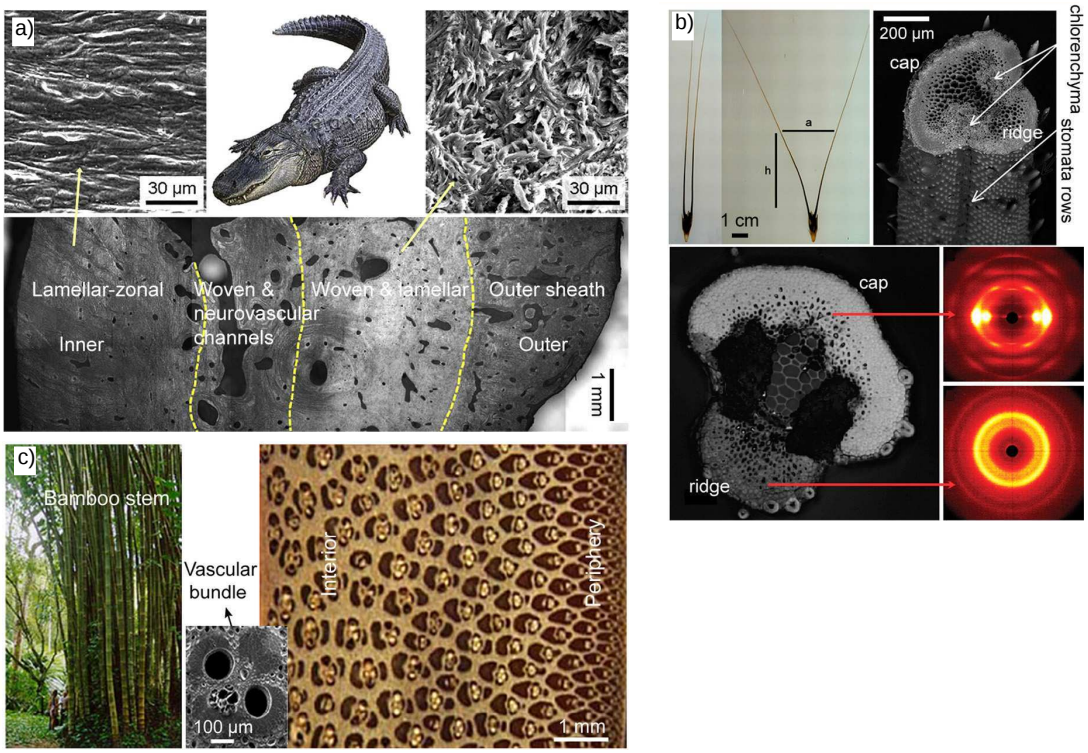

Figure 1.4: *Examples of gradient in the microstructural arrangement of natural materials a) Four various regions in alligator osteoderm [32], b) Random organization of microstructure at the ridge part of wheat awn, while at the cap cellulose fibrils are well organized along the longitudinal axis. This organization leads to non-uniform expansion at different regions when it is exposed to daily humidity cycles [33], c) Gradient in the density of vascular bundles in bamboo stems which increases from interior to peripheral [34, 35]. Adopted from [4].*

In some biological substances such as bone and tooth, a mixture of diverse chemical and structural gradient exists. It means in these materials multiple length-scales constituents with hierarchical structures are organized [3, 4, 19, 37–39].

Such combination of material and structural gradient in Nature are optimized with respect to the specific function of biological materials [4, 19]. These functions can be mechanical, non-mechanical and interfacial strengthening and toughening. For example, bones and plant stems have evolved and optimized due to their mechanical role as a load-bearing or support element in the structure [4].

Among different structural elements in Nature, we considered randomness, microstructural organization, orientation, arrangement, and distribution as the most critical natural design elements (also called as functional gradient) and try to implement them in the artificial designs. Such an implementation will be discussed in brief in Sec-

tion 1.5, and in detail in the following chapters.

1.3.1 Cellular Metamaterials

Cellular solid materials can be found in natural structural elements such as bone, cork, and wood. These materials can be used as a source of inspiration for the creation of human-made cellular solids with different engineering applications that require lightweight, customized stiffness, impact resistance and energy absorbance capability. Numerous investigations have been focused on the mechanical response of periodic and non-periodic cellular solids in 2D and 3D under various loading configurations [40, 41].

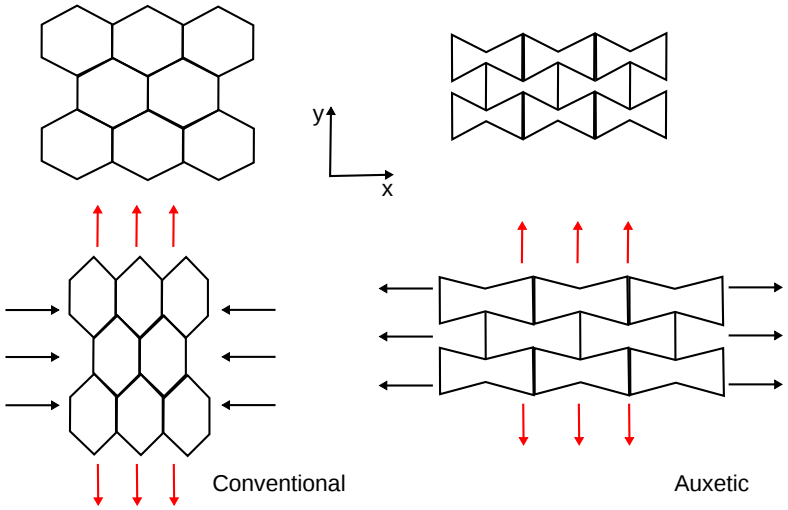

Figure 1.5: *Two-dimensional unit cells under tension loading in y-direction. Left: Conventional honeycomb structure, Right: Auxetic Lattice structure [42, 43].*

Mechanical behavior of the cellular metamaterial highly depends on the geometry of the unit cells at small-scales rather than their chemical compositions [44, 45]. By changing the geometry of the unit cell in cellular material, one can create materials with properties that cannot be found in nature. A tunable positive- negative Poisson's ratio unit cells is an example of these materials [46–48].

One of the emerging cellular materials is auxetic material. Auxetic cellular materials belong to the class of cellular metamaterials with negative Poisson's ratio (NPR). These materials show a contrary behavior of bulk material as they transversely contract under longitudinal compression and transversely expand under longitudinal extension (Figure 1.5). Auxetic materials can be found in nature such as cadmium [49] and single crystals of arsenic [50], or in biology substances for instance in load-bearing cancellous (trabecular) bone of human femur/ tibia [51,52] or form of skin [53,54]. Auxetic materials have various potential applications as an implant in biomedical engineerings such

as artificial discs and scaffold [52, 55], surgical implants with pull out resistant [42], artificial blood and stent designs or as sensors and actuators, air and mass filters, and fastener in aerospace engineering [56, 57]. Recently, accordion-like honeycomb structures similar to heart's cells was implemented as a new strategy in design of tissue scaffolds in bioengineering [58, 59].

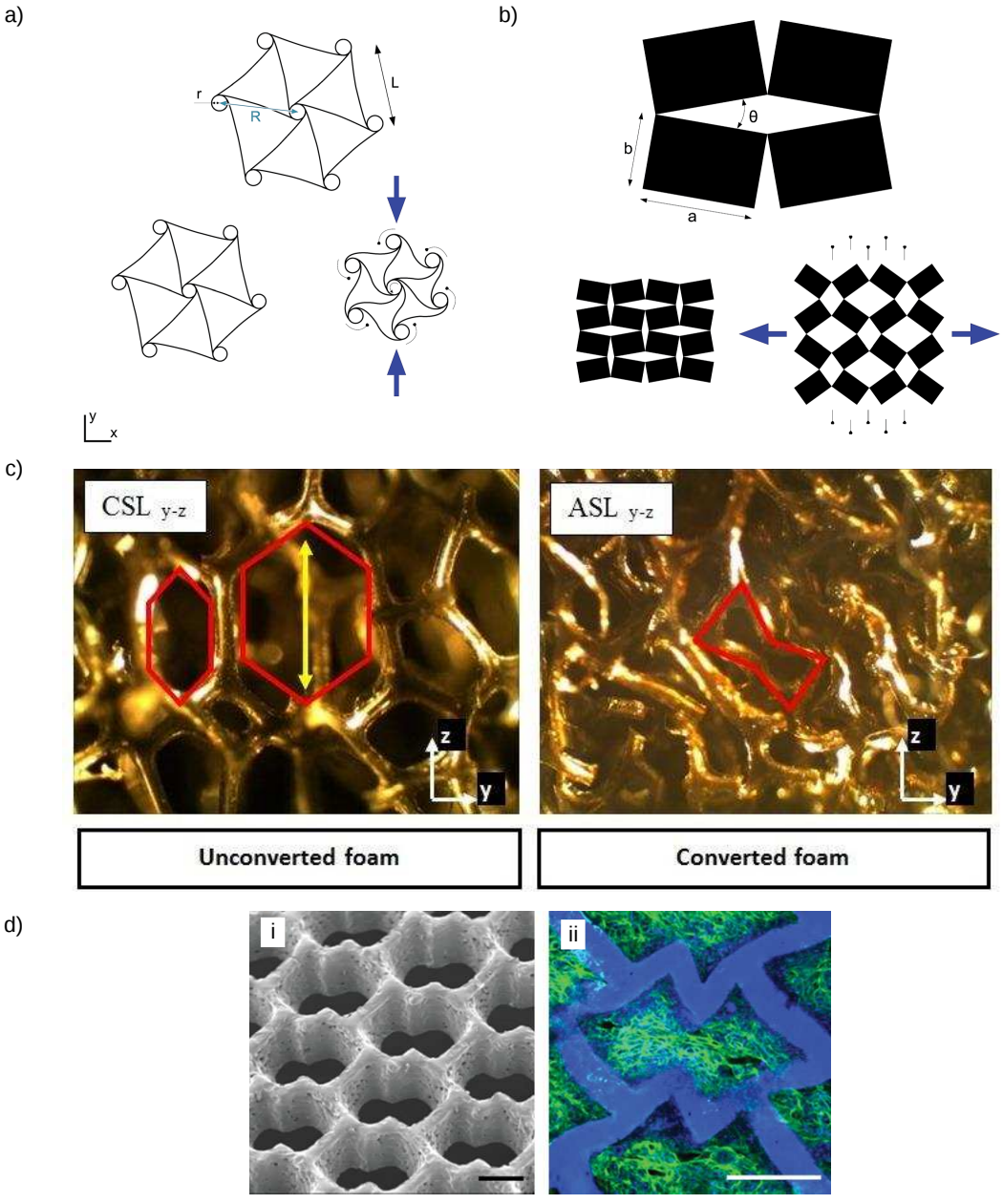

Figure 1.6: *Different forms of auxetic unit cells, a) hexachiral unit cells [60], b) rotating rigid rectangle structures [60, 61], c) micrographs of converted and unconverted foam. Detection of regular and re-entrant honeycomb structure in foam materials [55]. c) design of accordion-like honeycomb scaffold used for myocardial tissue engineering [58, 59].*

Auxetic materials exist in different shapes [45, 62]. Some of the most well-known auxetic materials proposed within past years are: re-entrant honeycomb structures [63], chiral structures [60] (Figure 1.6a), rotating rigid unit [61] (Figure 1.6b), angle-ply laminates [64], origami-like structures [65] and foam materials [66] (Figure 1.6c). This shows how topological design of these structures at microscale can change the properties at the macroscopic level. General application of NPR materials are mainly based on their unusual (negative) Poisson's ratio [63, 67], superior toughness, resilience, and shear resistance [43], acoustic properties [66], negative compressibility [68], improved impact performance [69], and snapping deformations [70]. More information about different types of auxetic lattice structures and their applications can be found in the a recent review was written by Zadpoor et al. [45, 60].

Functionally graded auxetic (FGA) structures [46, 71], and porous biomaterials with graded/gradient porosity and pore size have also been developed recently [72] to be used as a biomedical implant. One of the potential approaches to implementing the FGA material is in total hip replacement stem [55, 73] or mandible implant [74]. The reason is that the mechanical properties of this structures can be tuned efficiently. In addition, from the microstructures of these materials can be designed in a way that mimics the microstructures of bones in the case of the design of a bone implant [55].

FGA materials can be fabricated using Additive Manufacturing (AM) techniques [66, 75]. These techniques allow a rapid manufacturing of complex cellular structures with controllable architectures made of metals or polymers.

1.4 Bio-Inspired Materials

In the past, different structural features in the biological materials have been used to design synthetic materials. That mimicking has not only led to manufacturing new artificial materials, but also new fabrication techniques. In section 1.4.1, we will focus on the bone as a complex biological substance and a potential candidate for the biomimetic purposes. Therefore, we first provide a summary of different structural and compositional features in bones and different methods in the investigation of microstructural features in bone. Then, in section 1.4.2, we review few fabrication techniques developed and used for the production of mainly bone-inspired materials.

1.4.1 Bone Composition, Structural and Mechanical Properties

Bone is one of the lightweight biological substances with a unique combination of strength and toughness and a sophisticated hierarchical architecture. The hierarchical structural features and compositions of bone are locally optimized from nano to

mesoscales to improve its mechanical function [4]. For this reason, it can be considered as a smart natural material used for the design of synthetic ones [76, 77].

Bone Composition

Bone is a composite material made of [20, 78]: (i) a mineral or hard phase (carbonated hydroxyapatite) (50-60 wt. %), which gives the bone its rigidity, (ii) a protein or soft phase (mainly type-I collagen) (30-40 wt. %), which improves its fracture resistance and (iii) water (10-20 wt. %). This makes the structure of the bone to be hierarchical at different length scales. At the nano-scale, bone consists of the nanoparticle of hydroxyapatite. Mineral platelets together with collagen molecules (with the thickness of 2 nm to 4 nm and several tens of nanometers in the other dimensions) create mineralized collagen fibrils at a scale of approximately 100 nm. These mineralized collagen fibrils then form fiber bundles at the level of a micrometer. The fiber bundles finally make lamellae which roughly have constant mineral content within different part of the bone [2, 20, 78] (Figure 1.7).

At the macroscopic level, bone can be divided into two main parts: trabecular or cancellous bone and cortical bone (Figure 1.7). Cortical bone shapes the hard outer shell or cortex and trabecular forms the spongy inner part of the bone. In particular, trabecular bone can be found near the articulating ends of the long bone, such as the femur or tibia. They may also be found to fill the interior of short bones and flat bones or bones with irregular shapes, such as vertebrae, pelvis, and sternum [79]. The change from trabecular (interior) to cortical (exterior) part of the bone is via a transition of structural arrangement with an increase in the bone density [4].

The relatively high amount of trabecular bone adjacent to the joints through which large forces are transmitted suggests that it plays a vital role in preserving the mechanical integrity of the compound joint and bone as a whole. In addition, optimization of the micro- structure of the trabecular network eventuates to a material with optimal strength and minimal mass [81].

The cortical bone is formed of concentric bone lamellae arranged around blood vessels creating osteons and interstitial areas [82]. Cortical bone has a porosity of 5-15 % oriented along the osteon direction [83, 84], called Haversian canal. Osteons are separated from the surrounding tissue by a cement interface [85] (with the thickness of 1 to 5 μm [81, 85].

Important Structural Features of Bone

Trabecular bones appear as a highly porous cellular solid composing of a lamellar structure arranged in a not well-organized pattern. They are made up of a network of rods

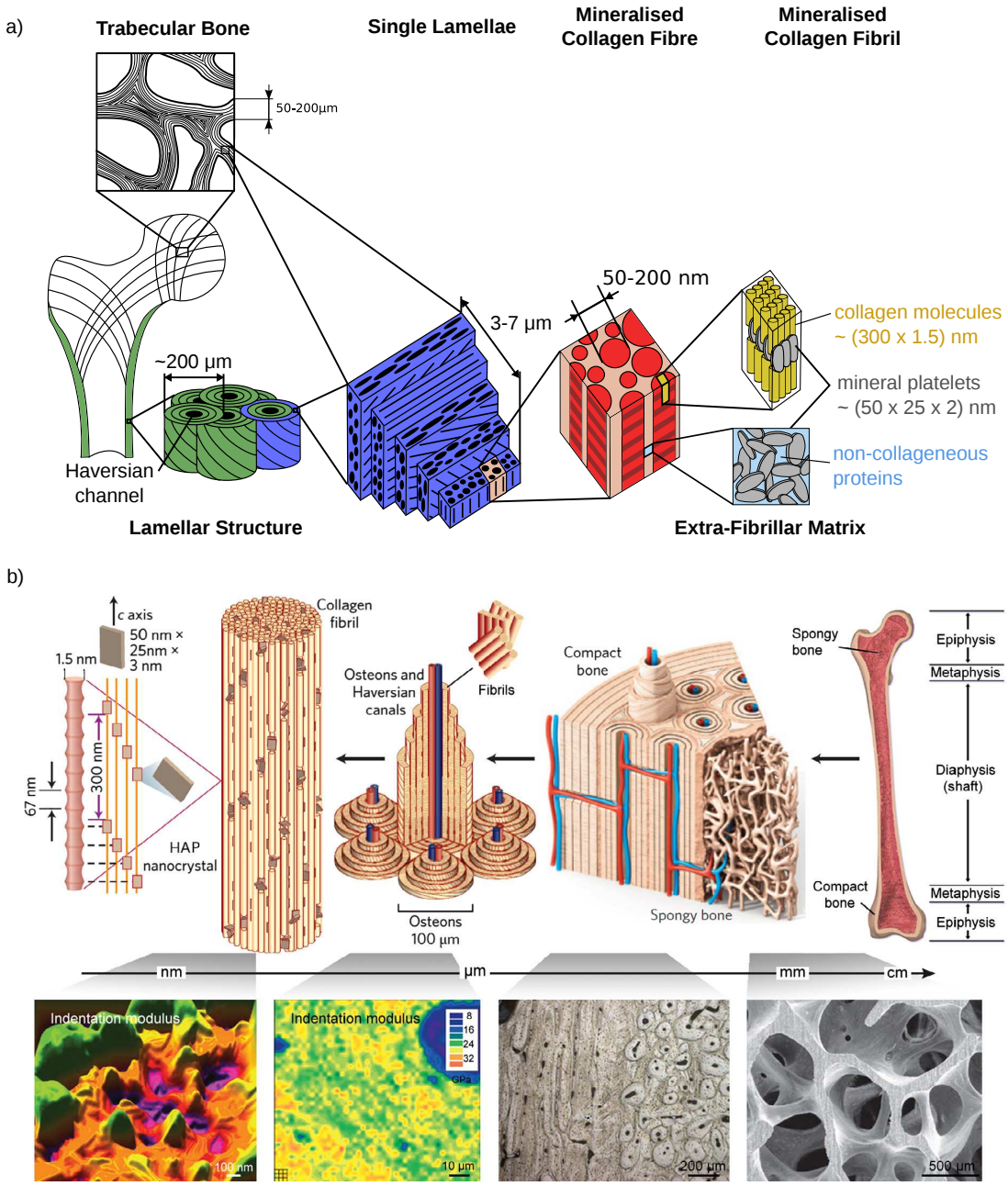

Figure 1.7: *Microstructure of bone: (a) consisting of Lamellar Structure and Extra-Fibrillar Matrix (Adopted from [80]), (b) in different length-scales from nano- to mesoscale (Adopted from [4]). It shows the hierarchy and gradients in the structure of bone. The density of bone radially increases from the interior cancellous (trabecular) to the exterior cortical bone.*

and plates, called trabeculae, with the thickness of about 100 to 300 μm interspersed with large marrow spaces [86]. Trabecular bones exhibit heterogeneity, where their shapes, dimensions, arrangement are different within skeletal sites and between skeletal sites [87, 88]. For instance, trabecular in human vertebral body tends to be more

rodlike, whereas trabecular in the proximal tibia consists almost entirely of plates (Figure 1.8).

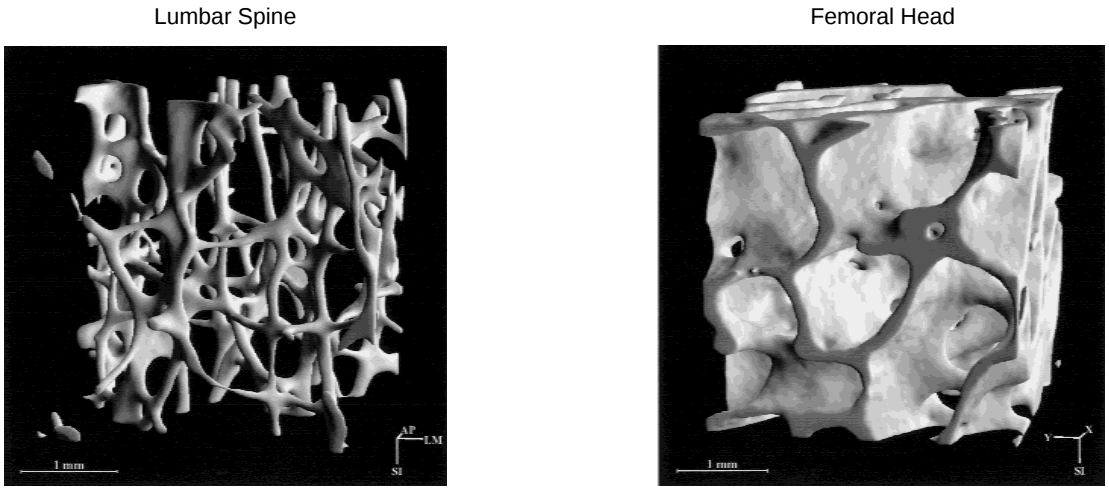

Figure 1.8: *Typical trabecular bone structures of the femoral head with plate-like structure and the lumbar spine with rod-like structure. (Adopted from [88]).*

This heterogeneity results in a vast difference in the mechanical properties such as elastic modulus and strength [79, 89]. Trabecular bone also reveals anisotropy since its microstructures are typically oriented along the direction of maximum strength and maximum mechanical stiffness based on the Wolff's law [79, 90, 91]. Bone structure adaptation is a result of mechanical stimuli and results in an anisotropy of the mechanical properties and microstructural arrangements of bone.

To measure the intrinsic anisotropic material behavior of the trabecular bone, it is required to perform mechanical testing along the principal coordinate system of trabecular bone [92] and minimize errors due to the possible side effects during the testing [93]. Therefore it is essential to quantify the principal structural directions of the trabecular bone. In the past, Mean Intercept Length (MIL) [94], have been used to measure these principal structural directions. The MIL is a tensor to estimate the orientation and anisotropy of microstructures from 2D or 3D binary images. The MIL is defined as the mean of distance between change from one phase to another phase in the binary image. To measure this distance, a set of parallel lines will pass through the image at different angles ranging from 0 to 180. In 2D, the MIL tensor can be obtained by fitting an ellipse to polar plots of the MIL which is also known as rose diagrams [95]. It was approximated by an ellipsoid in three-dimension [96], and led to the definition of a positive definite second-order fabric tensor that characterizes the degree of anisotropy of the trabecular's structure [97]. In addition, based on the general theory developed by Cowin, fabric tensor, which is the inverse of MIL tensor, has been applied to measure

the local structural anisotropy [98].

Fabric tensor is defined as:

$$\mathbf{M} = \sum_{i=1}^{3} m_i \mathbf{M}_i = \sum_{i=1}^{3} m_i (\mathbf{m}_i \otimes \mathbf{m}_i). \tag{1.1}$$

Where m_i are the positive eigenvalues and the $\mathbf{m}_i$ are the corresponding normalized eigenvectors. $\mathbf{M}$ is normed to $tr(\mathbf{M}) = 3$, which ensures that fabric is independent of volume fraction. The three eigenvectors of $\mathbf{M}$ represent the principal axes of material symmetry, which also correspond to the principal orientations of trabeculae. Based on the different eigenvalues, fabric can be isotropic, transversely isotropic or orthotropic [99]. The degree of anisotropy (DA) can be defined as the ratio of the largest over the smallest fabric eigenvalue [96].

Non-destructive X-ray-based imaging, such as micro-computed tomography (μCT) and other high-resolution imaging techniques have been utilized to represent the three-dimensional structure of the trabecular and cortical bone, and consequently, are used to estimate the orientation distribution of the trabecular bone [100] (Figure 1.8).

Different morphological parameters can be obtained from (μCT) imaging such as relative density ($\frac{BV}{TV}$), Trabecular Thickness ($Tb.Th$), Trabecular Spacing ($Tb.Sp.$), and Structural Material Index (SMI). Relative density shows the relative amount of bone in a total volume of interest. Trabecular Thickness ($Tb.Th$) is defined by filling maximal spheres into the structure with the distance transformation [101]. It shows the thickness of each trabeculae in the structure. Trabecular Spacing shows the maximum sphere that can be filled within the trabeculae. The Structure Model Index (SMI) is an estimation of the plate-rod characteristic of the structure [102]. For an ideal plate and rod structure, the SMI value is 0 and 3, respectively. These morphological features of the trabecular bone are sorted in Table 1.1.

Mechanical Properties of Bone

Trabecular bone shows an asymmetric behavior in tension and compression loading (Table 1.2). The elastic modulus of the trabecular bone is 20 % to 30 % less than the cortical one [103] (Table 1.2). It yields in compression at a strain of approximately 1 %, after which it can sustain large deformations (up to 50 %) while still maintaining its load-carrying capacity [104]. Trabecular bone can absorb substantial energy on mechanical failure [79]. However, ultimate strain in trabecular bone is constant [105], suggesting a biological control mechanism targeted toward apparent strains [79]. It also displays time-dependent behavior and visco-plasticity [106], as well as damage susceptibility during cyclic loading. Damage accumulation mechanism under different loading modes and directions in trabecular [107], and cortical [108] bones are discussed,

Table 1.1: *Morphology of trabecular bone in different anatomical locations. Mean ± standard deviation are presented in this table.*

Anatomical Loacation	BV/TV [%]	Tb.Th [µm]	SMI	DA	Method	Reference
Iliac crest	11.5 ± 1.6	-	-	-	Histology	[87]
Iliac crest	15.6 ± 5.4	151 ± 27	1.51 ± 0.61	1.49 ± 0.18	µCT scan	[88]
Femoral neck	15.8 ± 1.6	-	-	-	Histology	[87]
Femoral neck	26.1 ± 7.8	194 ± 33	0.41 ± 0.68	1.68 ± 0.18	µCT scan	[88]
Lumbar spine	8.3 ± 0.8	-	-	-	Histology	[87]
Second lumbar spine	8.3 ± 2.4	122 ± 19	2.13 ± 0.35	1.42 ± 0.16	µCT scan	[88]
fourth lumbar spine	8.7 ± 3.3	139 ± 28	2.12 ± 0.36	1.51 ± 0.16	µCT scan	[88]
Calcaneus	15.4 ± 2.0	-	-	-	Histology	[87]
Calcaneus	12.0 ± 3.5	129 ± 18	1.76 ± 0.36	1.75 ± 0.15	µCT scan	[88]
Intertrochanderic	10.2 ± 1.2	-	-	-	Histology	[87]

and different aspects of this mechanism have been studied.

In Figure 1.9 typical stress-strain curves for trabecular bone is presented. As it can be observed from the curve, three steps happen during the compressive loading; linear elastic deformation due to elastic cell bending till yielding causes collapse of the cell walls, as the load increases a constant stress plateau occurs, which is due to progressive cell wall damage, breakage and buckling of the cells and produces an inelastic section. Finally, a densification occurs as cells collapse and contact each others resulting in a steep stiffness increase [109, 110].

Mechanical properties of trabecular [97] and cortical bone are highly correlated to

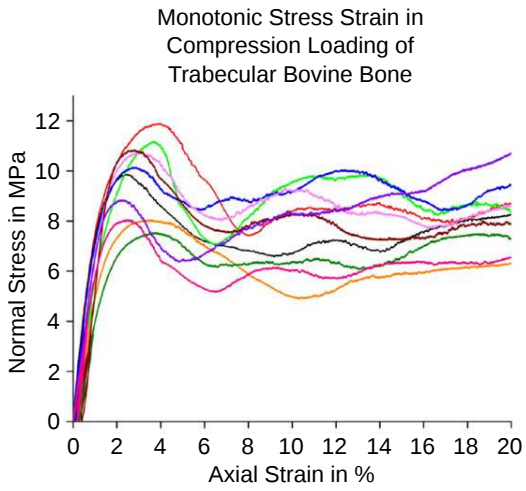

Figure 1.9: *Typical stress-strain curve of experiments performed on bovine trabecular bone (cylindrical shape specimens from bovine iliac crest with the diameter of 8 mm, and height of 15 mm, embedded into the endcaps using acrylic resin) under monotonic compression loading (Adopted From [111]). Similar trends have been observed in human vertebrae body specimens with same shape and dimension embedded in Polymethylmethacrylate (PMMA) [104].*

porosity and its microstructural orientation [97]. There are several theoretical models relating volume fraction, ρ, and fabric $\mathbf{M}$, defined in Equation 1.1, to mechanical properties in trabecular bone [97, 115]. Fabric elasticity model (Equation 1.2 [97]) and fabric strength model (Equation 1.3 [116]) in uni-axial loading condition are examples of these models which correlate the mechanical properties of trabecular bone to the morphological properties:

$$E_i = E_0 \rho^k m_i^{2l}, \nu_{ij} = \nu_0 \frac{m_i^l}{m_j^l}, G_{ij} = G_0 \rho^k m_i^l m_j^l \tag{1.2}$$

$$\sigma_{ii}^- = \sigma_0^- \rho^p m_i^{2q}, \sigma_{ii}^+ = \sigma_0^+ \rho^p m_i^{2q}, \tau_{ij} = \tau_0 \rho^p m_i^q m_j^q \tag{1.3}$$

These models are able to predict more than 90 % variation of mechanical properties of trabecular bone and are verified by different experiments on trabecular samples extracted from different anatomical locations in small strain [117–119], and large strain conditions [120]. Based on these models different fabric based yield criteria for trabecular bone have been proposed [121, 122].

In these models, eigenvectors can describe the amount of misalignment of the microstructure of the trabecular bone with respect to anatomical planes of animal's body. For instance, there is a different misalignment in human pedicles, and they vary between 0 to 30° [100]. This value for cortical bone is less than 6°, as in cortical bone

Table 1.2: *Mechanical properties of the trabecular bone with respect to different anatomical location. Elastic modulus E, compressive σ_{UC} and tensile σ_{UT} strength, yield strain in compression $\varepsilon_{0.2UC}$ and tension $\varepsilon_{0.2UT}$ are presented in this table.*

Anatomical Loacation	E [GPa]	σ_{UC} [MPa]	σ_{UT} [MPa]	$\varepsilon_{0.2UC}$ %	$\varepsilon_{0.2UT}$ %	Test Type	Reference
Human femoral neck	18.07 ± 2.8	133.67 ± 34.1	82.87 ± 11.1	0.83 ± 0.15	0.41 ± 0.04	macroscopic test	[112]
Human vertebra transverse	16.6 ± 1.1	-	-	-	-	nanoindentation	[113]
Human vertebra longitudinal	19.4 ± 2.3	-	-	-	-	nanoindentation	[113]
Human vertebral	0.301 ± 0.1	2.23 ± 0.95	2.23 ± 0.76	0.84 ± 0.06	0.78 ± 0.04	macroscopic test	[105]
Bovine tibia	18.7 ± 3.4	20.64 ± 0.59[a]	14.88 ± 0.18[b]	1.09 ± 0.12	0.78 ± 0.04	macroscopic test	[114]

[a] Compressive yield stress

[b] Tensile yield stress

microstructures are aligned in the longitudinal direction of osteons in bone [123].

Accordingly, different constitutive continuum models have been developed to describe the mechanical behavior of the cortical and trabecular bones [97, 124], and dif-

ferent failure criteria such as cellular solid [125] and quadratic multiaxial Tsai-Wu criterion [126] have been implemented. Importance of such multiaxial failure, the criterion is in the simulation of non-habitual loading configuration such as falling, which increases the risk of fracture. They can also be used in the simulation of the interaction of bone-implant systems.

Finite element models constructed from these datasets have been used to determine apparent mechanical properties of bone and to predict the fracture risk [127].

1.4.2 Fabrication Techniques

Recent developments in the advanced fabrication approaches such as 3D printing (additive manufacturing [22, 44, 128, 129], (magnetic) freeze casting [130–132] and laser engraving [133] provide different tools and pathways for the manufacturing of bio-inspired materials. In this section, we review some of these manufacturing techniques. Finally, few bone-inspired materials will be presented.

Additive Manufacturing

Additive manufacturing (AM) techniques belong to the family of technologies that use computer design in building layer-by-layer structures. These techniques enable accurate and independent spatial distribution of materials and geometrical featuring [44, 129] (Figure 1.10).

According to ISO/ASTM52900-15, additive manufacturing techniques are divided into seven categories: binder jetting, directed energy deposition, material extrusion, material jetting, powder bed fusion, sheet lamination and vat photopolymerization. 3D printing has been used in different sectors such as manufacturing, industrial and medical [134]. This technique has also been used for the creation of tissue scaffold and implant [19] by mimicking the tissue microstructures via 3D bio-printing [135] and magnetic 3D bioprinting [136, 137] that have an important application in tissue engineering and regenerative medicine.

AM has been used for replicating design elements from nature to synthetic materials. Multi-scale and gradient in materials and hierarchical designs can be achieved by advanced AM and multi-material AM techniques [44]. There are several attempts to produce and replicate structural features existing in biomaterials. One example is mimicking the toughening mechanisms of mineralized natural materials in bone and biocalcide-like artificial structures that make high fracture resistance [138]. Effect of mineral bridges and its size inspired by nature on the fracture properties of these materials was an example of using multi-material 3D printing [139]. Mimicking the self-assembly at nanoscales by forming a polymer-ceramic bio-inspired material was

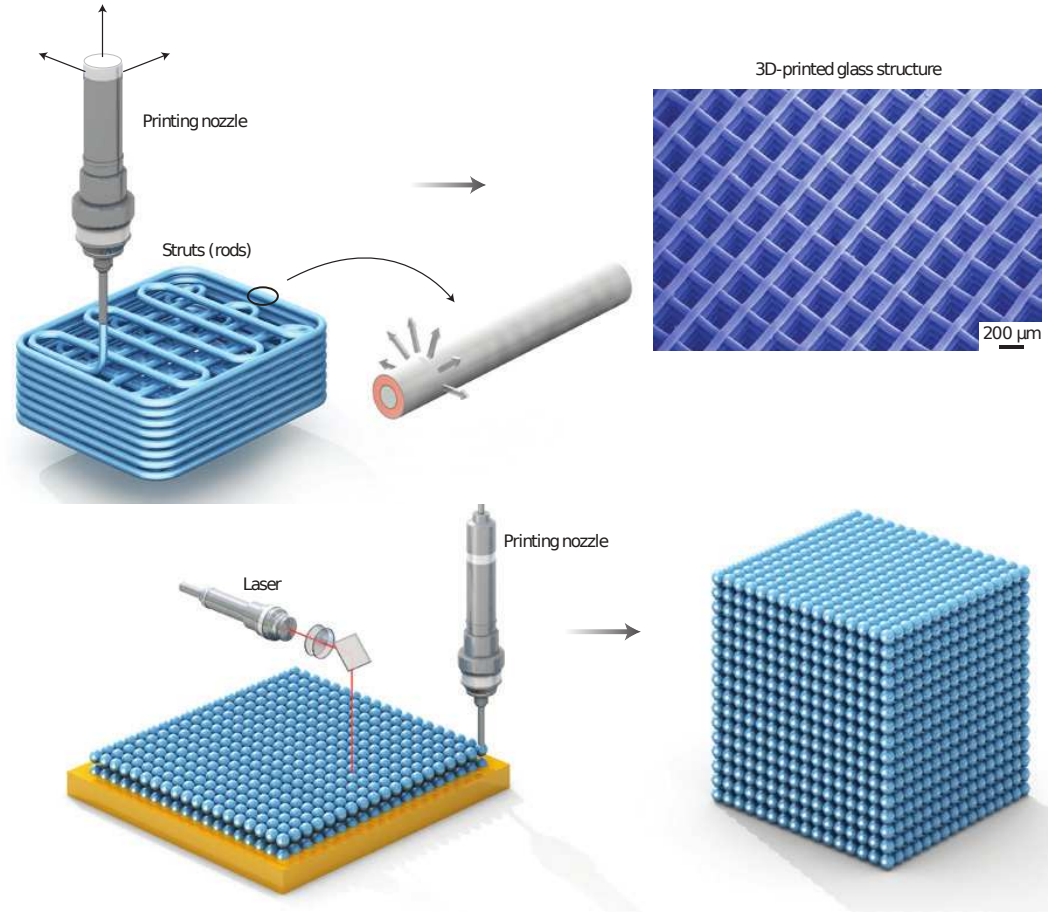

Figure 1.10: *Additive manufacturing techniques that can be used for the fabrication of precise and reproducible geometrical features. (Adopted from [77]).*

another example of using additive manufacturing techniques [140].

Applications of 3D printing in the design of new bio-inspired materials are limited to two main problems [77, 129]; first, the number of materials that can be printed is limited to metals, polymers, and ceramics. Due to the hybrid combination of dissimilar building blocks in biomaterials, i.e., polymers and ceramics, printing bioinspired materials with same material mismatches are limited. Therefore, it makes it difficult to have one manufacturing technique to fabricate such materials. The second problem is related to print at different scale, i.e. from nano to macro scales. Although it is possible to print fine features at nano levels using methods such as nanolithography [141] or inkjet printing [142] these methods cannot be used for the fabrication of materials at large scales.

Freeze Casting

Freeze casting or ice templating is a manufacturing process that has been used for the fabrication of nacre-like inspired ceramic materials with high toughness properties [130, 131]. The reason to mimic the microstructure of nacre is that its majority consists of minerals (99 % of volume) while its toughness can be an order of magnitude higher than the mineral constituents. This is due to the arrangement of mineral platelets in a 'brick-and-mortar' like fashion [2].

It is an inexpensive procedure for directionally freezing of the ceramic-based suspensions in water [77, 143]. It has been used for the manufacturing with metal/ceramic, polymer/ceramic and hybrid materials [143]. Moreover, this method was also used for the replication of 'brick-and-mortar' structures, i.e., brick-shaped mineral platelets within layers of mineral materials, similar to those of nacre 1.11. It has been shown this method can be useful for production of cellular structures by directional solidification of platelet-based slurries [144].

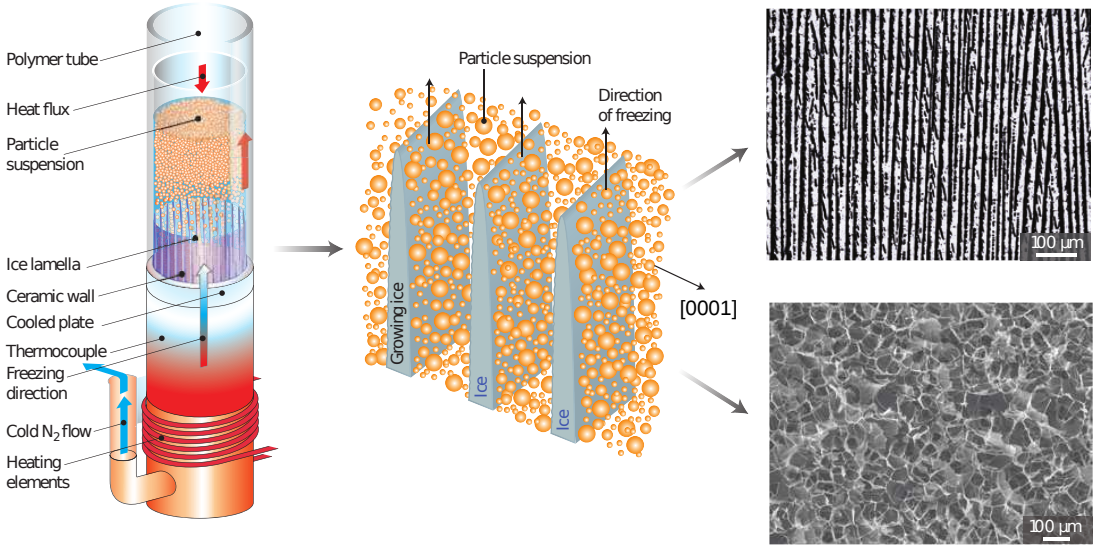

Figure 1.11: *Using freeze casting in the replication of nacre-like microstructures. Combination of directional freezing of ceramic suspensions and microstructures of ice will be used to template the architectural features of the scaffold. This can be used in the fabrication of layered and porous structures [130, 131]. By adjusting the suspension's composition and ice grows' speed one can control the dimension of microstructures [77]. (Adopted from [77])*

Bone-inspired examples

Different structural and material characteristics of cortical and trabecular bones have been used in the past for the bio-mimetic purposes. The aim of such design can be either

to reach improved mechanical properties or to obtain specific functionalities similar to what can be seen in the natural design.

One of the most exciting properties of materials such as bone and nacre is their high specific strength/ stiffness and toughness while being light [76] as it has been an issue to have simultaneously high stiffness/ strength and high toughness properties [38, 145]. In another word, attempts to increase one property will result in the reduction of the other one. Different microstructural organization are responsible for such property which has been regarded as a source of inspiration for the production of the new advanced (bio-)materials with different applications in medical and material science.

As an example, toughening mechanisms of cortical bone at microscale was replicated in the construction of bio-inspired composite materials via different manufacturing methods such as traditional composite materials [21, 146], 3D printing [147], and 3D magnetic printing process [137]. This mechanism includes crack deflection in the cortical bone that occurs due the existence of osteons or Haversian canal [21, 146, 147] (Figure 1.12a,b). Libonati et al., designed, manufactured and characterized the bone-inspired synthetic composites and showed higher strength compare to classic laminate composite materials [21, 146]. They also used high-resolution multi-material 3D printing techniques for the fabrication of such materials and showed that how similar modes of fracture to the cortical bone can be observed in the synthetic composite materials. These modes of failure were crack deflection and branching and constrained microcracking which enhanced the toughness properties of the artificial materials [147]. For mimicking the microstructure of cortical bone, Libonati et al. defined two different shapes for the microstructures, i.e., circular and elliptical, representing the Haversian units while the soft/ hard ratio in the designed composites were kept constant (Figure 1.12a). That explained how biomimetic approached in mimicking the geometrical features of cortical bone can active further toughening mechanisms and finally, amplify toughness of the artificial materials.

The combination of the direction and distribution of trabeculae within trabecular bones can be considered as a significant factor in their excellent original design which influences the macroscopic properties of such materials. Mimicking the microstructure of trabecular bone in open-cell foams with the aim of replicating similar interconnectivity for the application in the orthopedic area was used for the fabrication of bone-inspired material [111] (Figure 1.12c). Guillén et al. studied open-celled metallic foams as their material have interconnected structure with homogeneous and adjustable densities which can be used in the orthopedic research area and especially in the design of bone scaffolds as it is required to have similar microstructural properties of trabecular bone. They compared mechanical properties of different foams from Aluminum

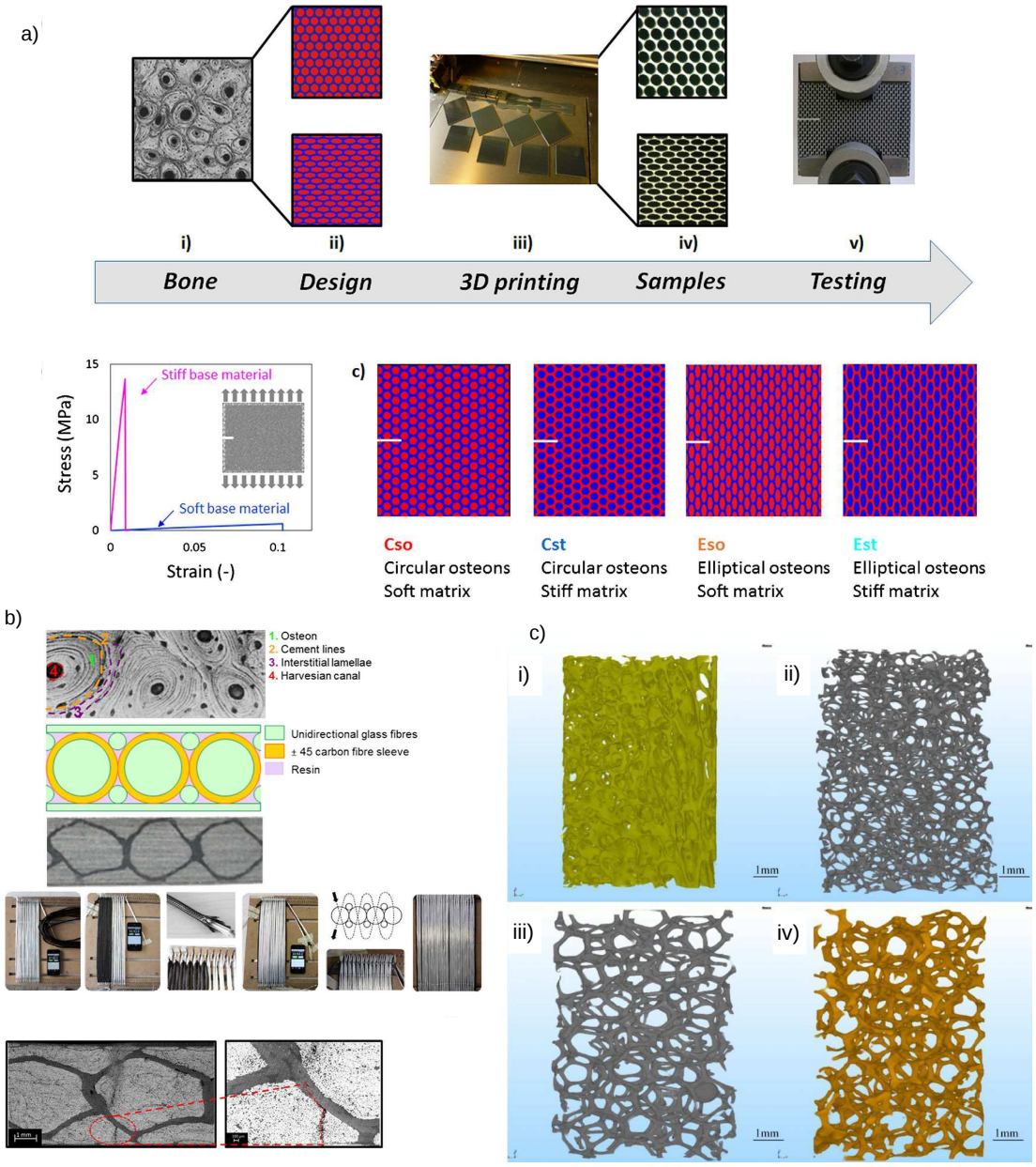

Figure 1.12: *Examples of bone-inspired materials manufactured with different aims and different manufacturing techniques. a) Mimicking the microstructure of cortical bone to enhance the toughness properties of the synthetic material. Multi-material 3D printing was used for the fabrication of these materials [147]. b) Fiber- reinforced composite inspired by the microstructure of cortical bone to mimic the crack deflection mechanism based on the role of cement line in bone [146]. c) Mimicking the microstructure of trabecular bone in foams constructed by precision-cast technique i) bovine trabecular bone, ii) AlSi7Mg foam, 45 ppi, iii) AlSi7Mg foam, 30 ppi, iv) CuSn12Ni2 foam, 30 ppi [111].*

alloys, which had the minimum porosity of 30 ppi (pores per inches) with trabecular bovine bone. They used precision-cast for the production of polymeric molds. Then, the mold was filled with mold casting slurry and finally baked them to harden the cast-

ing material.

Fabrication of multifunctional metallic foams inspired by lightweight bird bone was another example for bone-inspired materials which demonstrated low adhesive superhydrophobic self-cleaning, and striking loading capacity similar to water strider leg found in nature [148]. One of the applications of the resulted bio-inspired metallic foam is to built an oil/water separation apparatus with high separation efficiency and long-term repeatability [148].

Few examples of bio-inspired materials manufactured by different manufacturing methods have been discussed so far. These approaches have gained a great deal of attention and undoubtedly in the near future new engineered materials will be proposed. Few exhaustive reviews [4, 19, 128, 129] on this subject have been recently published which are referred for further case studies of bio-inspired materials.

1.5 Outline

In the previous sections, key design element features in natural materials were discussed and various fabrication methods for the implementation of such features in the synthetic materials were reviewed. Some of the examples of bio-inspired materials were discussed as well. Implementing the important topological design elements in the fabrication of new artificial materials with different purposes and applications are the topic of the following chapters.

The prime characteristic of structural features in natural materials can be summarized as: **functionally gradient**, **multiple length-scale hierarchy**, **randomness**, **anisotropy** in either microstructures or mechanical properties of the biological materials. Most of the biological materials adopt a smart and optimized combination of these features to meet specific functions and design motifs. Concerning functionally gradient both in microstructures and mechanical properties, it can happen through different orientation, dimension, arrangement and distribution of the microstructures. In addition, it happens to have specific shapes in the microstructures of natural materials such as re-entrant honeycomb or cellular shapes.

Integrating all these features in the construction of advanced synthetic materials can lead to the properties that cannot be achieved by the traditional approaches. Moreover, to implement those features, we need to use the current manufacturing techniques or propose a modified version of those techniques. Therefore, each chapter contains specific topological properties, an aim to use those features, and finally the manufacturing technique that we used for the fabrication of those materials. These are summarized in Table 1.3.

Table 1.3: *Summary of the topics of different chapters in this thesis.*

Chapter	Topological features	Manufacturing technique	Aim
2	Functionally gradient (through orientation, dimension and distribution), Anisotropy	Foaming process	Mimicking the microstructure of trabecular bone to achieve similar mechanical properties
3	Functional/ pattern Randomness, Metamaterial	Additive Manufacturing	Independent tailoring of elastic properties
4	Functional gradient, Metamaterial	Additive Manufacturing	Shape matching
5	Randomness	Crumpling	Proposing a manufacturing method for converting surface functionalization to 3D

1.5.1 Summary of achieved results in each chapter

In the following, a summary of methods and achieved results in each study is discussed:

- in **Chapter 2**, we investigated the application of conventional foaming processes for the production of a new aluminum foam material by mimicking the loading adaptation features of the microstructure of the trabecular bone. The loading adaptation features of trabecular microstructure exhibit a graded distribution of porosity and cell size, with axially elongated cells (anisotropy). To reach this goal, we designed, manufactured and tested two different types of bone-inspired aluminum closed cell foams, aimed at mimicking the loading adaption feature: the first type, characterized by a directional gradient of pores (i.e., along the length of the specimens) and the second type, characterized by elongated pores by the hot rolling process. We used micro-computed tomography (μCT) to compare the morphological properties of aluminum foams and bones. Furthermore, we built geometry-based Finite Element (FE) models from the (μCT) images and validated them by means of experimental results. In the next step, image analysis techniques were used to create virtual models and to expand the range of experimental data. This helped to get further insight into the structural behavior of the materials. From the results of this study, we introduced a manufacturing method for the fabrication of closed cell aluminum foams with biomimetic uniaxial mechanical properties in the low strain regime. The method involved controlling the relative density and the axial orientation of cells of aluminum foams. Concerning the inexpensive cost of this manufacturing process, it can have several applications in

the aerospace and automobile industry. For instance, they can be used for a structural application requiring load-bearing features and high impact-absorbing parts in vehicles such as car bumpers or helmets. They can also have biomedical application in the production of the prosthesis. The results of this study were published in *Materials and Design*. It also resulted in two conference presentations at *21st European Conference on Fracture, ECF21, 2016, Catania, Italy.* and *4th Cellular Materials, CellMAT2016, Dresden, Germany*.

- in **Chapter 3**, we introduced patterned randomness as a strategy for independent tailoring of the elastic properties of soft metamaterials, i. e. the elastic modulus and Poisson's ratio. Randomness is one of the features that can be found in the biological substances, and combining this feature with metamaterials was the topic of this chapter. Elastic properties of mechanical metamaterials are a direct function of their topological design. Therefore, we used rational design approaches based on computational models to devise topological designs and reach desired properties. For this aim, soft mechanical metamaterials incorporating various types of patterned randomness were fabricated using indirect additive manufacturing technique and mechanically tested. We also developed computational models to predict the topology-property relationship in a wide range of proposed topologies. From the results, we showed that patterned randomness could be used for independent tailoring of elastic properties and cover a broad area of the elastic modulus-Poisson's ratio plane. The uniform and homogeneous topologies constitute the boundaries of the covered area, while topological designs with patterned randomness fill the enclosed area. The results of this study were published in *Applied Physics Letters*. They were also presented at *MatCel2017 & DynMatCel2017, 25-27 September, Aveiro, Portugal*.

- in **Chapter 4**, we used the concept of functional gradient metamaterials in order to obtain specific functions. Architecture materials with rationally designed topologies could be used to create mechanical metamaterials with unprecedented or rare properties and functionalities. We introduced 'shape-matching' metamaterials where the topology of cellular structures comprising auxetic and conventional unit cells is designed so as to achieve a pre-defined shape upon deformation. We used computational models to forward-map the space of planar shapes to the space of topological designs. The validity of the underlying computational models was first demonstrated by comparing their predictions with experimental observations on specimens fabricated with indirect additive manufacturing. The forward-maps were then used to devise the topology of cellular structures that approximate the

arbitrary shapes described by random Fourier's series. Finally, we show that the presented metamaterials could match the contours of three real objects including a scapula model, a pumpkin, and a Delft Blue pottery piece. Shape-matching materials have potential applications in soft robotics and wearable (medical) devices. The results of this study was published in *Scientific Reports*.

- in **Chapter 5**, we proposed crumpling as a fast and easy fabrication technique for manufacturing crumpled-based materials. Crumpling or folding of thin wall objects frequently encounters in nature such as in brain cortex and flower buds. Due to the random nature of the crumpling mechanism, study the physics of crumpling and crumpled-based materials could result in new advanced materials with different properties. These materials have been shown to have robust mechanical properties for practical applications, including meta-biomaterials design aimed for improved tissue regeneration. For such requests, however, the structure needed to be porous. Therefore, we introduced a crumpled holey thin sheet as a robust bio-metamaterial and measured the mechanical response of a crumpled holey thin Mylar sheet as a function of the hole size and hole area fraction. We also studied the formation of patterns of crease lines and ridges. The area fraction mostly dominated the crumpling mechanism. We also showed that the crumpling exponents slightly increases with increasing the hole area fraction and the total perimeter of the holes. Finally, hole edges were found to limit and guide the propagation of crease lines and ridges. The results of this study have been published in *Scientific Reports*.

CHAPTER 2

Mimicking the Loading Adaptation of Trabecular Bone in Closed-Cell Aluminum Foams

From the manuscript published as[1]

2.1 Introduction

Through the history, nature has always been considered as a source of inspiration for scientists and engineers to create or mimic new materials with augmented material properties. Natural materials, composed of an organic soft component and mineralized hard component, exhibit a complex hierarchical architecture that magnifies the performance of each layer of the hierarchy [18, 77]. Structure-property-function relationship of natural biological materials has been used in designing new technologies such as magnetic freeze casting [130, 131, 149], magnetic slip casting [150], 3D magnetic printing [137, 150] or in synthesizing ceramic [131] or composite [146, 147, 151, 152] materials.

Among natural materials, trabecular or cancellous bone and woods are examples of lightweight cellular materials with remarkable stiffness and strength, and multi-

[1] M. J. Mirzaali, V. Mussi, P. Vena, F. Libonati, L. Vergani, M. Strano, Mimicking the loading adaptation of bone microstructure with aluminum foams, *Materials and Design*, doi: 10.1016/j.matdes.2017.04.039

ple functions. For instance, trabecular bone in the skull is surrounded by cortical bone and constructs a sandwich structure that protects the brain from impact loading. As a further example, radial variation of density in bamboo and palm improves their mechanical properties and helps them in limiting deflection under the applied loads [41]. The mechanical properties of such materials come not only from their chemical composition, but also from the fundamental multiscale hierarchical architecture [41, 77, 82, 110, 128, 153–156]. Metal foams with closed cells are lightweight materials with a random cellular structure that exhibit high energy absorption, damping capacities and high strength/ stiffness ratio. Their morphology has often been compared to the porous structure of cancellous bones and as a consequence, they have frequently been considered a class of biomimetic materials [157, 158]. However, a quantitative comparison of the morphological and mechanical parameters of metal foams with cancellous bones has never been attempted in a comprehensive paper. Besides, the conventional manufacturing routes [159–161], used for producing closed cell metal foams, have never been modified or addressed towards the goal of producing biomimetic materials.

Closed cell aluminum foams are particularly suited for the purpose of absorbing mechanical energy, either at small deformations (i.e. acting as a vibration damper) or at large deformations (i.e. acting as an anti-crash member). Metal aluminum light foams can be used as a reinforcement filler in sandwich panels. They also have wide applications as load-bearing parts in engineering structures for vehicles, where lightweight components with high energy absorption are needed, i.e. helmets, car bumpers [162, 163], and so forth. Closed cell aluminium foams have several similarities with cancellous bones, though bones have open cells. This apparent similarity has never been designed on purpose but, the supposed biomimetic structure of cellular metals is only an incidental result of the typical manufacturing processes. Owing to this enhanced biomimicry, bone replacement could be one of the many potential applications of metal foams, although biological compatibility is a crucial issue which actually limits the selection of the materials to be used in the metal foam manufacturing. More generally, biomimetic closed cell aluminum foams can be used as a structural reinforcement in any application where the load is not deterministic, but has dominant or preferential loading directions. In this context, the morpho-mechanical properties of trabecular bone may be the primary inspiration for the design of new lightweight materials with effective mechanical properties.

Recently, additive manufacturing processes such as Electron Beam Melting and Selective Laser Melting have been proposed in order to produce designed biomimetic structures [164]. However, additive manufacturing processes are more suited for the

production of the open cell rather than closed cell foams, because of technical and economic constraints. As of today, the most cost-effective and efficient technology for producing closed cell aluminum foams is the expansion of a foaming agent in a sintered compacted aluminum matrix [165]. Accordingly, based on the numerous potential applications of foam materials in aerospace and automotive industry, modification of the manufacturing process and improving foam mechanical properties has continuously been on demand. A new way of enhancing their behavior might come from an improvement of the production process, with the goal of mimicking the characteristic features of natural foam materials.

Based on Wolf's Law, the trabecular microstructure is aligned with the direction of loading and principal stress [90, 91]. Similarly, by breaking the inherently isotropic orientation of the microstructure of closed-cell aluminum foams, one may boost the mechanical properties of such materials in one direction. In other words, microstructural anisotropy will result in mechanical anisotropy analogous to natural cellular materials. Such property is valuable for the case of engineering structures experiencing anisotropic loading situation in their operation life.

It has been shown that the mechanical properties of cellular materials depend not only on the mechanical properties of the solid itself, but also on the amount of this material (i.e. the relative density) and on the geometrical arrangement of microstructures [110]. Among the microstructural parameters, the relative density is the most compelling factor affecting the mechanical properties of cellular materials [166, 167]. However, the architecture and the orientation of the microstructures play a significant role on the bulk properties, especially in natural cellular materials [115, 168, 169]. Several morphological parameters can be used to describe the microstructure of cellular materials, such as the average strut thickness, the average cell size, and so forth. Directional variations of the microstructures can be assessed using the Mean Intercept Length (MIL) [94] parameter. From the MIL values it is possible to obtain the fabric tensor, a positive definite second-order tensor [96, 98, 170], which shows the preferred microstructural orientation of the cellular materials. These parameters, used to describe the microarchitecture of trabecular bones, can be also used to describe the microarchitecture of anisotropic manufactured aluminum foams.

The aims of the present paper are: 1) to quantitatively compare, in terms of mechanical and morphological parameters, the properties of trabecular bone (taken from bovine samples) and those of aluminium closed cell foams; 2) to modify the standard manufacturing process to better mimic the natural morphology of cancellous bones, its anisotropy. For this purposes, we produced and tested two sample sets of closed-cell foams with a modified manufacturing process, able to produce samples with sta-

tistically different morphological parameters. We used micro-Computed Tomography (μCT) to compare the morphological properties of aluminum foams with those of trabecular bone, and the fabric tensor to measure the degree of anisotropy. Mechanical compression testing allowed us to compare the mechanical response of the foams, whereas micro finite Element (μFE) models, built from each CT-scans, allowed us to get a further insight into the structural behavior of each material.

Using image analysis techniques, virtual FE-models have been created to allow a further comparison with human trabecular bone, based on the fabric-base model.

2.2 Materials and Method

Four different types of metal foams samples have been prepared, according to the summary plan in Table 2.1. Groups A and C are produced as 'control groups', with a conventional foaming process. Groups B and D have been produced in order to induce, respectively, inhomogeneity and anisotropy of metal foam closed cells. In Table 2.1, the expected morphology is briefly reported. In Figure 2.1 and Figure 2.2, the obtained typical morphology of the four groups will be reported.

Table 2.1: *Summary of produced metal foam samples in comparison with bovine trabecular bones.*

	Manufacturing method	Expected overall relative density, ρ_s	Expected morphology
Group A	Standard	19 %	Uniformly sized and shaped cells
Group B	Modified precursor position inside foaming die	19 %	Graded distribution of porosity and cell size
Group C	Standard	28 %	Uniformly shaped cells
Group D	Standard process + hot rolling	>30 %	Uniformly shaped cells, axially elongated
Bones	-	>30 %	Graded distribution of porosity and cell size, axially elongated cells

The standard manufacturing method used for the production of control group A is now described. Aluminum foam specimens were prepared using foaming of a sintered powder, in which a mixture of particles containing an appropriate blowing agent was compacted to a condensed precursor and foamed above the solidus temperature of the resulting alloy [171, 172]. Trade precursor rods (Mepura^{TM}), produced by a direct powder extrusion, were used with $AlMg_1Si_{0.6}$ composition and 0.8 % weight of TiH_2 as blowing agent. Precursors rods with the diameter of 10 mm were cut by a band saw,

and the sawed surfaces were ground with a sand paper (120 grit SiC) to obtain cylinders with the exact desired weight, with a margin of error of $\pm$ 0.06 g. As an example, to produce a cylindrical foam sample with an average overall density of 650 $\frac{kg}{m^3}$ and a length of $L = 50$ mm, a single precursor rod has to be inserted in the center of a cylindrical foaming mold, made of a titanium tube with an inner diameter of 10.9 mm (Figure 2.1a). Two stainless steel caps (14 mm thick) were applied at both ends to limit the foam expansion to the desired final length of ~50 mm. The inner volume of the mold was selected with the purpose of producing foamed specimens with the prescribed density of 650 $\frac{kg}{m^3}$ starting from a 2.99 g precursor rod. The mold was placed at the center of an air convection laboratory furnace (Nabertherm L9/11-HA) preheated at 750° C for about 205 s. The mold support in the furnace was designed with only four contact points with the foaming mold to achieve the best temperature uniformity during the heating and foaming phases. Thus, the amount of heat exchanged by conduction was minimized. The mold was then extracted, positioned on a cooling support, rotated 360° along its longitudinal axis in the steady air, and finally cooled to room temperature with compressed air. The final diameter of the foam cylinders is smaller than 10.9 mm, due to post cooling shrinkage, and is equal to about $10.8 - 10.9$ mm.

The standard manufacturing method used for the production of control group C is very similar the one used for group A. The only difference are the size of the precursor rod (which is 8.6 mm in diameter instead of 10) and the shape of the foaming mold, which is prismatic with a square cross section (internal square side 9 mm) and rounded corner radii (2 mm).

2.2.1 Foam with graded distribution of porosity

To alter the distribution of porosity inside the samples and the size of the foam cells, the standard process described above has been slightly modified, by changing the initial position of the precursor rod at the beginning of the foaming process, as seen in Figure 2.1b. This new layout resulted in a different spreading of pores along the length of the specimens. Ten closed-cell aluminum foam samples were included in this part of the study and were divided into two groups: group A, the standard control group of closed-cell aluminum specimens (with a heterogeneous distribution of pores), and group B with a graded variation of pores along the length of samples (Figure 2.1b). Five samples were considered in each set. Foam samples had original length L of about 50 mm. A lathing machine removed the exterior skin of each foam sample (the skin is not porous) and reduced the diameter down to $OD = 9.5$ mm. The chuck spindle of the lathe damaged both ends of the cylindrical specimens. For this reason, a circular saw abrasive cutting blade with water cooling (HITECH EUROPE) has re-

moved 16 mm length from each end, leaving the sample with a final length of about $L = 18$ mm. Distribution of the relative density along the length of the specimens in groups A and B are depicted in Figure 2.1c and Figure 2.1d, respectively. While the overall average value of relative density can be easily determined by a proper selection of the mass of precursor inserted inside the tubular die, the actual profile distribution has a limited controllability. To some extent, the grading porosity is controllable, because it is mainly due to friction at the foam-die interface when the foam is semi-solid. Therefore, the regions of larger or greater relative movement can be roughly predicted.

We should notice that, to analyze the distribution of the relative density, we removed from the μCT-images few slices, corresponding to the specimen top and bottom and generally affected by artifacts, chosing an equal length of 16 mm for all the specimens. This allowed us to perform a comparison among all the foam samples, neglecting possible distorsion arising at the specimen ends (Figure 2.1 and Figure 2.2).

2.2.2 Foam with axially elongated pores

To prepare samples with axially elongated pores (group D) (Figure 2.2c), a hot rolling operation was performed as a post-foaming treatment. Specifically, specimens were first foamed according to the standard method used for group A. After cylindrical foam samples (about 10.8 mm OD) had been prepared, they have been hot rolled along their axial direction, with two subsequent rolling passes at a tangential rolling speed of $7.6\frac{m}{min}$. Contrarily to Group A samples, the skin was not removed after the rolling process for Group D, in order to prevent microstructure damage that would have been induced by the rolling. With the given rolling speed, the temperature of the samples has been measured in a preliminary experiment with a thermocouple embedded inside the sample. The measured values are 520° C at the rolling entry section and 490° C at the exit section. The rolling operations transformed the samples into bars with a square cross section, with two consecutive passes of equal area reduction ratio. The final side length of the square cross section was 9 mm, with rounded corners (Figure 2.2b). The hot rolling process can have an annealing effect on the residual stresses, which were induced by severe plastic deformation ([173–175]). The distribution of the relative density in groups C and D are shown in Figure 2.2d and Figure 2.2e. The rolling process produces specimens having distorted ends (Figure 2.2b). To produce the samples (18 mm long), we only considered the middle region, where the effect of distortion was negligible.

The specimens used as a control group (group C) have been produced with the standard manufacturing procedure (Figure 2.2a), described at the beginning of Section 4.2, using a square titanium tube as the foaming die, instead of a cylindrical tube. To be

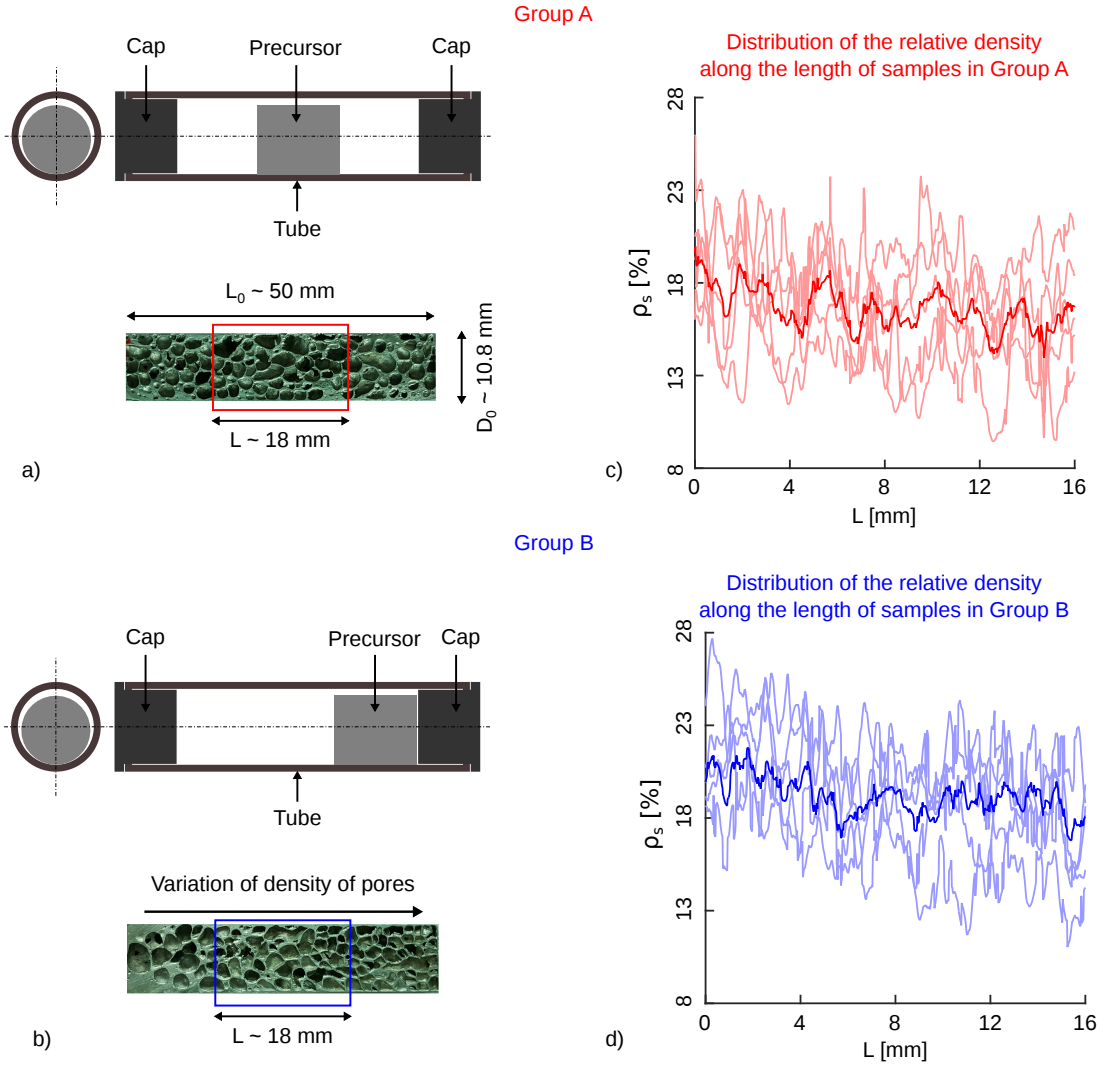

Figure 2.1: *Schematics of two different layouts for placing of the precursor in the mold. a) Placing the precursor in the middle of the tube results into a homogeneous distribution of pore size and density along the length of the specimen (Group A). b) Placing the precursor close to one end leads to a dispersal variation of pores along the dimension of the sample (Group B). The relative density distribution along the length of the tube for all samples in groups A (c) and B (d) is shown. The total length of the specimens is about 18 mm. For the sake of comparison, we chose equal length of 16 mm for all specimens to represent the relative density in (c) and (d). The bold line shows the average along of the relative density.*

consistent with the previous case, the skin has not been removed from control group C either.

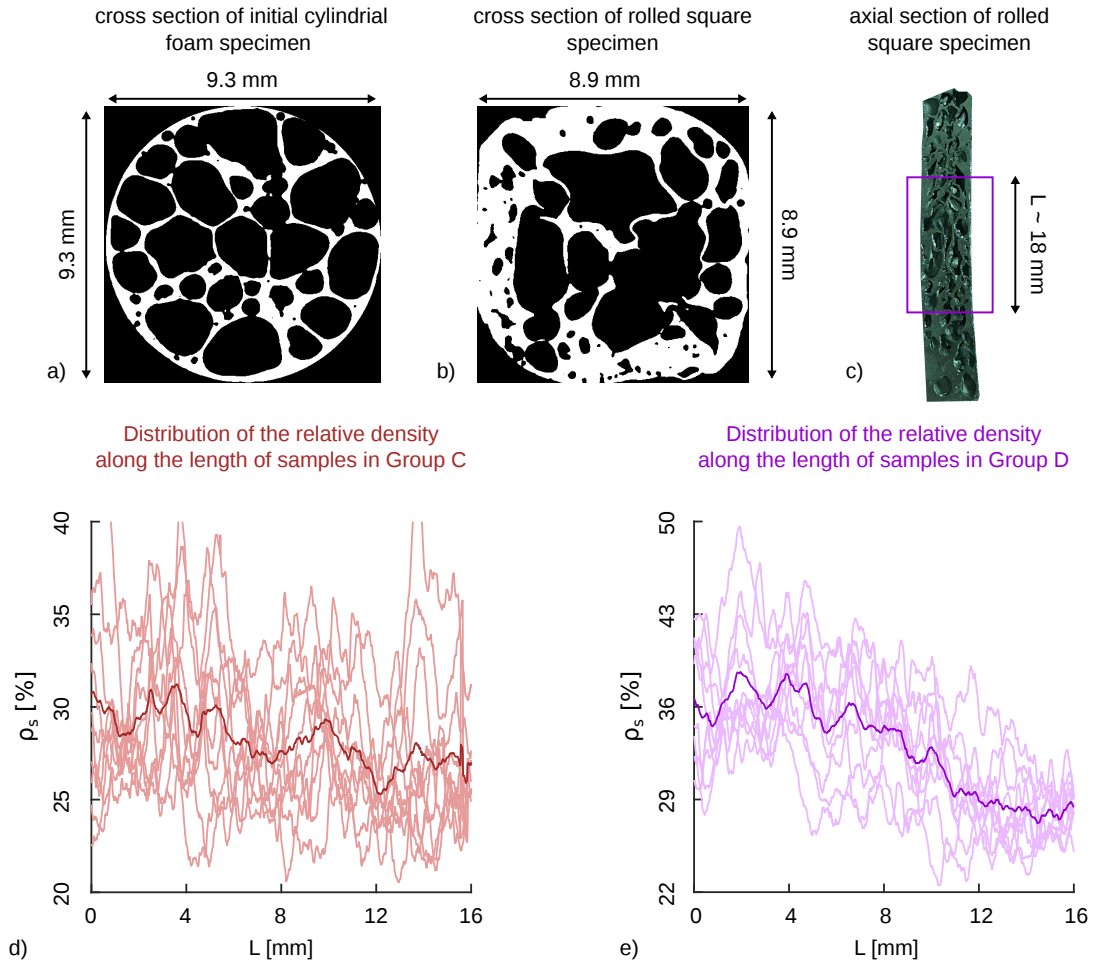

Figure 2.2: *Schematic of samples with axially elongated pores. a) µCT image of the cross section of the initial cylindrical sample. b) µCT image of the cross section of rolled square specimen. c) An example of the sample with axially elongated pores. d)-e) Relative density distribution along the length of samples in groups C and D. The total length of the specimens is about 18 mm. For the sake of comparison, we chose equal length of 16 mm for all specimens to represent the relative density in (d) and (e). The bold line shows the average along of the relative density. In panel b) it is possible to notice a distortion, which affected only one end of the specimen. This distortion is not affecting the other results as we cut the 18 mm-samples from the middle region of the bar.*

2.2.3 Trabecular bovine sample preparation

For comparison of foam materials with trabecular bones, 13 trabecular specimens were included in this study. Cancellous bone samples were harvested from the lower extremity of the bovine femur. Samples were drilled using a coring device (WÜRTH MACHINERY) in the principal direction of the trabecular structures. The coring device has the inside diameter of 10 mm and length of 30 mm. Subsequently, the samples were transferred to a lathing machine (OPTIMUM) to reduce them to cylinders with

the diameter of 8 mm and height of 26 mm. Specimen were kept wet during milling and coring by water. The trabecular cylinders were dried for 24 h at room temperature. When dried, the ends of the bone specimens were glued to custom-made aluminum end caps, using epoxy adhesive (LOCTITE 435 Instant Adhesive) with the purpose of reducing the edge effects [176] during mechanical tests. It has been shown that the repeated drying and re-wetting of the bone samples have minor effects on the mechanical properties of the bone [177]. However, as the mechanical properties of the bones strongly depend on the condition (e.g. dry or wet) [178], we performed the mechanical tests on wet bone samples.

The end caps, with an inner diameter of 8 mm and an outer diameter of 10 mm, covered 10 mm of the bone specimens length. The outer side of the bone samples, as well as the aluminum end caps, were defatted using acetone before gluing. Custom-made alignment tools were used to keep the bone and the end caps aligned within the direction of axial loading.

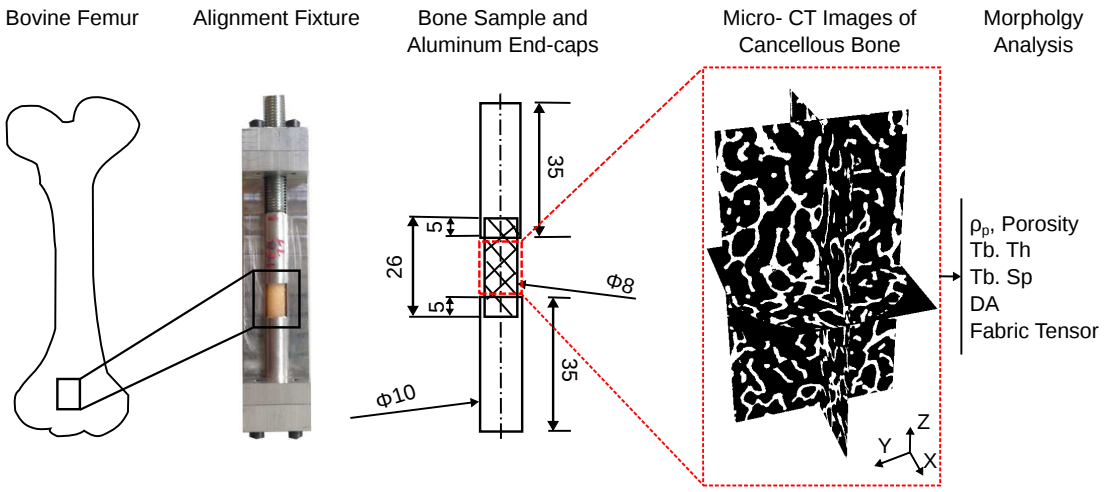

Figure 2.3: *Cylindrical bovine specimens were cut from the proximity of the bovine femur. Both sides of the specimens were glued in an aluminum end caps, using an alignment fixture. Before the mechanical testing, μCT images were collected for each specimen, and morphological features were calculated.*

2.2.4 Image analysis

Micro-computed tomography (μCT) of the metal foam and trabecular samples have been collected using an x-view scanning equipment (North Star Imaging Inc.) with the spatial resolution of 20 μm for foam samples and 27 μm for bone specimens. Parameters of the scanning were fixed at 40 kV and 220 μA for aluminum foams and 112 kV and 21 μA for bones. Simultaneously, five specimens were placed in the CT equipment

and total imaging time was around 60 minutes for both materials. Bone specimens were submerged in the saline solution (0.9 % NaCl) during scanning.

The x-view CT software has performed image reconstruction. Image analysis has been done in ImageJ [179] software and bonej plugin [180]. A same cylindrical region of interest (ROI) equal to the smallest diameter of foam samples has been considered for each sample. Using a Gaussian blur filter ($\sigma = 1.5$) noises were removed from the images. Otsu local thresholding method [181] has been used for the segmentation of the images which resulted in binary images with the voxel value of 1 for aluminum and 0 for the empty spaces.

Porosity (ρ_p) was defined as the total number of cavities to the total number of voxels in ROI in the binary image. The relative density was defined as $\rho_s = 1 - \rho_p$. Strut thickness ($St.Th$) and strut spacing ($St.Sp$) were calculated based on the conventional definition of the greatest sphere diameter that fits within the structure [101]. Foam surface FS (or bone surface BS) was defined as the inside surfaces of the foam materials and was calculated by the isosurface creation of the binary image with the resampling equal to 4 [182]. Given the solid volume of the samples, V, the ratio $\frac{BS}{V}$ ($\frac{FS}{V}$) can be calculated in order to estimate the amount of available surface for a material quantity. Connectivity was defined on the purified image. Tortuosity was defined as the Euclidean number of the longest branch in the skeletonized image and was calculated by 3D skeletonization plugin. Structural Model Index (SMI), which is an estimation of the plate-rod characteristic of the structure of the foams was calculated from the binary images based on the method proposed in [102]. The main direction of the microstructures of the foams was measured by MIL [94]. It has been shown that an ellipsoid can approximate MIL in three-dimensions [96], and lead to the definition of a positive definite second-order fabric tensor that characterizes the degree of anisotropy of the foam/bone microstructures. Moreover, based on the general theory developed in [98], fabric tensor, which is the inverse of MIL tensor, has been applied to measure the local structural anisotropy. Fabric tensor is defined as:

$$\mathbf{M} = \sum_{i=1}^{3} m_i \mathbf{M}_i = \sum_{i=1}^{3} m_i (\mathbf{m}_i \otimes \mathbf{m}_i). \tag{2.1}$$

Where m_i are the positive eigenvalues, and the $\mathbf{m}_i$ are the corresponding normalized eigenvectors of the fabric tensor. $\mathbf{M}$ is normalized to $tr(\mathbf{M}) = 3$, which ensures that fabric is independent on volume fraction. The three eigenvectors of $\mathbf{M}$ represent the principal axes of symmetry of the material, also corresponding to the main orientations of the strut. Based on the distinct eigenvalues, the fabric can be isotropic, transversely isotropic or orthotropic [99]. The degree of anisotropy (DA) can be defined as the ratio

of the largest over the smallest fabric eigenvalue.

2.2.5 Monotonic compression testing

Quasistatic monotonic compression tests have been conducted using an MTS machine (Alliance, RF/150) with the load cell of 150 kN (class 1 ISO 7500-1) and under the stroke rate of 8.5×10^{-2} $\frac{mm}{s}$ (strain rate of 5×10^{-3} s^{-1} for testing of bone and foam samples. The boundary conditions of the compression test were free for the foam samples. The bone samples, instead, are confined into the endcaps. An external deflectometer (MTS 632.06H-30) was adopted to measure the small axial displacements. Testing was performed at room temperature and axial displacement (S), axial loading (F), time and axial strain (E) was recorded by the sampling rate of 20 Hz. Nominal stress (Σ) was defined as the ratio of axial force (F) to initial area (A_0) obtained from μCT scans for each sample. Yield stress ($\Sigma_{y0.2}$) and yield strain ($E_{y0.2}$) were obtained based on a 0.2 % offset criterion. The global (apparent) elastic moduli (C_a) of the samples were calculated using a moving regression with a box width of 0.2 % strain to identify the stiffest section of the loading part. Ultimate stress (Σ_{ult}) was obtained as the maximum stress before densification and its corresponding strain as ultimate strain (E_{ult}). Dissipation energy (U) was defined as the area underneath of the stress-strain curve till the certain level of strains. We calculated the dissipation energy at 3.5 %, 5 % and 15 % strains.

2.2.6 Finite element analysis

3D μFE-models were generated from the geometry of the scanned specimens using the gmsh software [183]. The point clouds corresponding to the contours of each specimen were extracted from the μCT image using isosurface module in bonej with the resampling number equals to 2 [180]. We calculated the triangular surfaces by considering the resampling number of 1 and 2, and we found out less than 1 % difference between them. We used resampling number of 2 as it can reduce the number of element and consequently simulation time significantly. Isolated pixels were removed using corresponding filters in meshlab [184] and defining the maximum diameter of 15 for the isolated pixels. The number of triangle faces were reduced with the quadric edge collapse decimation filter in meshlab [184] to have about 200,000 faces. Self-interface surfaces were removed in geomagic software [185]. Second-order tetrahedral elements with frontal algorithm were used for 3D meshing in gmsh; finally, the mesh was optimized. Each FE-model has about 200,000 second-order tetrahedral elements. The elastic modulus of the FE-model was calibrated based on the experimental results. The numerical analyses were performed in Abaqus [186]. Von Mises elastic perfectly

plastic material models were used for the FE model. The initial guess (40 MPa) for the microscopic yield stress for each element was chosen from the specific strength, $\frac{\Sigma_{ult}}{\rho_n}$, of the experimental compression tests. FE-models were validated by the experimental compression tests, as shown in Section 2.3.3.

Once the FE-models had been validated, additional FE-models were built using image analysis operation on the original μCT-images in groups A and B. Erosion and dilation techniques were used for the construction of these new virtual FE-models. Erosion and dilation are basic mathematical morphology operations in the digital image processing of grayscale images. Dilation operation adds pixels to the boundaries of the object in the image, while erosion operation deletes pixels on the borders of the object [187]. These operations help to have artificial models with different levels of porosity and other morphological parameters with respect to the original samples. Erosion and dilation were performed in imagej; then, images were converted to FE-models. The intrinsic elastic modulus C_m used for the solid phase of the eroded and dilated models was the same as that used in FE models for group A and B. Finally, the effect of the microstructures on the mechanical properties have been studied.

2.2.7 Statistical analysis

A statistical analysis was carried out in R [188], and $p < 0.05$ was assumed as the significant level for the t-tests. The t-test has been performed between foam samples and their corresponding control group. Foam samples were also statistically tested in comparison with bone specimens. A linear regression model in logarithmic scale was fitted on the results to obtain the relation between the mechanical properties and other morphological parameters.

2.3 Results and discussion

2.3.1 Morphology

In total 30 foam specimens and 13 trabecular bone samples were tested in this study. As stated above, a homogeneous distribution of pores was expected for samples of group A, and a graded variation of pores for group B. Foam samples with non-elongated pore distribution were expected in group C and samples with elongated pores were expected in group D. Group A is a control set for group B and group C is a control set for group D.

Descriptive statistics of morphometric properties are listed in Table 2.2. The statistical difference between mean values of the morphological parameters of groups A vs. B and group C vs. D has been assessed using a t-test with a significance level $p = 0.05$.

The values which are statistically different are written with a bold font in Table 2.2. group B is statistically different from group A in three variables: the trabecular spacing, which represents the average size of cells, the connectivity density, which accounts for the number of foam strut in the volume, and the degree of anisotropy DA. Besides, it is evident from the μCT images that samples in group B have a graded distribution of morphological parameters along the length of the sample. These topological differences induce a different mechanical behavior under compression, which will be discussed in Section 2.3.2. Larger differences are found in group D compared to group C, in nearly all variables. Relative density, ρ_s for samples in group D is significantly higher than specimens in group C; this is owed to the rolling process. Samples in group D exhibit slightly higher ρ_s values and consequently lower strut spacing $St.Sp$ than samples in group C. The specific surface area (foam surface) of the foam per unit volume depends on the relative density (porosity), pore size and its distribution. Foam surface ratio was marginally higher for samples in group D compared to their control samples.

Tortuosity is an important factor for foams with insulation or thermal application [189, 190]. The parameter is nearly the same for specimens of groups A, B, and C, while samples in group D show slightly higher tortuosity. The structural material index (SMI) gives an estimation of the shape of the microstructures of foams. SMI for an ideal plate and rod structure is 0 and 3, respectively. The manufacturing process modifications induced with groups B and D does not change the original SMI value of the standard control groups. The degree of anisotropy (DA) can vary between 0 (isotropic) and 1 (anisotropic). Our results demonstrated that dispersal variation of pores is increased for rolled specimens in group D, compared to group C. From the DA calculation, microstructures of samples in groups A and B show a nearly isotropic distribution, while a significant anisotropy in the microstructures can be found in samples in group D. While the DA parameter indicates whether the cells are anisotropic, the normalized eigenvalue (m_3) indicates whether the cells are axially oriented (for large values) or not. The m_3 parameter says that foam samples are slightly axially oriented, and that group D has a more pronounced axial orientation.

Once all morphological parameters from the metal foams have been obtained, a quantitative and comprehensive comparison can be made between the typical topology of closed cell metal foams and the bovine trabecular bones. Trabecular specimens exhibit larger relative density, compared to standard foam samples. The rolling operation performed for specimens in group D allows to increase the relative density up to comparable values, and it is a simple, inexpensive operation for products with constant cross section. Samples in group D also exhibit the nearest degree of anisotropy DA to the trabecular bones and the largest m_3 parameter. Another geometrical parameter which

is very similar in metal foam and bone samples, is the SMI: both kinds of structures have, indeed, a mixed plate-like morphology.

The trabecular thickness of bones is smaller than that in aluminum foams, but in a comparable order of magnitude. This results in a consequently smaller trabecular strut spacing, meaning that, in this study, bovine bones show a larger number of smaller cells with thinner walls, with respect to metal foams.

Table 2.2: *Morphometric properties of foam samples in four groups and bovine trabecular specimens. Data are presented as a mean ± standard deviation. In the treatment columns B and D, bold numbers represent variables with a statistically significant difference ($p = 0.05$) with respect to the control groups.*

Morphometric properties	Group A	Group B	Group C	Group D	Bone
Relative density (ρ_s) [%]	16.62 ± 1.7	19.08 ± 2.1	28.22 ± 1.48	32.88 ± 2.16	34.14 ± 4.52
Strut (Trabecular) Thickness ($St.Th.$) [μm]	225.4 ± 7.02	216.8 ± 10.5	298.5 ± 25.03	345.9 ± 34.9	209.69 ± 17.70
Strut (Trabecular) Spacing ($St.Sp.$) [μm]	1619 ± 152.6	1414 ± 93.6	1778 ± 190.2	1307.6 ± 118.8	495.23 ± 48.7
$\frac{FS}{V}$ [$\frac{1}{mm}$]	12.66 ± 0.18	12.92 ± 0.63	8.13 ± 0.66	7.45 ± 0.82	12.96 ± 1.52
Connectivity density [$\frac{1}{mm^3}$]	0.93 ± 0.18	1.37 ± 0.38	1.89 ± 0.32	1.41 ± 0.20	5.72 ± 0.83
Tortuosity	1.14 ± 0.66	1.24 ± 0.86	1.77 ± 0.51	2.77 ± 0.90	0.85 ± 0.19
Structural Material Index (SMI)	1.71 ± 0.12	1.79 ± 0.21	1.23 ± 0.18	0.93 ± 0.21	1.57 ± 0.19
Degree of Anisotropy (DA)	0.29 ± 0.08	0.20 ± 0.04	0.23 ± 0.08	0.37 ± 0.04	0.60 ± 0.09
m_3	1.13 ± 0.04	1.08 ± 0.08	1.13 ± 0.04	1.18 ± 0.03	1.51 ± 0.18

The two proposed modifications of the standard manufacturing processes have mixed effects in enhancing the biomimicry of metal foams. These effects can be seen in the Figure 2.4, where the % difference of the average value of each parameter is shown, compared to the same parameter measured for bones. From the point of view of mechanical strength, the two most important morphometric parameters are the relative density ρ_d and the m_3 directionality parameter. Group D exhibits the lowest deviations of these two important variables, if compared to other groups: ρ_d is also the same in

statistical sense, while m_3 is still larger for natural bones. Group D can still be considered the most biomimetic structure (among the four tested), with respect to axial mechanical strength. A larger number of rolling passes or a more severe deformation per pass could be applied in order to further increase the m_3 value of metal foams.

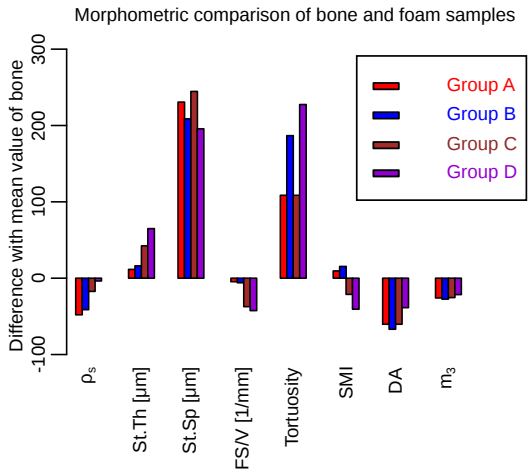

Figure 2.4: *Percentage differences of average values of morphometric parameters of closed cell metal foams with respect to the bovine bones.*

2.3.2 Compression testing

Compression tests were conducted on all the available foam and bone samples. The stress-strain curves obtained from compression tests are shown in Figure 2.5. It is very interesting to observe that all curves plotted in Figure 5 share some common behaviors: they all have a very small linear elastic part with a yield stress $\Sigma_{y0.2}$ (reported in Table 3), which is always below 10 MPa; they all reach a peak stress value Σ_{ult} (always below 20 MPa) after a similar amount of straining E_{ult}, which is always ranging from 3 to 5 %. They all show a densification, i.e. the stress starts growing again, always before reaching a level of 15 % strain. For this reason, we stopped the tests after reaching 15 % of strain.

Macroscopic mechanical properties of foam samples and trabecular bones are presented in Table 2.3. No significant difference was found between mechanical properties of samples of group B with respect to its control group A. Elastic stiffness, strength and yield stress in group D are significantly higher than samples in the control group C. Ultimate strains for the samples in groups C and D are similar.

As already shown for morphometric parameters, a similar comparison can be made for mechanical properties, shown in Figure 2.6. This comparison indicates that group D, which can be considered the most biomimetic group of the sample from a morpho-

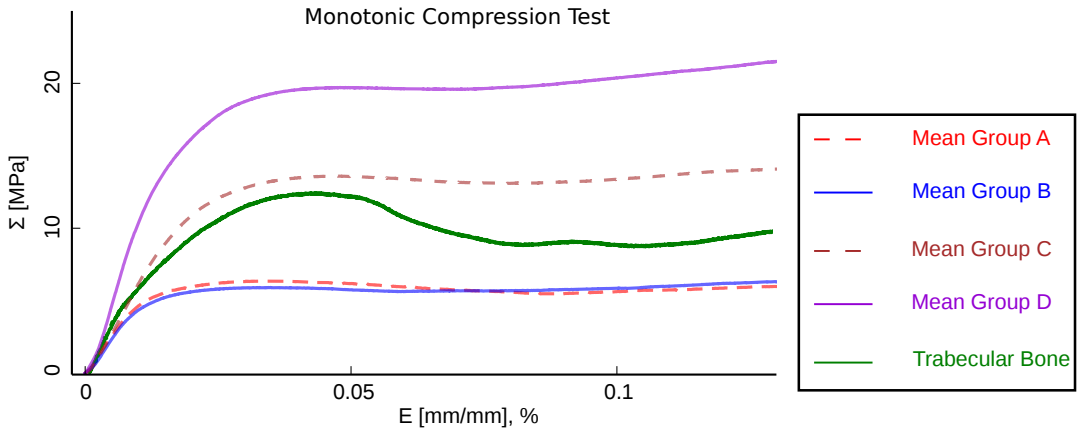

Figure 2.5: *Average stress-strain curves for aluminum and trabecular bovine samples for monotonic compression tests. Group A: homogeneous distribution of pores, group B: graded distribution of pores, group C: isotropic distribution of pores, D: elongated pores using rolling.*

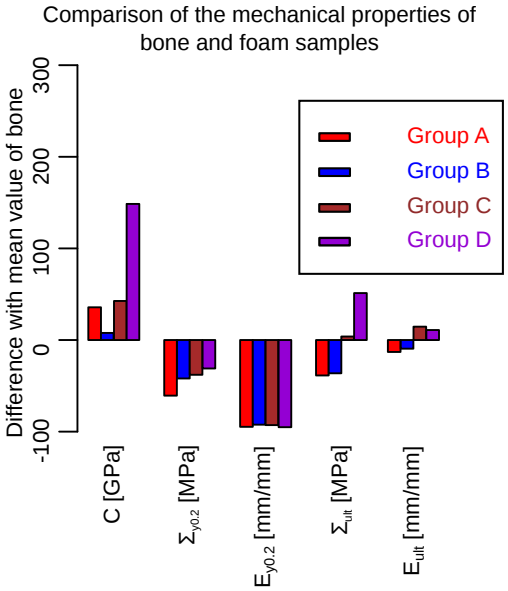

Figure 2.6: *Average stress-strain curves for aluminum and trabecular bovine samples for monotonic compression tests. Group A: homogeneous distribution of pores, group B: graded distribution of pores, group C: isotropic distribution of pores, D: elongated pores using rolling.*

metric point of view, well mimics two mechanical parameters: the yield stress and the ultimate strain of bones. Group D also shows closer $\frac{C_a}{C_0}$ property to bone compared to other aluminum groups. The inherent elastic modulus of aluminum foams calculated by nano-indentation tests, according to the scientific literature [191] is very close to the nominal $C_0 = 70$ GPa value. For bones, this value is reported as 20 GPa [192]. Groups A-B better mimic the elastic modulus, whereas group C well reproduces the ultimate

Table 2.3: *Apparent mechanical properties of the monotonic compression test of closed-cell aluminum foam samples and bovine trabecular bone. In the rows showing the results of groups B and D, bold numbers represent variables with a statistically significant difference with respect to the control groups A and C. C_0 for aluminum and bone samples are assumed to be 70, and 20 GPa, respectively.*

Sample	C_a [GPa]	$\frac{C_a}{C_0}$	$\Sigma_{y0.2}$ [MPa]	Σ_{ult} [MPa]	E_{ult} [$\frac{mm}{mm}$], %	U [$\frac{MJ}{mm^3}$]
Group A	0.80 ± 0.44	0.011	3.38 ± 1.5	6.47 ± 1.38	3.48 ± 0.82	1.07 ± 0.43
Group B	0.62 ± 0.17	0.009	3.91 ± 1.41	5.98 ± 1.56	3.30 ± 0.49	1.16 ± 0.57
Group C	0.96 ± 0.20	0.013	5.41 ± 3.91	13.72 ± 1.66	4.50 ± 0.83	1.86 ± 0.21
Group D	1.67 ± 0.69	0.024	6.01 ± 5.09	19.98 ± 3.56	4.65 ± 0.83	2.81 ± 0.52
Bone	0.67 ± 0.26	0.034	8.71 ± 4.36	13.21 ± 4.07	4.06 ± 1.04	1.50 ± 0.42

stress.

According to the results discussed thus far, bovine trabecular bones have both a graded distribution of porosity and cell size, and axially elongated cells. The produced metal foam samples capture either one or the other of these two morphological parameters but not both. Groups C and D performed well for the Σ_{ult} (i.e. similar to trabecular bone). As they also performed well with the relative density, this brings us to the conclusion that the yield stress of this sintered aluminum material is reasonably close to the intrinsic yield stress of the bone tissue, while a higher mismatch between intrinsic elastic moduli for bone and aluminum is found. Since the proposed treatments are sequential, i.e. one treatment is performed while foaming (graded distribution of pores) and one treatment is performed post-foaming (anisotropy induced by rolling), they can easily be combined. In other words, a closed cell sample with both graded distribution and anisotropy of properties should be producible.

Mechanical properties of cellular materials follow a power law relation with the relative density [40, 41, 110] (Eq. 2.2).

$$\mathbf{X} = \mathbf{X}_0 \alpha \rho_s^n \tag{2.2}$$

Where $\mathbf{X}$ is the effective mechanical properties, $\mathbf{X_0}$ is the mechanical properties of the solid constituent, and ρ_s is the relative density; α and n are material constants. The same kind of law could be generalized, through linear regression analysis of logarithmic terms, to a more comprehensive formulation:

$$X = X_0 \alpha \prod_i \theta_i^{n_i} \tag{2.3}$$

Where θ_i is any independent geometrical parameter of the ones listed in Table 2.2. However, the statistical analysis yielded by the linear regression has shown that signifi-

cant correlation can be found, with the available data, only between the strength and ρ_s. Indeed, due to a limited range of variation of the morphometric parameters, no statistically significant correlation has been found, except for the relative density. Particularly interesting is the model obtained for the ultimate compressive strength Σ_{ult}, where all four foam groups can be pooled together into a unique model (Figure 2.7). This model can be compared to a similar model obtained for bovine bones: the n-values for both models are very close, being equal to 1.79 and 1.67, respectively.

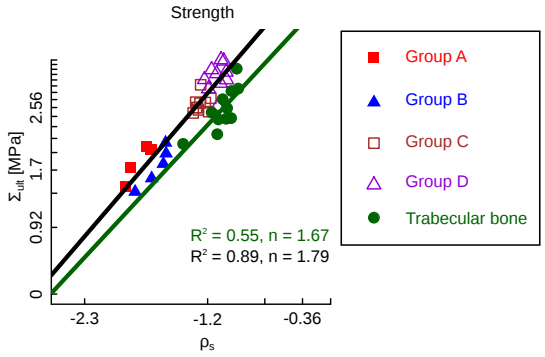

Figure 2.7: *A linear regression model (in logarithmic scale) of foam and bone samples. Samples in all four aluminum groups are pooled.*

We also normalized the strength data (Σ_{ult}) for samples in Group C and D to $\rho_s^{1.79}$. The mean ± standard deviation for normalized strength for samples in Group C and D was 132.51 ± 17.42 MPa and 146.92 ± 26.63 MPa, respectively. This shows that the hot rolling process mainly affect the apparent density only with the relevant increase of the ultimate strength.

2.3.3 Finite element simulation

To overcome the limitation of the available experimental range of morphological parameters, which is obviously bounded by technical and economic constraints, additional 'virtual' experiments have been run by means of FE-simulations, after proper validation of the model.

A linear elastic-perfectly plastic material property was considered for the μFE simulation of axial compression tests. The displacement control simulation was done by applying a 1.2 mm displacement (7 % of strain) on a reference point defined on the top of the model. Kinematic coupling was considered between the reference point and the node sets on the upper part of the mesh of the samples. The FE-simulation was limited to small strains, because only in that region the FE-model is reliable, where no significant damage yet occurs to the foam metal walls. A clamped boundary condition

was considered for the set of nodes at the opposite side of the model. The geometrical nonlinearity was included in the analysis.

The solid metal in the foam is obtained through a sintering process which may result in a micro or nano-porosity well below the resolution of the CT scans. For this reason, an elastic modulus lower than that typical of the aluminum ($C_0 = 70\ GPa$) can be expected for these samples. Similar considerations hold for the yield stress. A direct experimental estimation of the mechanical parameters (Elastic modulus and yield stress) for the sintered aluminum as that obtained in the foaming process cannot be technically performed; therefore, an inverse estimation by comparing finite element simulation and experimental results of compression tests on foam samples has been carried out. One elastic modulus for the solid phase in the finite element model was identified for each experimental stress-strain curve. To this purpose a linear fitting of the loading curve between the 0 % strain and the 2 % strain was performed on each experimental curve; a similar curve fitting was made of the simulated stress-strain curve for each specimen. The Young's modulus in the finite element model was identified so to match the elastic stiffness of the models with that found on the experimental data. Eventually, to have one single elastic stiffness for all the FE-models, a mean calibrated elastic stiffness, equal to $C_m = 5.01$ GPa, was chosen for the solid phase in the model. This is in line with the results of [163], which also did FEM simulations of compression tests.

Based on Eq. 2.2, $\frac{X}{\rho_s}$ shows the mechanical properties of the solid constituent. Therefore, we normalized the apparent experimental stresses to $\rho_s^{1.79}$ in order to obtain the mechanical properties of the solid constituent. Subsequently, we calculated the mean yield stress of the normalized stress curve ($\frac{\Sigma}{\rho_s^{1.79}}$). Microscopic yield stress was obtained as 40 MPa, and it was considered as the yield stress in the von Mises plasticity model for the solid phase. FE-simulations have been performed for samples in group A and B.

The macroscopic elastic stiffness, compressive strength, and energy dissipation obtained from FE-models and experiments were compared in Figure 2.8. The μFE model can predict the compressive strength reached in experiments with a root mean square error equal to 0.76 MPa, and $R^2 = 73.4\ \%$. The corresponding values for the elastic stiffness were $RMSE = 0.1$ GPa and $R^2 = 50\ \%$, and $RMSE = 0.016\ \frac{MJ}{mm^3}$ with $R^2 = 79.6\ \%$ for the dissipation energy. From the comparison of FE and experimental results, it can be concluded that the current FE-model is appropriate for the estimation of the initial yielding and the compressive strength. FE-models of original specimens in groups A and B were used for the creation of new models (virtual samples) representing additional foams with new values of relative density. Erosion and dilation images

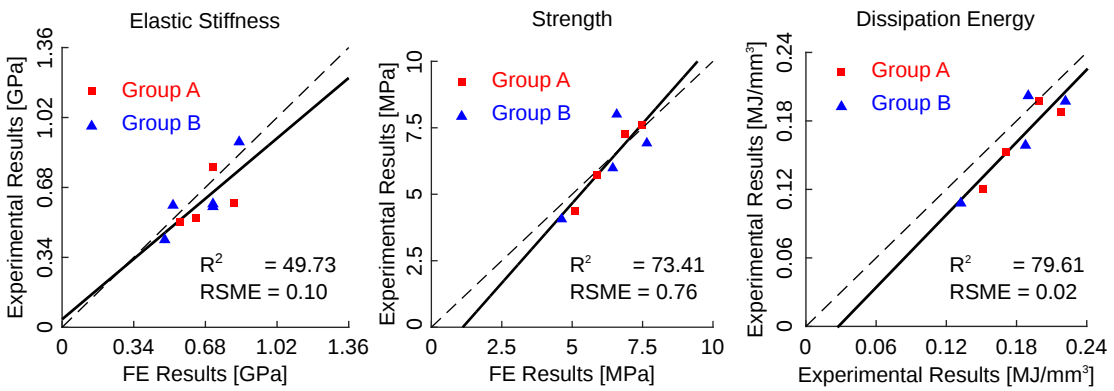

Figure 2.8: *Comparison of the numerical results with the experimental data for the elastic stiffness, strength, and energy dissipation; dashed lines are the regression 1:1 lines.*

analysis were used for the creation of these new models. Erosion resulted in samples with higher porosity and a lower strut thickness, while dilation produced samples with higher strut thickness and the relative density. The general shapes of the cells did not change for the artificial samples.

Morphometric comparison of the virtual and original samples was illustrated in Figure 2.9. The comparison between morphology of virtual and original sample shows artificial samples have different levels of porosity and strut thickness, and there is a linear correlation ($R^2 = 87.7$) between the two parameters. As the shape of pores did not change significantly, erosion and dilation do not significantly alter the DA and m_3 values of real samples.

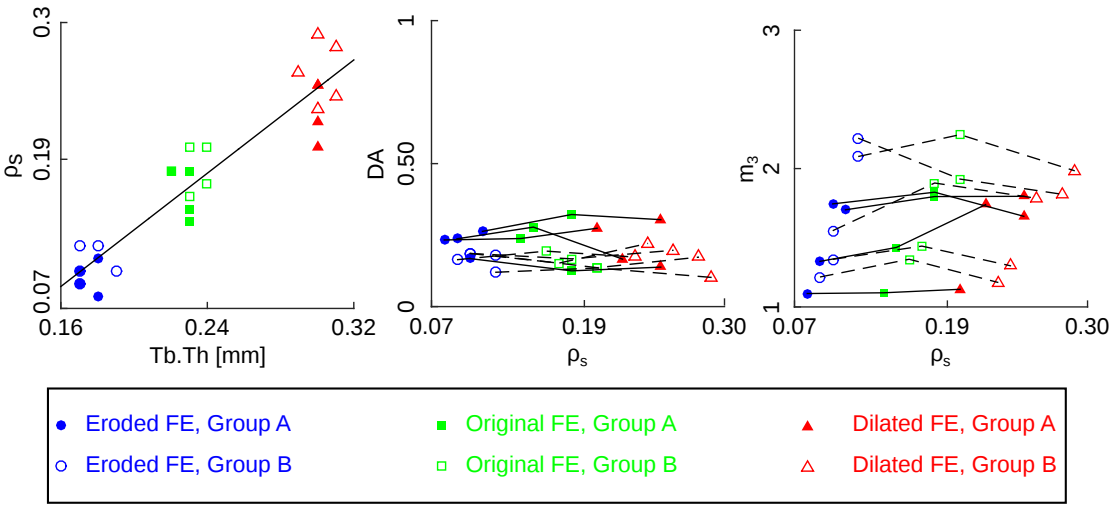

Figure 2.9: *Morphology of the artificial foam samples produced from original images in groups A and B.*

As we were able to expand the range of porosity with the new virtual samples, we compared the numerical results for different mechanical properties. Then, using an ANOVA fit and considering the samples of two groups, we fitted a fabric based model on data. The model shows that although main mechanical properties of the foam samples can be well predicted by the relative density only (as in Eq. 2.2), adding the eigenvalue m_3, which is a replica of the architecture the prediction improves:

$$X = X_0 \alpha \rho_s^p m_3^q \tag{2.4}$$

The dependence of stiffness C_a, strength Σ_{ult}, and energy U on the density ρ_s and m_3 is graphically summarized in Figure 2.10 and Figure 2.11. The 2-parameters and 3-parameters models are summarized in Table 2.4. As a comparison, Charlebois et al. [120] found $p = 1.55$, $q = 1.61$ with $R^2 = 0.78$ for the elastic stiffness, estimated for human trabecular bones. The n-values are very similar, while for metal foams the q-value is significantly smaller, i.e. the stiffness of metal foam is less sensitive to the m_3 parameter.

Table 2.4: *Two different models were used for the fit. In first try, $X = X_0 \alpha \rho_s^n$ is used. In the second fit, a fabric based model equal to $X = X_0 \alpha \rho_s^p m_3^q$ is considered.*

	2-parameters model			3-parameters model			
Mechanical properties, x	n	α	R^2	p	q	α	R^2
Elastic stiffness, C_a [GPa]	1.39	0.10	0.90	1.40	0.29	0.09	0.96
Strength, Σ[MPa]	1.47	0.24	0.90	1.42	0.24	0.20	0.94
Dissipation energy, U [$\frac{MJ}{mm^3}$]	1.46	1.80	0.90	1.42	0.24	1.51	0.95

Among natural cellular materials, trabecular bone constituents have compositions, shapes, sizes and spatial distribution, which lead to multiscale hierarchical structures. In addition to the relative density, topological irregularities, shapes and size of the cells, and heterogeneity can affect the behavior of cellular materials. The scaling relationship in cellular materials can be changed through the geometry of the microstructures rather than composition in an architected design. This can be seen from the power law we used for the prediction of strength in aluminum foams and trabecular bones. Both materials show similar scaling relationship.

2.4 Conclusions

Natural cancellous bones have a complex hierarchical microstructure, which provides several functions. From a mechanical point of view, the load-bearing abilities of trabecular bones are characterized by an anisotropic morphology (i.e. cells are oriented

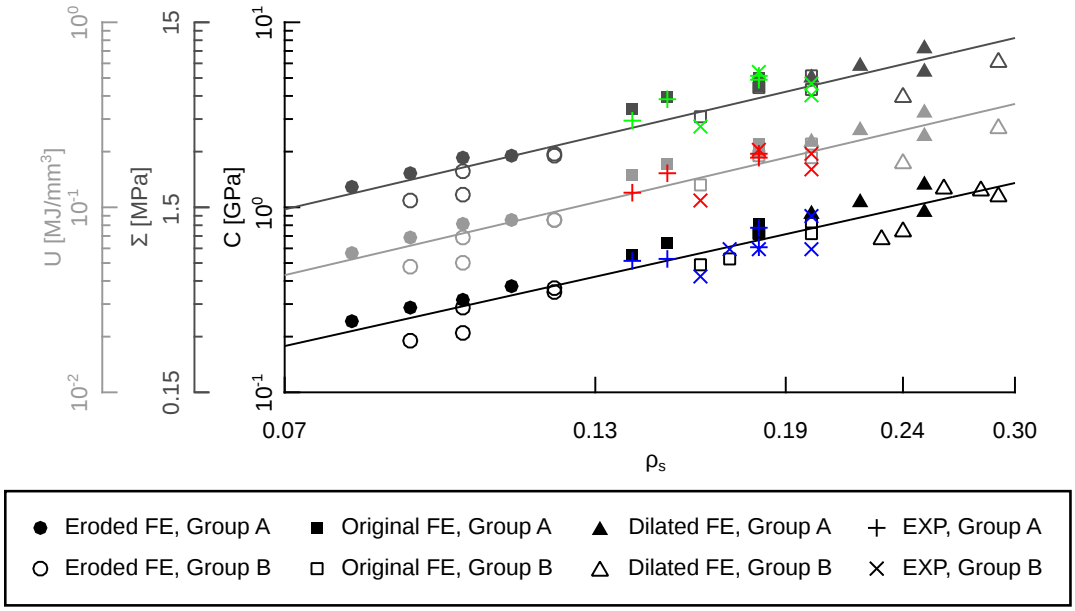

Figure 2.10: *Linear correlation of the mechanical properties and the relative density in the logarithmic scale. Model is fitted on the pooled data. The colorful data show experimental results of groups A and B.*

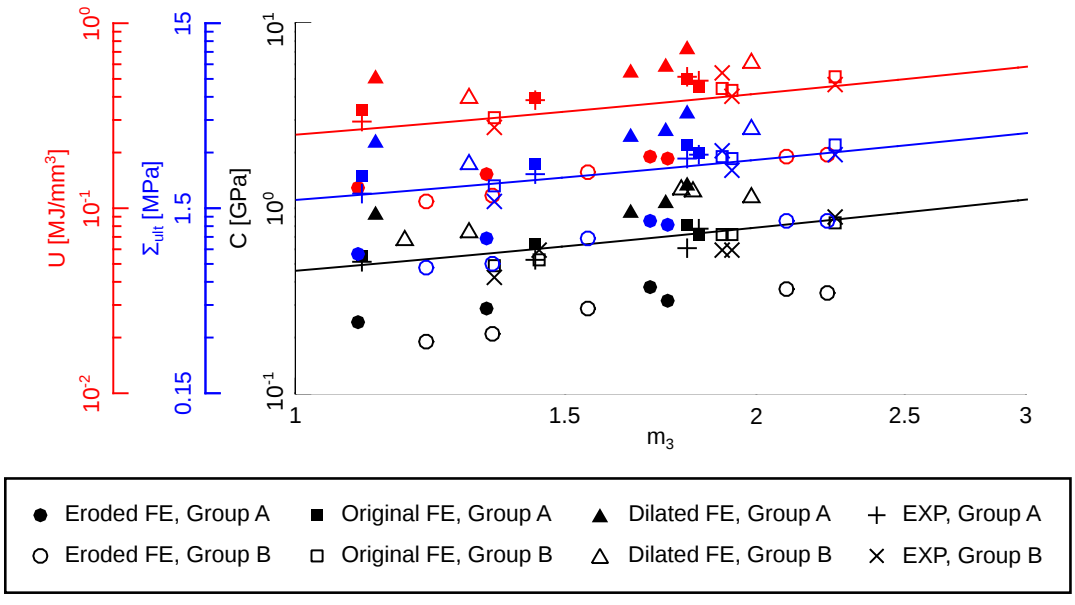

Figure 2.11: *Linear correlation of the mechanical properties and the m_3 in the logarithmic scale. Model is fitted on the pooled data.*

in the direction of the prevalent load) and by a graded distribution of pore size. In this study, inspired by the mimicking of the trabecular microstructures, we developed and tested two innovative manufacturing processes for producing closed-cell aluminum

foams, by modification of the standard process. Small rod or bar-shaped samples were manufactured, in order to be comparable with available cylindrical bone samples. The standard process is the expansion of a foaming agent in a semi-solid metal aluminum matrix. In the first modified design (group B) a graded variation of pore size along the axial length of foams was introduced. In the second design (group D), we elongated the pores along the axial length, by hot rolling of small prismatic bars, in order to induce microstructural anisotropy as in the cylindrical trabecular specimens. The samples B and D were compared to standard control groups, respectively called A and C.

The microscopic geometrical properties and the mechanical properties under axial compression of foams B and D were measured by μCT imaging and their morphometric parameters compared to control groups and to trabecular bones. Morphologically, group B had only little differences from its control group A. In terms of biomimicry, i.e. similarity to trabecular bovine bones, groups A and B can be pooled together. The most biomimetic morphometric parameters for groups A-B are the strut thickness $St.Th.$ and the surface-to-volume $\frac{FS}{V}$ ratio. However, they have a lower relative density ρ_s and a lower axial orientation m_3. On the contrary, the morphology of group D resulted significantly different than its standard control group C. group D resulted more biomimetic in two important morphometric parameters: the relative density Ïs and the axial orientation m_3. The other geometrical parameters of group D, on the contrary, were less biomimetic than groups A-B.

The comparison of mechanical elastic properties for samples in the different groups shows that specimens with elongated pores in group D have properties closer to bones, especially with respect to the $\frac{C}{C_0}$ (ratio between elastic stiffness of the porous material and elastic stiffness at the micro level). This shows that the manufacturing procedure is able to reproduce some mechanically relevant geometric features of the porous structures, similar to the trabecular bone.

According to the study, bovine trabecular bones have both graded distribution of porosity and cell size, and anisotropy (i.e. axially elongated cells). The produced metal foam samples capture either one or the other of these two morphological parameters but not both. A closed cell foam sample with both graded distribution and anisotropy of properties should be easily producible, providing an enhanced biomimicry.

In the second part of the paper, the power of FE-simulations combined with image analysis (μCT 3D reconstructions) has been applied for building virtual μFE-models that can be used in homogenization and micromechanical studies. These models can also help designers to understand the effect of microstructures and can serve as a design guideline. In this case, the μFE-models were very useful because the available range of morphometric parameters (especially the relative density) was not sufficient to

develop a comprehensive correlation between mechanical properties and morphology of microstructure. The μFE-models were carefully calibrated, and similar micro-elastic properties were considered for each FE-model. The models are able to accurately replicate the behavior of groups A-B in the low strain region. The FE-models were then used to create new virtual compression tests on a broad range of relative density values.

Correlation models, based on the power law, were developed among the main mechanical performance of foams (stiffness, strength, absorbed energy) and the morphometric parameters (relative density ρ_s and an axial orientation m_3). Surprisingly, the power law relations for closed cell aluminum foam were very similar (in terms of exponents of the independent variable) to the models developed for trabecular bovine bones and even more similar to a model (found in the literature) of trabecular human bones.

In conclusion, the study has shown that closed cell aluminum foam can be produced with biomimetic uniaxial mechanical properties in the low strain region, by controlling their relative density and the axial orientation of their cells.

CHAPTER 3

Effect of Randomness in the Design Process of Cellular Structures

From the manuscript published as[1]

3.1 Introduction

Mechanical metamaterials [45, 60, 68, 193] are materials for which small-scale topological design determines the large-scale properties. It is, therefore, possible to adjust the topological design of such materials to obtain the desired set of mechanical properties including some unusual properties such as negative Poisson's ratio [63], negative compressibility [45], ultrahigh stiffness [194], and fluid-like behavior [195]. Rational design is the process of applying physical principles, analytical solutions, and computational models to devise the topological design that gives rise to the desired set of mechanical properties [196–199].

As far as the elastic properties of isotropic metamaterials are concerned, different topological designs result in different values of the elastic modulus and Poisson's ratio. It is, of course, possible to consider other duos of the elastic properties such as

[1] M. J. Mirzaali, R. Hedayati , P. Vena, L. Vergani, M. Strano, A. A. Zadpoor, Rational Design of Soft Mechanical Metamaterials: Independent Tailoring of Elastic Properties with Randomness, *Appl. Phys. Lett.*, 111, 051903 (2017); doi: http://dx.doi.org/10.1063/1.4989441

the elastic modulus and shear modulus or the bulk modulus. We will, however, use the elastic modulus and Poisson's ratio here due to their practical importance. While the elastic modulus is often used to evaluate the load-bearing capacity of the material, the Poisson's ratio in general and auxetic metamaterials in particular [200–204] are instrumental in designing mechanical metamaterials with advanced functionalities [200,203].

Many applications of mechanical metamaterials require simultaneous adjustment of both elastic modulus and Poisson's ratio which is possible through the recent development in additive manufacturing technologies in general and dual-material additive manufacturing in particular [205]. However, topological designs that result in favorable values of one property may adversely affect the values of the other. For example, it has been shown that topological designs that decrease the Poisson's ratio to large negative values that are desired for many applications result in decreased values of the elastic modulus [200, 203]. It is therefore important to find rational design approaches through which elastic modulus and Poisson's ratio could be independently adjusted within a wide range of values.

In this study, we propose an approach based on random distribution of auxetic (re-entrant hexagonal honeycomb) and conventional (periodic hexagonal) unit cells in soft cellular metamaterials to cover particular areas in the elastic modulus-Poisson's ratio plane that cannot be covered with a simple arrangement of the same unit cells. The main hypothesis, therefore, is that "patterned randomness could be used as a rational design tool to achieve a wide range of elastic properties while keeping the unit cell design constant". We also propose an inexpensive method based on hobbyist 3D printer for indirect additive manufacturing of the proposed soft metamaterials. As it is generally not possible to print highly elastomeric materials with hobbyist 3D printers, the proposed manufacturing approach could facilitate the research and practical application of soft mechanical metamaterials.

3.2 Materials and Method

3.2.1 Samples Preparation and Geometries

The general dimensions of the auxetic (A-UC) and conventional (C-UC) unit cells are presented in Figure 3.1a and d. Eight samples were manufactured to validate the numerical simulations. These eight samples contain two samples with either fully conventional or auxetic lattice structures (Figure 3.1a). The rest of six samples contained randomness in their microstructures which will be discussed in Section 3.2.2 and are illustrated in Figure 3.1b and c.

The topological design of the specimens in a CAD program (Solidworks) was used

to create individual molds. A mold was designed and additively manufactured using a fused deposition modeling (FDM) 3D printer (Ultimaker 2+, Geldermalsen, The Netherlands) from polylactic acid (PLA) filaments (MakerPoint PLA 750 gr Natural). Subsequently, an elastomeric polymer (Elite Double 8, Zhermack, Badia Polesine, Italy) with a one-to-one ratio of the base to catalyst was poured into the mold. Once the specimens had cured (after about 1 hour), they were transferred to a grinding machine to remove the support layer and redundant particles from both sides of the panel. The final products are shown in Figure 3.1.

In the development of these unit cells, we assumed that total length and width of both unit cells are constant. The only parameter that could change the geometry of both unit cells was the interior angle (θ) of each unit cell (see Figure 3.1). Due to geometrical constraints (Table 3.1), the angle of unit cells could vary between 55°and 130°.

Table 3.1: *The geometrical parameters of the conventional or hexagonal (C-UC) and auxetic or re-entrant (A-UC) unit cells in this study.*

Unit cells	$h\,[mm]$	$l\,[mm]$	$w\,[mm]$	$t\,[mm]$	$L\,[mm]$	$W\,[mm]$	$t_{lattice}\,[mm]$
A-UC/ C-UC	9	7.5	16.5	0.9	132	120	13

3.2.2 Introducing Randomness in the Fully Conventional (Auxetic) Lattice Structures

The final lattice structure contained a random combination of hexagonal and re-entrant unit cells. We propose two main algorithms to introduce randomness into the lattice structure, which is detailed in (Table 3.2) and Figure 3.1b and c. These two algorithms are defined as: i) fixed level of randomness, ii) patterned randomness. The idea of implementing the randomness means how hexagonal unit cells can randomly be replaced with re-entrant ones in a fully auxetic lattice structure.

Fixed Level of Randomness

For specimens in this group, we considered a uniform distribution of randomness. For this purpose, we selected three levels of randomness as 25 %, 50 %, and 75 %. These values show the probability that a unit cell in a fully A-UC lattice structure is replaced by a C-UC.

To create these samples, first, we considered a random number from a Gaussian distribution. The random number was generated between $(-1 + \frac{PR}{100}, \frac{PR}{100})$ where PR

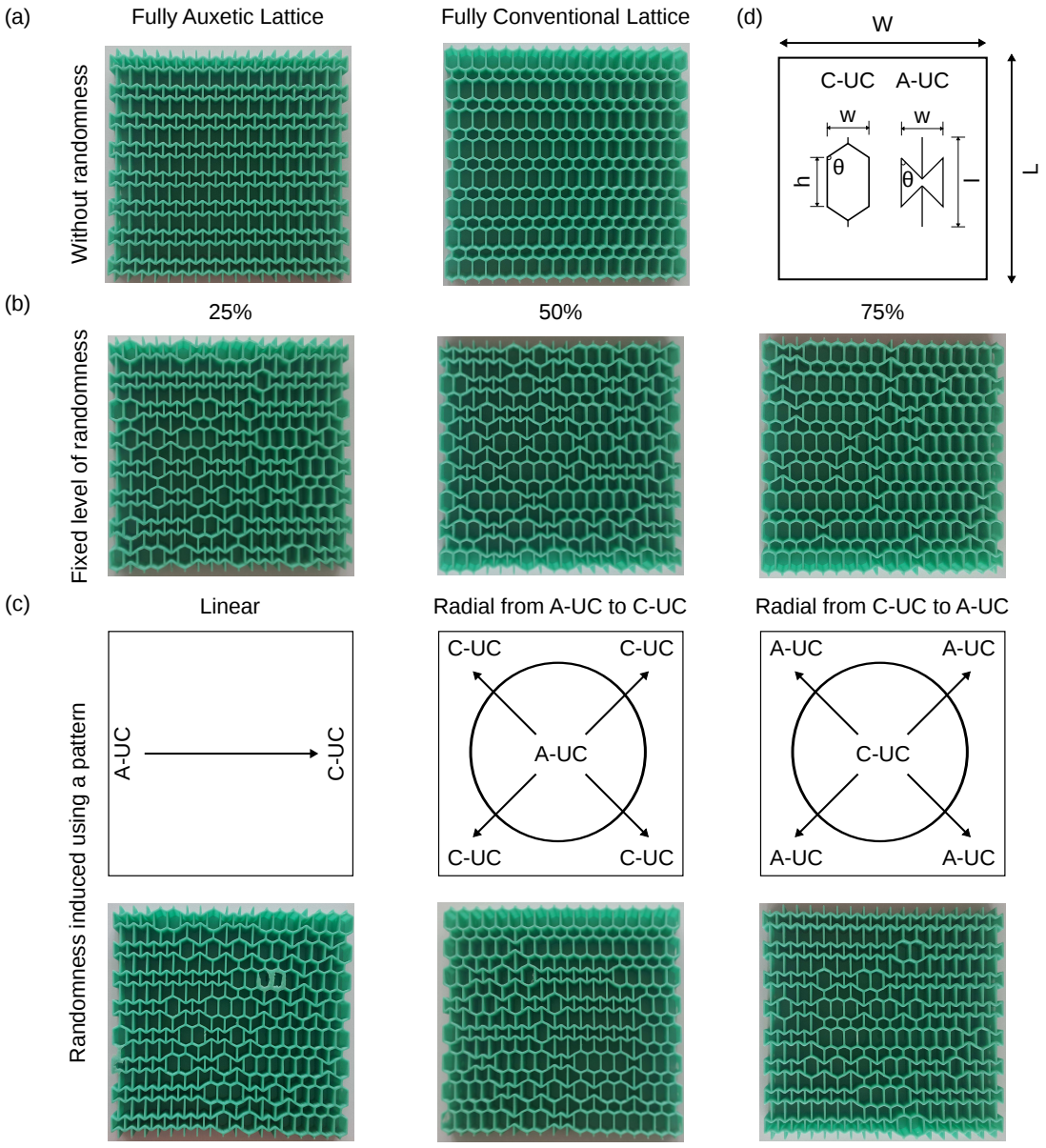

Figure 3.1: *Elastomer lattice structure with (a) regular and (b and c) random distribution of unit cells. Dimensions of the conventional (C-UC) and auxetic (A-UC) unit cells and the dimension of the whole lattice structure are shown in (d). Total length and width of both unit cells (i.e. l and w) are kept constant. By changing the interior angle (θ) of unit cells, different geometries can be constructed. θ can vary between 55°to 130°. Additional parameters are presented in Table 3.1.*

stands for the percentage of randomness (Table 3.2). The generated number shows the incident probability of a conventional unit cell in a fully auxetic lattice structure, as it is shown in Equation 3.1.

$$\begin{aligned} \text{for} X \in [-1 + \frac{PR}{100}, \frac{PR}{100}] \\ \text{if} X > 0 \\ \text{Replace C-UC in a fully A-UC lattice} \\ \text{if} X \leq 0 \\ \text{Keep A-UC in a fully A-UC lattice} \end{aligned} \tag{3.1}$$

For instance, in the case of a lattice with the randomness level of 25 %, for each unit cell, a random number was created in the range of -0.75 and 0.25. For every random number greater than zero, a conventional unit cell was positioned in the lattice structure, while random number below zero resulted in an auxetic unit cell being added to the lattice structure (Figure 3.1b).

Patterned Randomness

In the second group, we introduced randomness in the structure using linear or radial patterns. A schematic illustration of each model is presented in Figure 3.1c.

In the case of patterned randomness, conventional unit cells were replaced in a fully auxetic lattice structure by either linear or radial distributions. These patterned randomnesses were introduced using the formulae provided in Table 3.2 where i and j respectively represent the column and row number, while m and n stand for the total number of columns and rows, i.e. $nw = W$ and $ml = L$.

Table 3.2: *Summary of the randomness distribution type in the lattice structures.*

Randomness distribution	Range used for creation of the random numbers
Uniform 0 % (A-UC)	$(-1, 0)$
Uniform 25 %	$(-0.75, 0.25)$
Uniform 50 %	$(-0.5, 0.5)$
Uniform 75 %	$(-0.25, 0.75)$
Uniform 100 % (C-UC)	$(0, 1)$
Linear pattern	$(-1 + \frac{j}{n}, \frac{j}{n})$
Radial pattern (C-UC to A-UC)	$(-1 + 2\sqrt{(\frac{i}{m} - \frac{1}{2})^2 + (\frac{j}{n} - \frac{1}{2})^2}, 2\sqrt{(\frac{i}{m} - \frac{1}{2})^2 + (\frac{j}{n} - \frac{1}{2})^2})$
Radial pattern (A-UC to C-UC)	$(-2\sqrt{(\frac{i}{m} - \frac{1}{2})^2 + (\frac{j}{n} - \frac{1}{2})^2}, 1 - 2\sqrt{(\frac{i}{m} - \frac{1}{2})^2 + (\frac{j}{n} - \frac{1}{2})^2})$

In the linearly patterned random structures, the probability of having A-UC on the left side of the structure was higher than C-UC. This probability decreased linearly and made to have more C-UC at the very right end section of the structure (Figure 3.1c).

This will happen by choosing a random number between the range of $(-1 + \frac{j}{n}, \frac{j}{n})$. For instance, at one side of the samples, where $n = 1$, the random number will be generated between (0,1), that means higher chance of having C-UC. However, as we move toward the other side the sample, that range will change to (-1,0), that means higher chance for having A-UC.

A similar concept was used to introduce a radial random pattern into the structure. In the case of radial randomness from A-UC to C-UC, the probability of having A-UC in the center of the structure was maximum. This probability decreases radially and reaches the minimum likelihood of having A-UC at the boundaries of the lattice structure (Figure 3.1c). For this case, we used the formula of circle to introduce the randomness in the structure (Table 3.2).

3.2.3 Experimental Testing

Eight samples were fabricated to validate the numerical simulations (Figure 3.5) that will be discussed in Section 3.2.4 and 3.3. The specimens were tested under quasi-statically applied monotonically increasing tensile load using an INSTRON e10000 dynamic test machine. The experiments were displacement-controlled and were performed at a rate of $4\ \frac{mm}{min}$.

To attach the specimens to the grippers of the testing machine, two connecting parts were designed and additively manufactured using the same PLA filament and 3D printer as noted in Section 3.2.1. The connector worked as a hook. The first and the last rows in the unit cells were fitted in the connector. Then, the outer side of the connector was designed in such a way that the grippers of the testing machine could fully grip the connector (Figure 3.2).

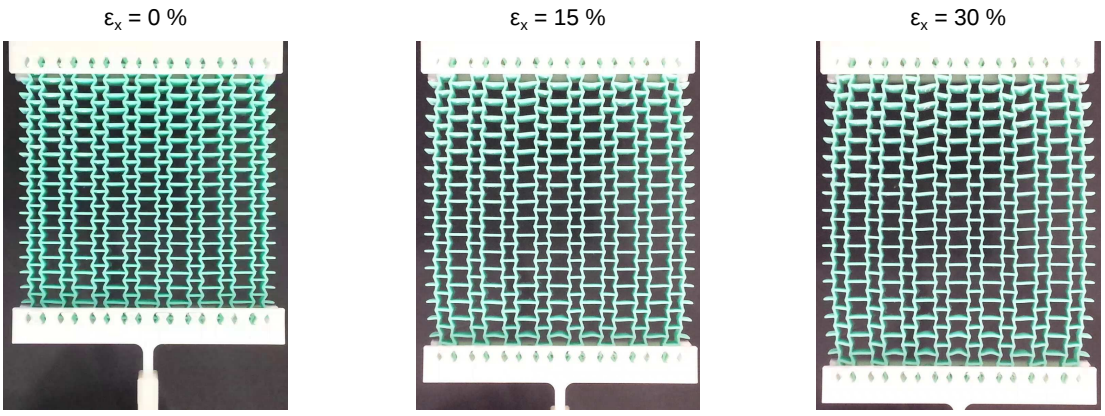

Figure 3.2: *Experimental fixture to perform tensile testing in this study. Deformation of fully auxetic lattice structure is presented under three levels of strain, i.e. 0 %, 15 % and 30 %.*

The nominal stress (σ) was defined as the ratio of the applied force to the initial area (A_0). The axial strain (ε) was defined as the proportion of the displacement to the free length between two connectors (W). The elastic modulus (E) was calculated from the slope of a linear fit to the stress-strain curve until 5 % strain.

3.2.4 Numerical Modeling

Numerical simulation and modeling were performed in ANSYS® Academic Research, Release 16.2, software. A hyperelastic (Mooney-Rivlin) material model ($E_s = 0.721$ MPa, ν_s =0.49, C_{10} =103927.05 Pa, C_{01} =-2591.52 Pa) was used for the simulations. The coefficients of the material model were determined based on the standard experimental protocols for testing elastomeric materials in tension (ASTM D412 Type C) and compression (ASTM D 575-91, Standard Test Methods for Rubber Properties in Compression). Timoshenko beam elements with rectangular cross-sections and constant thickness ($t = 0.9$ mm) were employed for discretizing the geometries of the finite element (FE) models (Figure 3.3). The out-of-plane thickness of the lattice structure ($t_{lattice}$) was set to 13 mm.

Similar boundary conditions were applied to all FE models. Consistent with the experimental configurations and mechanical testing setup, the nodes located in the first row on the left side of the structure were fixed in all directions. A constant displacement in the x-direction was applied on the right side of the geometry. The nodes located on the right side of the structure were constrained in both Y and Z directions (Figure 3.3). A non-linear solver was used for the simulations.

One thousand simulations were performed for each type of introduced randomness. A constant level of displacement equal to $U_x = 2.5\ mm$ was applied to the FE models. The total reaction force (F) was then used to calculate the elastic modulus of the structure. The lateral expansion/contraction was measured for each row of the lattice structure ($U_{(y,j)}$) and the average value of the lateral displacements measured for different rows (U_y) was used to calculate the Poisson's ratio of the structure. The nominal stress (σ) was defined as the ratio of the applied force to the initial area ($A_0 = L \times t_{lattice}$). Axial strain ($\varepsilon_x$) and local lateral strains (ε_y) were respectively determined by $\varepsilon_x = \frac{U_x}{W}$ and $\varepsilon_y = \frac{\sum_{j=1}^{n} U_{y,j}}{nL}$, in which n is the number of unit cells. The Poisson's ratio (ν) was calculated as $\nu = -\frac{\varepsilon_y}{\varepsilon_x}$.

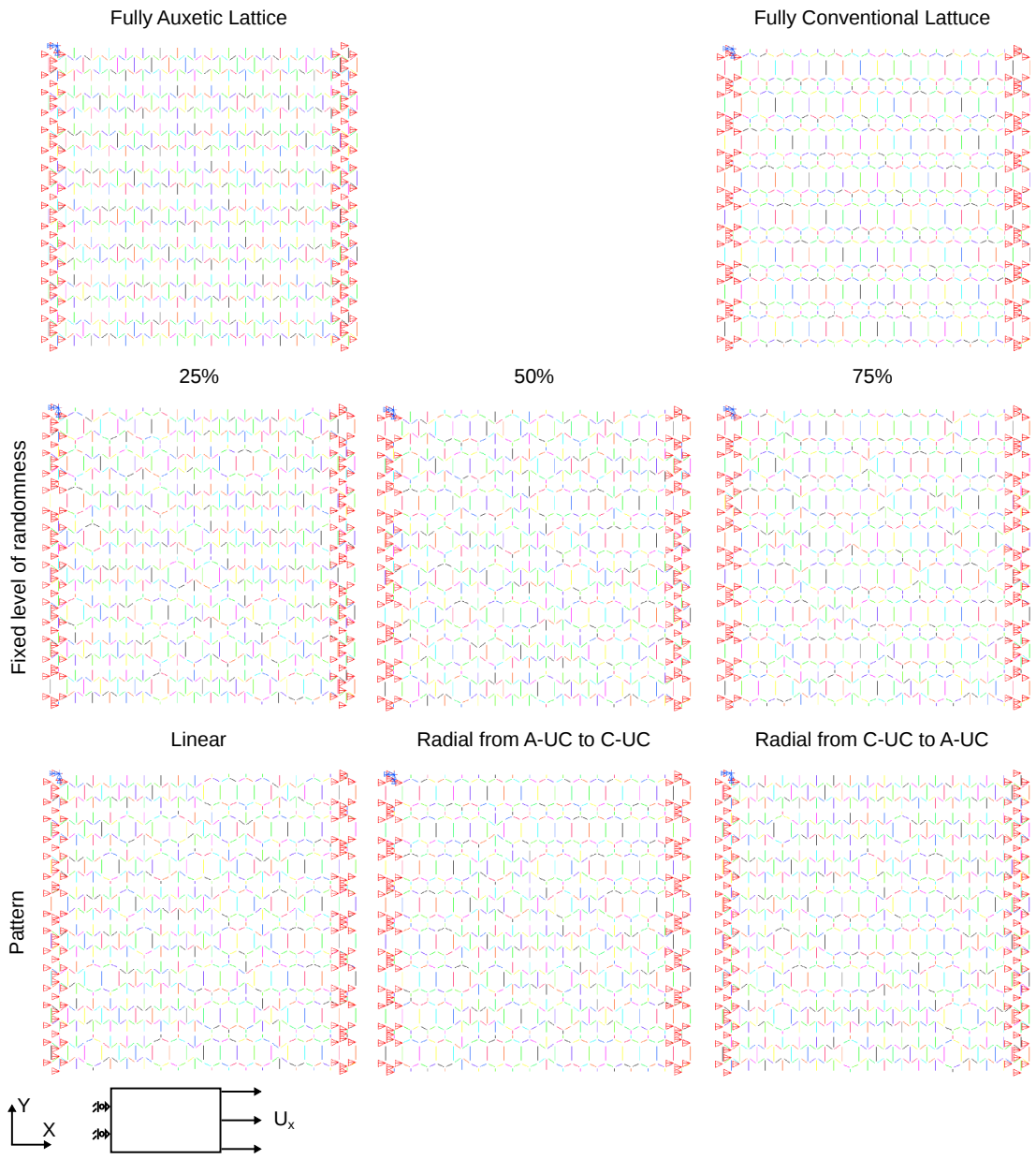

Figure 3.3: *Typical Finite Element models for different specimens.*

3.3 Results and Discussion

3.3.1 Validation of FE Results with Experimental Data

Numerical simulations for eight different samples were performed. In the case of randomness, one thousand simulations were carried out to make sure that the effects of randomness were eliminated.

In Figure 3.4, typical histograms obtained from numerical simulations for elastic stiffness and Poisson's ratio for samples with induced randomness were shown. Struc-

tures were randomly constructed and the random numbers come from a normal distribution. We checked the distribution of resulted values by plotting histograms. The histograms show a normal distribution for each parameter. Therefore, we use mean ± standard deviation for the representation of these values.

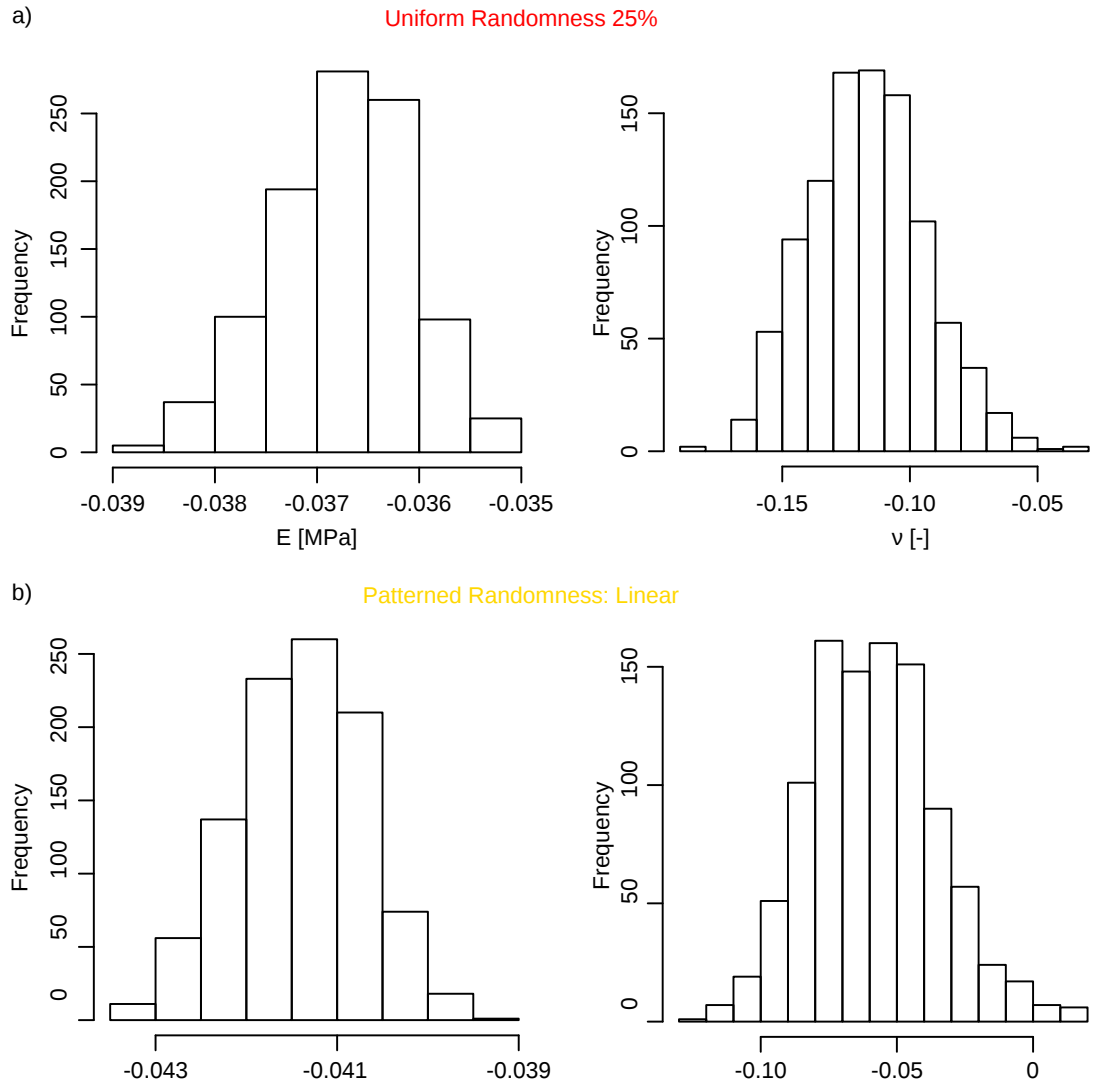

Figure 3.4: *Histogram of elastic stiffness and Poisson's ratio for two representative simulations with a) fixed level of randomness (25 %), and b) linear patterned randomness. The plots show a normal distribution for elastic stiffness and Poisson's ratio.*

For the validation of numerical simulations, we compare the elastic stiffness results with the one calculated from experiments. Comparison of FE and experimental results showed less than 6 % difference (Figure 3.5, Table 3.3). Those differences may have been caused by the micro-imperfections that arise from the bubbles formed in the ligaments of the lattice structures during the sample preparation process.

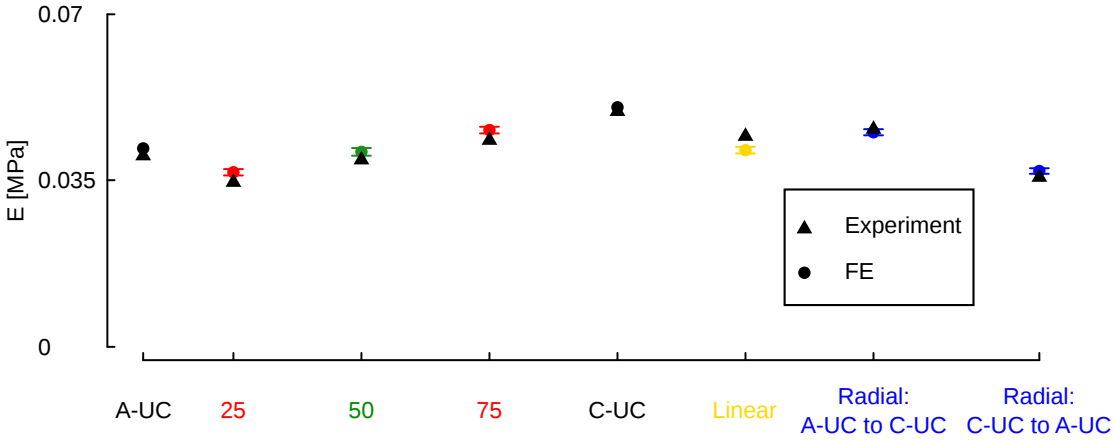

Figure 3.5: *Comparison of experimental results and numerical simulations. The mean ± standard deviation is shown for the numerical simulations.*

Table 3.3: *Elastic stiffness obtained from numerical simulation and experiments tests. Results for the FE simulation are presented as a mean ± standard deviation.*

Randomness distribution	$E\ [MPa]$		Error [%]
	Experiments	FE	
Uniform 0 % (A-UC)	0.040	0.042	5
Uniform 25 %	0.035	0.037 ± 0.00067	5.7
Uniform 50 %	0.039	0.041 ± 0.00080	5.1
Uniform 75 %	0.043	0.046 ± 0.00070	6.98
Uniform 100 % (C-UC)	0.050	0.050	0
Linear pattern	0.044	0.041 ± 0.00069	6.82
Radial pattern (A-UC to C-UC)	0.046	0.045 ± 0.00064	2.17
Radial pattern (C-UC to A-UC)	0.036	0.037 ± 0.00058	2.78

3.3.2 Implementation of Strategy of Randomness for Expansion of Data Range Using Numerical Modeling

Supplementary Angles for Auxetic and Conventional Unit Cells

The effects of topological design on the elastic modulus-Poisson's ratio duos were then explored using the computational models. First, the effects of the interior angle of each unit cells on the mechanical properties were studied by initially assuming that the angle of A-UC and C-UC are dependent and supplementary. Randomness was then introduced into the models in the ways described in Section 3.2.2, and Deformation in longitudinal (x) and lateral directions (y) obtained from FE results for two samples

were shown in Figure 3.6. Distributions of deformation in longitudinal direction show similar trend, while lateral deformation distributed differently for two selected geometries. Strains in lateral and longitudinal directions can be calculated as it is described in Section 3.2.4.

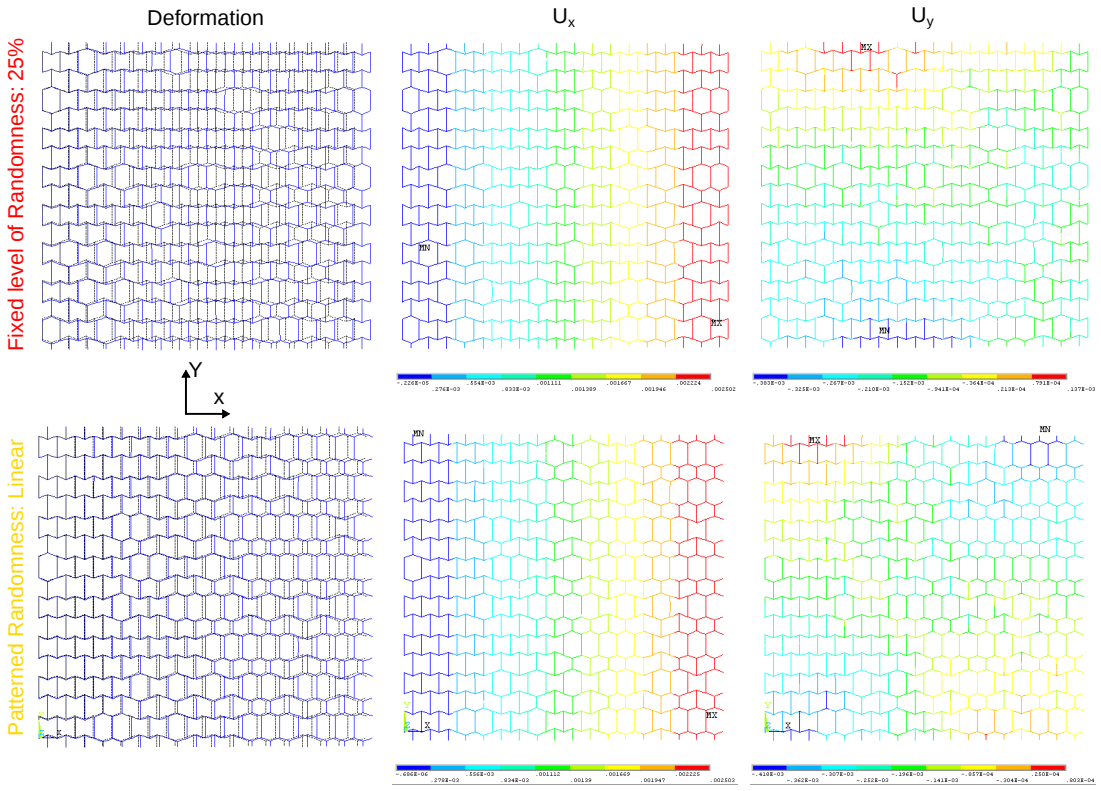

Figure 3.6: *Typical deformation and its distributions in lattice structures with top: 25 % uniform randomness, bottom: linear patterned randomness. The angles of A-UC and U-UC are supplementary ($\theta_{A-UC} = 80, \theta_{C-UC} = 120$). Due to the specific shapes of unit cells, deformation in longitudinal direction is similar in both lattice, but the lateral deformation varies. Similar strain distributions can be expected in x and y directions.*

The calculated duos of the mechanical properties were compared with those obtained for a lattice with uniform unit cells (solid circles in Figure 3.8). Randomness changed the Poisson's ratio in the lattice structure while the elastic modulus remained unchanged (Figure 3.8a,b left).

Independent Angles for Auxetic and Conventional Unit Cells

In the next step, we changed the topology of the unit cells independently from each other, i.e. the angles could be independent and not necessarily supplementary. Two examples for such cases are presented in Figure 3.7. The unit cells with the highest elastic moduli were combined with unit cells with the highest values of the Poisson's

ratio. As an example, auxetic unit cell with 60° angles (highest Poisson's ratio) were combined with the conventional unit cells with 90° angles (with highest elastic modulus) (Figure 3.7). Total deformation together with lateral and longitudinal distribution of deformation were also compared in this figure. Due to the geometrical features at micro-level and nature of A-UC and U-UC exposed to the loading condition, longitudinal deformations for both examples are similar, while lateral deformation/ strain will be different.

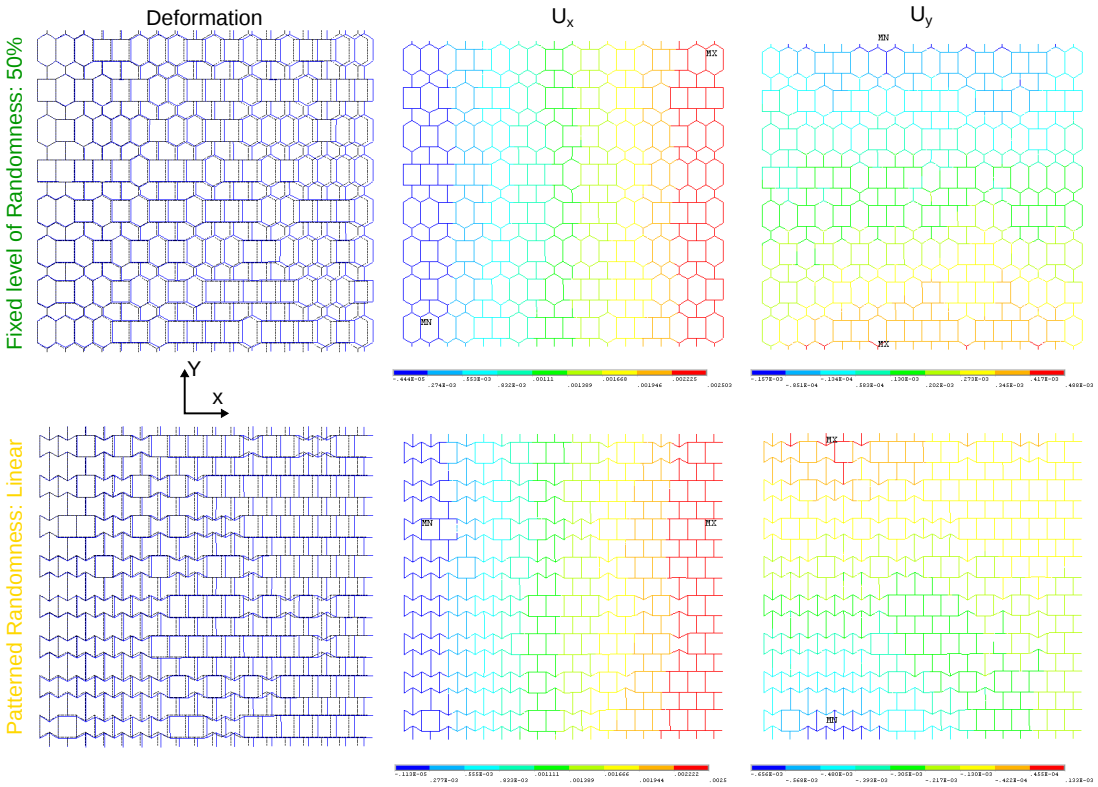

Figure 3.7: *Typical deformation and its distributions in lattice structures with top: 50 % uniform randomness ($\theta_{A-UC} = 90, \theta_{C-UC} = 110$), bottom: linear patterned randomness ($\theta_{A-UC} = 60, \theta_{C-UC} = 90$). The angles of A-UC and U-UC are independent in these cases. Due to the specific shapes of unit cells, deformation in longitudinal direction is similar in both lattice, but the lateral deformation varies between two models. Similar strain distributions can be expected in x and y directions.*

Such random combinations of the unit cells resulted in a broader area of the elastic modulus-Poisson's ratio plane being covered by the elastic properties of the proposed designs (Figure 3.8c,d left) as compared to the case where the angles of A-UC and C-UC were supplementary (Figure 3.8a,b left).

The normalized (normalized with respect to the elastic stiffness of the solid constituent (E_s)) elastic modulus of fully auxetic and fully conventional metamaterials

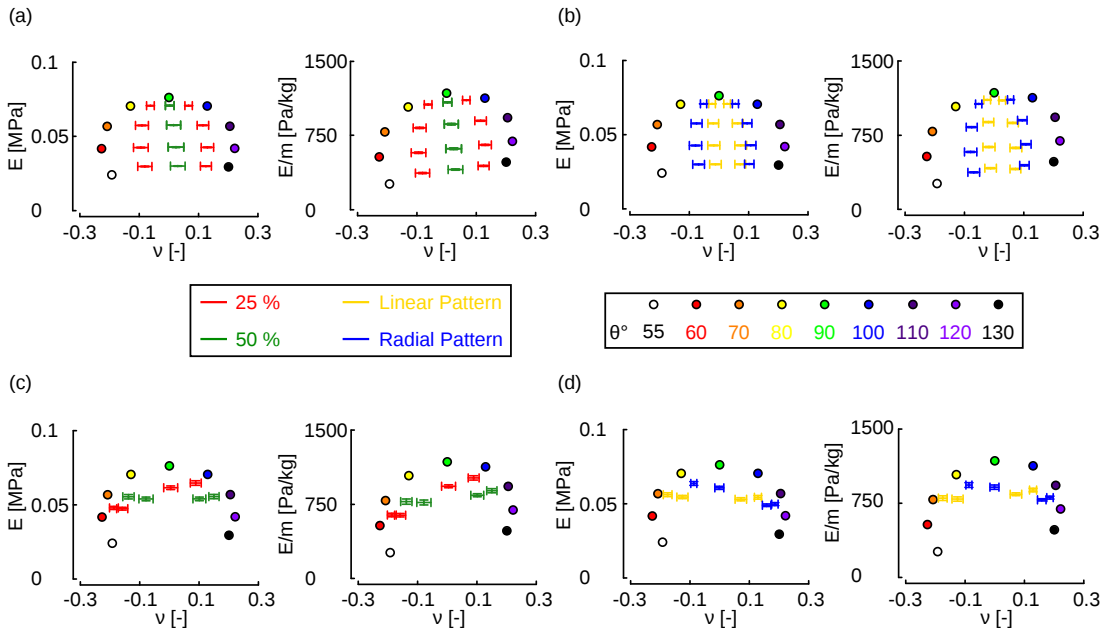

Figure 3.8: *Comparison of elastic modulus and Poisson's ratio planes obtained from FE simulations for lattice structures with regular (solid circles) and random microstructures. By variation of the angle θ, various geometries for the unit cells could be achieved. Different microstructural random generation was applied. (a, c) fixed level of randomness equal to 25 % and 50 %. (c, d) inducing randomness by a linear and radial pattern. In each part of this figure (a-d), the left graph shows the elastic modulus-Poisson's ratio plane while the right graph shows the specific elastic modulus-Poisson's ratio plane. A-UC and C-UC in lattice structures of (a-b) have supplement angles. The unit cells with the highest elastic moduli were combined with unit cells with the highest values of the Poisson's ratio (their angles were not necessarily supplementary) in the top row of the figure (a-b) to give the graphs in the second row of the figure (c-d).*

vary between 0.033 and 0.105 in our study. This is within the range (0.02-0.1) reported in [206] for conventional and hybrid metamaterials with comparable ligament thicknesses.

Since changing the topological design and introducing randomness in the structure could influence the relative density of the metamaterials, we normalized the predicted elastic moduli with respect to the mass of the cellular structure, thereby calculating the specific elastic modulus ($\frac{E}{m}$). The general trends remained the same after normalization of the elastic moduli with some relatively minor changes in the shape of the covered area (Figure 3.8a-d right). With or without normalization, the fully auxetic and conventional cellular structures created the boundaries of the covered area, while the values inside the area could be obtained by introducing patterned and uniform randomness into the topological design of the metamaterials (Figure 3.9).

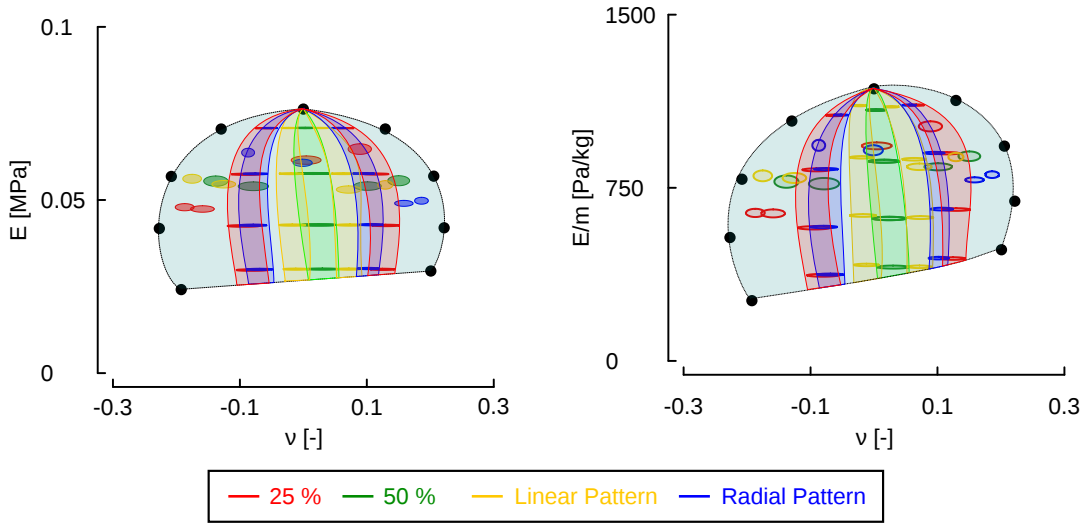

Figure 3.9: *Comparison of elastic stiffness (left) and specific elastic stiffness (right) with Poisson's ratio obtained from FE simulations for regular (solid circles) and random lattice structures. An envelope is drawn on data for lattice structure with regular unit cells. Results of different methods for the generation of random microstructures are spread as in this envelope.*

3.4 Conclusion

The ability to independently tailor the elastic modulus and Poisson's ratio and cover a broad area of the associated plane of the elastic properties (Figure 3.9) has many practical applications such as in the design process of biomedical implants and scaffolds. Furthermore, this possibility could be used in the design of structurally applied auxetic metamaterials whose functionality is driven by their (low) Poisson's ratio but are simultaneously required to exhibit high stiffness values to ensure sufficient load bearing capacity.

It could also serve as a general platform for the rational design of (soft) mechanical metamaterials. From the mechanistic viewpoint, patterned randomness and the interplay between the unit cells with positive and negative Poisson's ratio may be interpreted in analogy with the roles played by dislocations and precipitates in polycrystalline metallic materials. Random positioning of different types of the unit cell has the tendency to change stress flow, thereby resulting in the blockage or faster propagation of the far-field deformations. Those modifications in the deformation paths may be respectively manifested at the larger scales as increased or decreased stiffness, while not necessarily influencing the lateral deformation and, thus, the Poisson's ratio. Additional patterns of randomness and more diverse topological designs of the unit cells are expected to broaden the range of accessible properties even further.

In summary, we proposed patterned randomness in the positioning of auxetic and conventional unit cells as a strategy for independently tailoring the elastic modulus and Poisson's ratio of soft mechanical metamaterials made with indirect additive manufacturing. While metamaterials with homogenous and uniform arrangement of unit cells create the boundaries of the area covered in the elastic modulus-Poisson's ratio plane, the designs incorporating patterned randomness fill the enclosed area. Patterned randomness could, therefore, serve as an additional tool in the rational design of mechanical metamaterials.

CHAPTER 4

Shape Prediction with Soft Mechanical Metamaterials Under Mechanical Stimuli

From the manuscript accepted for the publication in [1]

4.1 Introduction

Mechanical metamaterials are materials whose macro-scale properties such as unusual deformation characteristics directly originate from their (small-scale) topological design [45, 68, 193, 207]. Rational topological design of metamaterials could lead to properties and functionalities not usually offered by natural materials such as negative Poisson's ratio (auxetics) [63, 67, 208], negative compressibility [45], elastic hysteresis [209], independent tailoring of elastic properties [210], snapping deformations [70], and shape-changing with vibration-mitigation capability [211] and out-of-plane deformation through 3D design of architectured metamaterials [212].

Metamaterials have also potential applications in shape-changing materials that are kinematically inspired by kirigami/origami-based designs [213], fractal cuts [214], deployable morphing [215], pattern switching [216], or strain amplification elements

[1] M. J. Mirzaali, S. Janbaz, M. Strano, L. Vergani, A. A. Zadpoor, Shape-matching soft mechanical metamaterials, *Scientific Reports*, doi:10.1038/s41598-018-19381-3

working through auxetic unit cells [217]. A novel objective in the design of shape-changing metamaterials is achieving a pre-defined shape upon loading through what we here call "shape-matching" materials.

Shape-matching metamaterials have a myriad of potential applications most notably in soft robotics [218, 219] and wearable (medical) devices. For example, shape-matching metamaterials could be used to design soft grippers that grip delicate objects with the maximum surface contact and, thus, minimum contact force. Wearable (medical) devices such as exosuits [220], prosthetics and orthotics [221], and tunable mechanical memory [222] are the other potential areas of application. Finally, the fashion design industry [223] may also be able to benefit from shape-matching or form-fitting materials.

4.2 Materials and Method

4.2.1 Sample Preparations and Geometrical Features of Prototypes

Here, we demonstrate soft shape-matching metamaterials that are designed by rationally combining auxetic, conventional, and transitional unit cells into a cellular solid, and are indirectly additively manufactured from elastomers (Figure 4.1). We used an equal aspect ratio for the longitudinal and transversal dimensions of all unit cells for easier integration of the unit cells with different reference angles in a planar cellular structure. This enables us to combine auxetic and conventional unit cells in the longitudinal direction, which could be also replicated in the transverse direction. Arrangement of unit cells with different values of the Poisson's ratio could then be used to program the lateral deformation of the cellular material upon deformation. The inverse problem of rationally designing a shape-matching metamaterial then reduces to the problem of finding the combinations of the Poisson's ratios that give rise to the desired lateral deformation and mapping those values of the Poisson's ratios back to unit cell designs.

To design the first prototypes, we divided the length of the specimen into three regions, i.e. auxetic, transitional, and conventional (Figure 4.1a). When designing the cellular structures, we assumed that the parameters c and w (Figure 4.1a) are constant for both auxetic and conventional unit cells ($\frac{c}{w} = 3$). The interior angle of each unit cell could therefore change the geometry of the unit cell from auxetic ($48^\circ < \theta < 90^\circ$) to conventional ($90^\circ < \theta < 120^\circ$). In the transitional region, the angle of each unit cell linearly changed from the auxetic angle to conventional one. We fabricated four prototypes with different unit cells in each of those three regions. The total numbers of unit cells in the longitudinal direction, $m = 18$, was similar for all specimens. The total length of each specimen was therefore $L = c \times m$. The number of unit cells

in the transverse direction, n, was also fixed ($n = 7$). The width of each specimen was therefore $W = 2n \times w$. The design parameters for all specimens are presented in Table 4.1.

Table 4.1: *The parameters of the prototypes fabricated with indirect additive manufacturing.*

parameters	$c\,[mm]$	$w\,[mm]$	$n\,[-]$	$m\,[-]$	$L\,[mm]$	$W\,[mm]$	$t_{lattice}\,[mm]$	$t_{ligament}[mm]$
	15	5	7	18	270	70	7	0.7

We used indirect additive manufacturing to fabricate the specimens. A mold was designed and additively manufactured using a fused deposition modeling (FDM) 3D printer (Ultimaker 2+, Geldermalsen, The Netherlands) from polylactic acid (PLA) filaments (MakerPoint PLA 750 gr Natural) (Figure 4.2a). Subsequently, an elastomeric polymer (Elite Double 8, Zhermack, Badia Polesine, Italy) with a one-to-one ratio of the base to catalyst was poured into the mold. Once the specimens had cured, i.e. after ≈ 1 hour, the mold was removed. The final shapes of all specimens are presented in Figures 4.1b and 4.2.

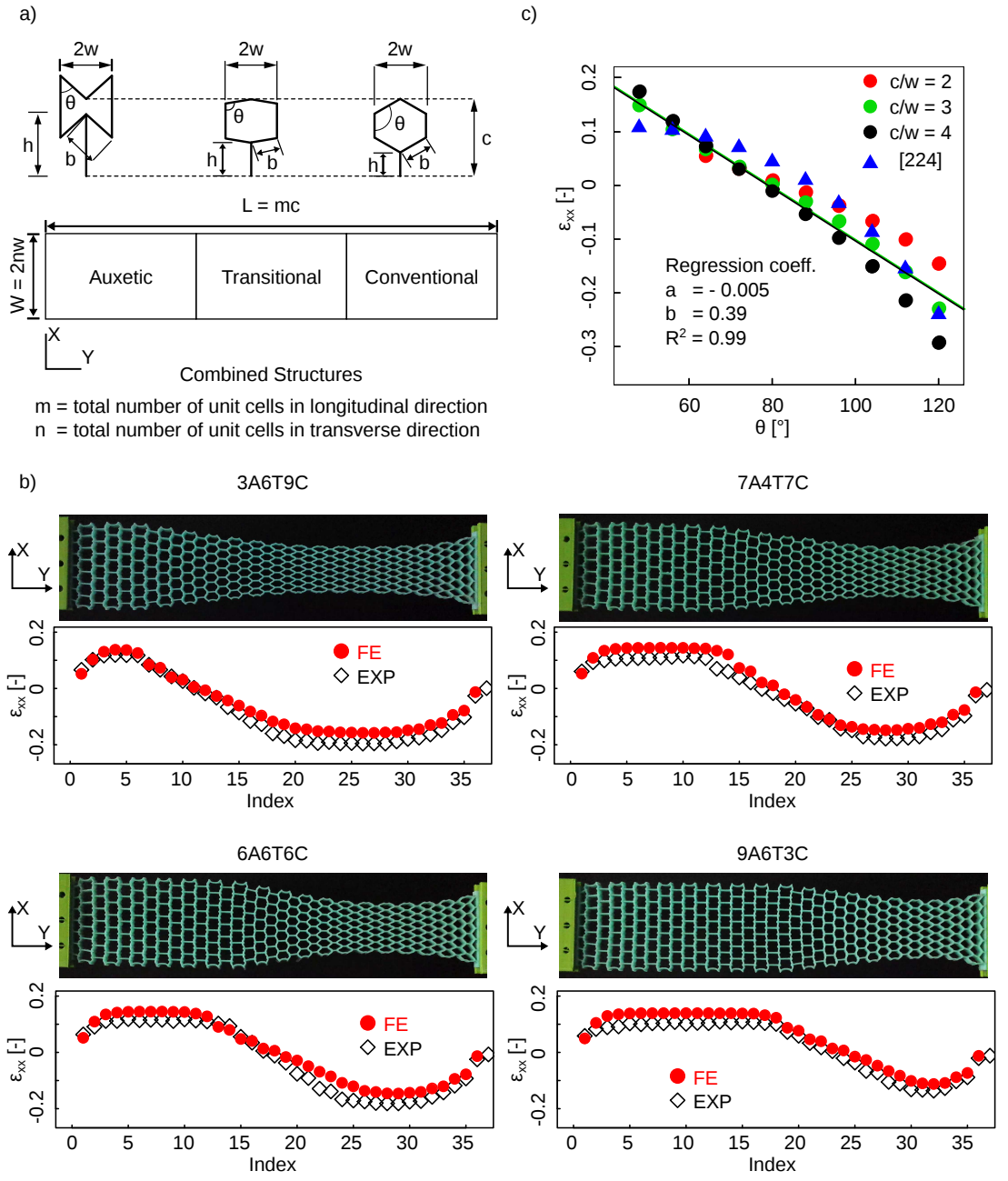

Figure 4.1: *a) A schematic drawing of the auxetic and conventional unit cells. The angle, θ, varies between 48° and 120°b) Four specimens with three zones (auxetic, transition and conventional) were fabricated. Computational models were developed for each specimen and the simulation results were compared against experimental observations. The specimen naming convention follows the NoANoTNoC format where "No" shows the number of unit cells in each region, while A, T, and, C stand for the number of unit cells in the auxetic, transitional, and conventional regions. In the transitional region, unit cells were linearly changed from auxetic to conventional unit cells. In all experimental specimens, $\frac{c}{w} = 3$. Index refers to the points at the corner of each unit cell where the lateral strains were calculated. c) The strains of cellular structures calculated for different $\frac{c}{w}$ ratios and reference angles (longitudinal strain = 20 %). Numerical results were also compared with the analytical relation (Equation 4.2) in the literature [224] for the calculation of lateral strains.*

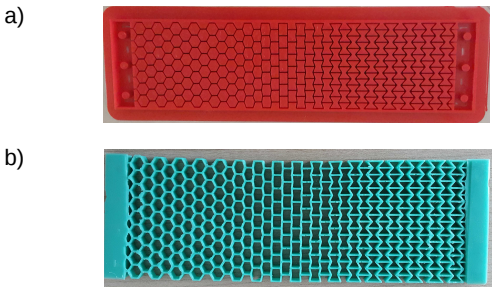

Figure 4.2: *Indirect additive manufacturing was used for the manufacturing of the prototypes. For this goal, first a mold was additively manufactured (a). Then, elastomeric polymers were poured into the mold. After being cured, the final specimen was extracted by breaking the mold (b).*

4.2.2 Experimental Testing

The specimens were deformed under displacement-controlled tensile loading applied by a mechanical test bench (LLOYD instruments, LR5K, load cell=100 N, displacement rate = $50\ \frac{mm}{min}$). Time, force, and displacement were recorded at a sampling rate of $20\ Hz$. Simultaneously, the deformation was captured by a digital camera. After the test, the first and last frames of each video was selected and converted into binary images. The middle junctions in each unit cell at the left and right sides of the structure were highlighted by points in the images. Then, the highlighted regions were dilated to one pixel. The initial width of each unit cell, W_j, was calculated from the first image as: $W_j = X_{(j,right)} - X_{(j,left)}$, where $j = 1 : 36$ shows the number of points in the total length of the structure, also called as index, and X_j stands for the position of each point measured in terms of pixels. Every two points belong to one unit cell. Similarly, after deformation, the final width of each unit cell, $W_j^{'}$, was calculated as $W_j^{'} = X_{(j,right)}^{'} - X_{(j,left)}^{'}$. Finally, the lateral strain was defined as $\varepsilon_{(j,xx)} = \frac{W_j^{'}}{W_j}$.

4.2.3 Computational Modeling

Computational models of the metamaterials were created with ABAQUS, 6.14. A hyperplasic Neo-Hookean material model ($C_{10} = 0.106$ MPa and $D_1 = 0.03\ \frac{1}{MPa}$) and plane-stress elements (CPS8) were used in the models. The material coefficients were determined using the standard experimental protocols for testing elastomeric materials in tension (ASTM D412 Type C) and compression (ASTM D 575-91). The out-of-plane thickness, $t_{lattice}$, of the structure and the thickness of each ligament, $t_{ligament}$ were respectively set to 10 mm and 1 mm. Two reference points were defined at the top and bottom of the model and were tied to two nodes from the corresponding locations. The bottom reference point was fixed while the top reference point was displaced far enough to create 20 % longitudinal strain. An implicit nonlinear solver (Abaqus Standard) was used for the simulations. The lateral strain calculated for the computational models were evaluated in a way similar to those of the experiments. Several node sets were defined at the internal hinges of the unit cells located at the left and right sides of the structure. The mean lateral displacements $U_{(j,left)}$, $U_{(j,right)}$ were calculated for each node set. The lateral strain was then obtained as: $\varepsilon_{(j,xx)} = \frac{U_{(j,right)} - U_{(j,left)}}{W}$.

4.3 Results and Discussion

4.3.1 Change of Lateral Strains on Uniform Lattice Structures

For the first analysis, we created unit cells with pure auxetic and conventional lattice structure. These specimens were experimentally tested (Figure 4.3). We found out that auxetic unit cells reached the saturation levels of strains earlier than conventional unit cells. The maximum level of lateral strain that could be reached with fully conventional structures is lower than the combined structures. This information is essential for proper design of samples that combine auxetic and conventional unit cells.

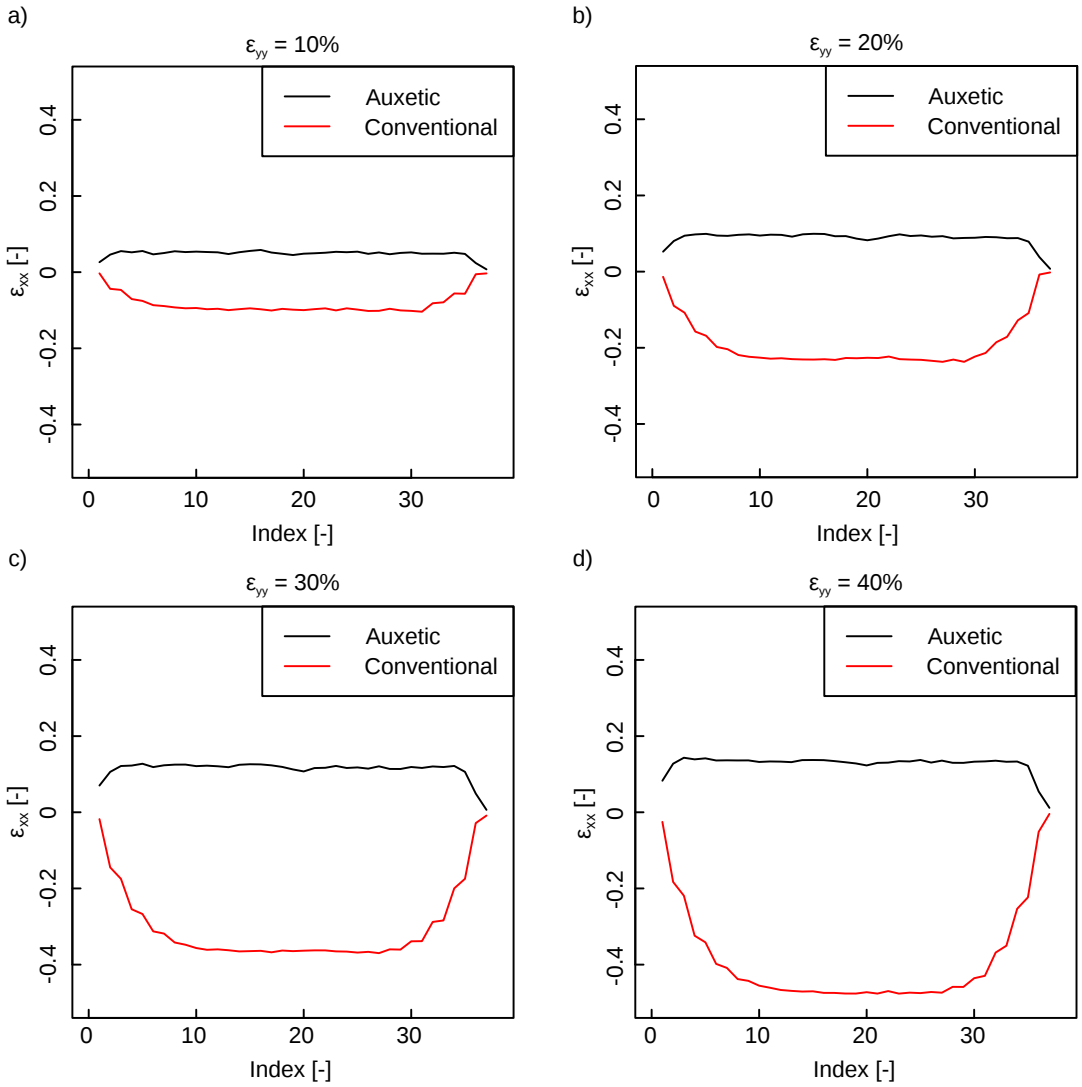

Figure 4.3: *Lateral strain at four different longitudinal strains for pure auxetic and pure conventional lattice structures. The angle of auxetic and conventional structures were 48 and 120, respectively.*

4.3.2 Effects of Transverse Number of Unit Cells on the Lateral Strain

We also performed experiments to evaluate the effects of the number of unit cells in the transverse direction of the structure on the lateral deformation. We found that the number of the unit cells in the transverse direction only influences the amplitude of the deformations but not the lateral strains of the structure 4.4.

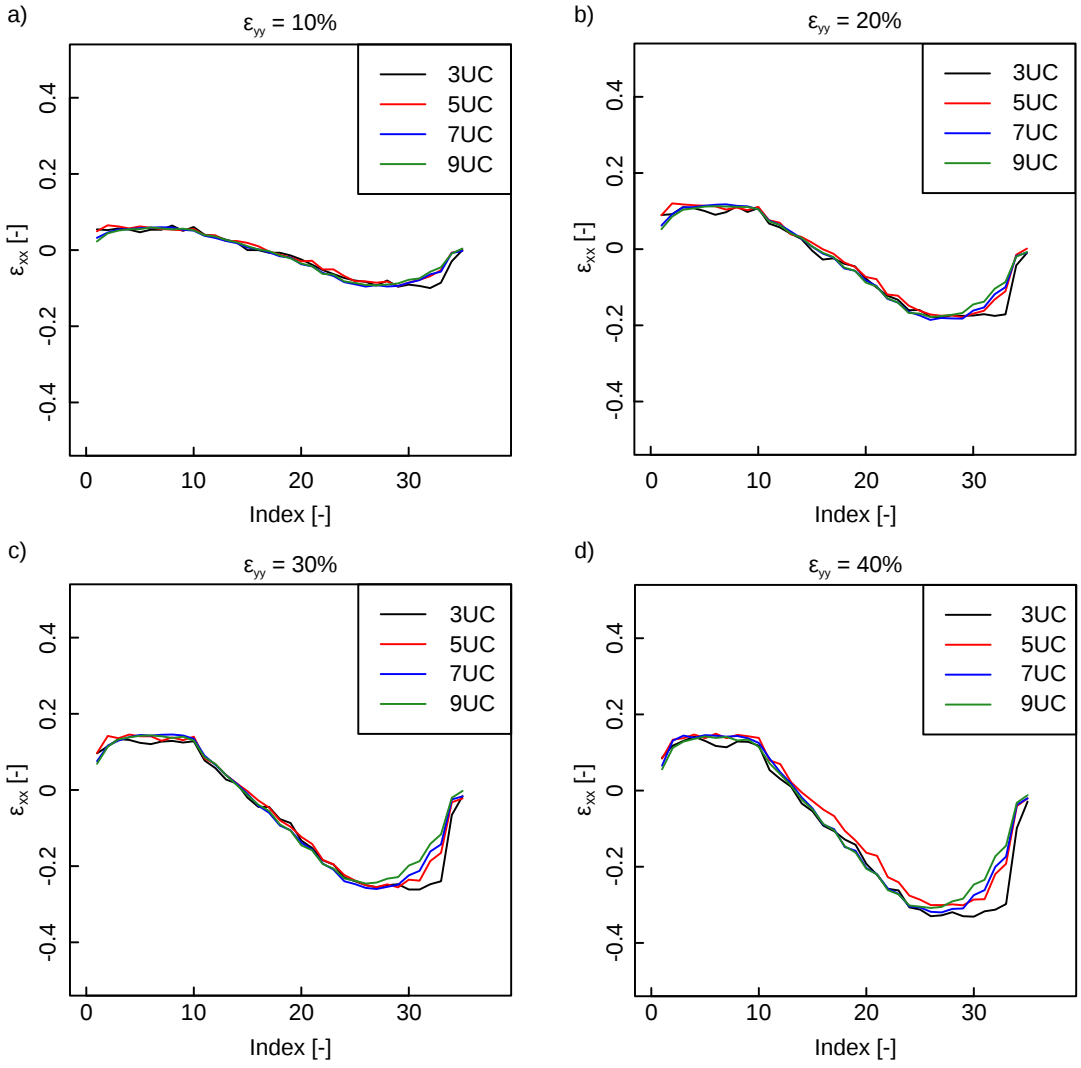

Figure 4.4: *The effects of the number of unit cells in the transverse direction of combined structure on the lateral strains. Results are plotted at four extension levels (a-d). Equal number of conventional, auxetic and transitional unit cells were considered for the construction of these specimens.*

4.3.3 Experimental Results of Combined Lattice Structures

Considering the experimental results for the combined structures, it was observed that changing the regions (auxetic, transition, conventional) in the structure does not influ-

ence the maximum lateral strains in the auxetic unit cells (if we compare those results with the lateral strain we obtained for pure auxetic and conventional lattices in Section 4.3.1). However, due to the geometrical features of the conventional unit cells, they were more sensitive to the boundary conditions and deformation of the adjacent unit cells. In the transitional region, we found that lateral strain linearly changes along the length (Figures 4.5 and 4.6).

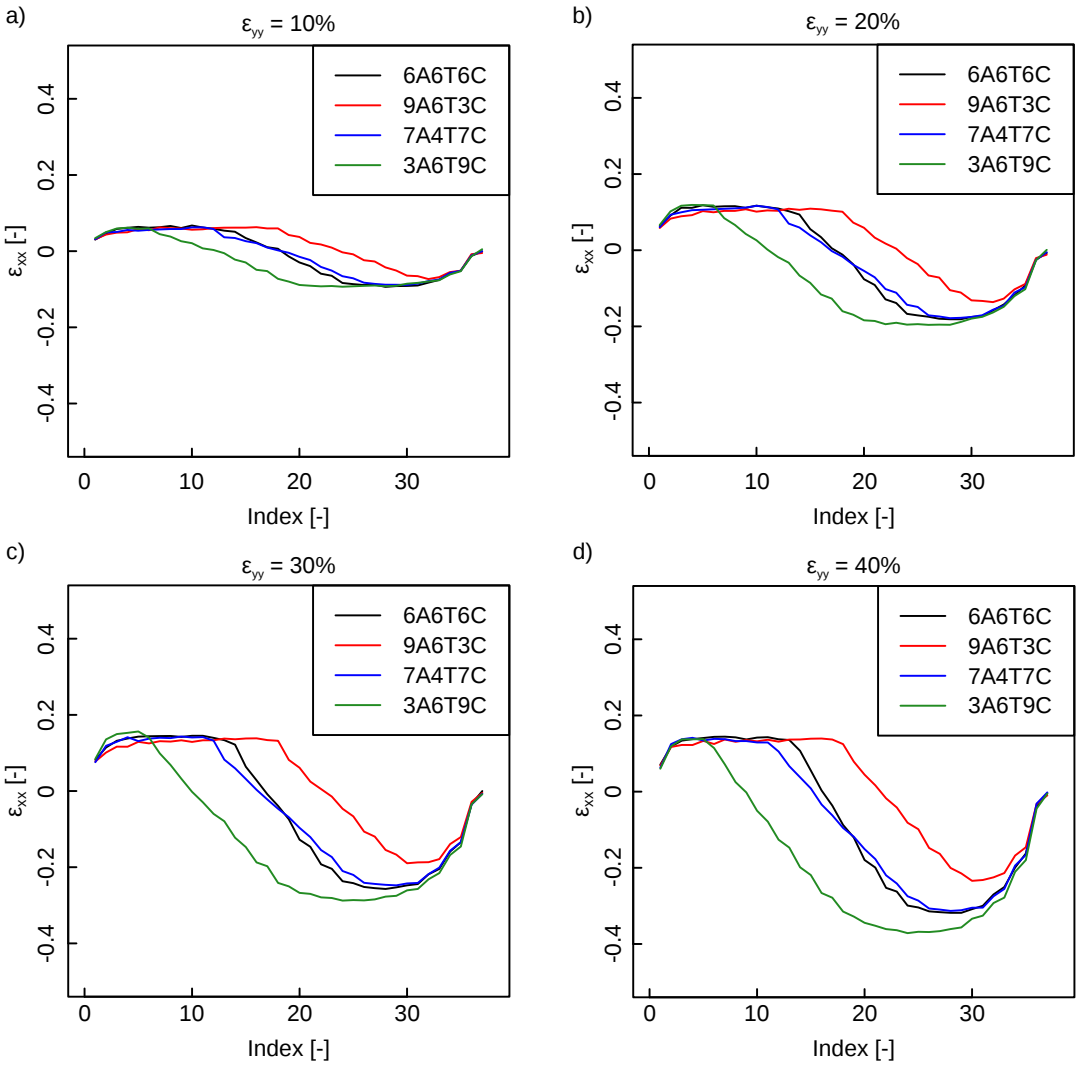

Figure 4.5: *Comparison of lateral strains at different levels of longitudinal expansion for four combined specimens. The specimen naming convention follows the NoANoTNoC format where "No" shows the number of unit cells in each region, while A, T, and, C stand for the number of unit cells in the auxetic, transitional, and conventional regions. In the transitional region, unit cells were linearly changed from auxetic to conventional unit cells. In all experimental specimens,* $\frac{c}{w} = 3$.

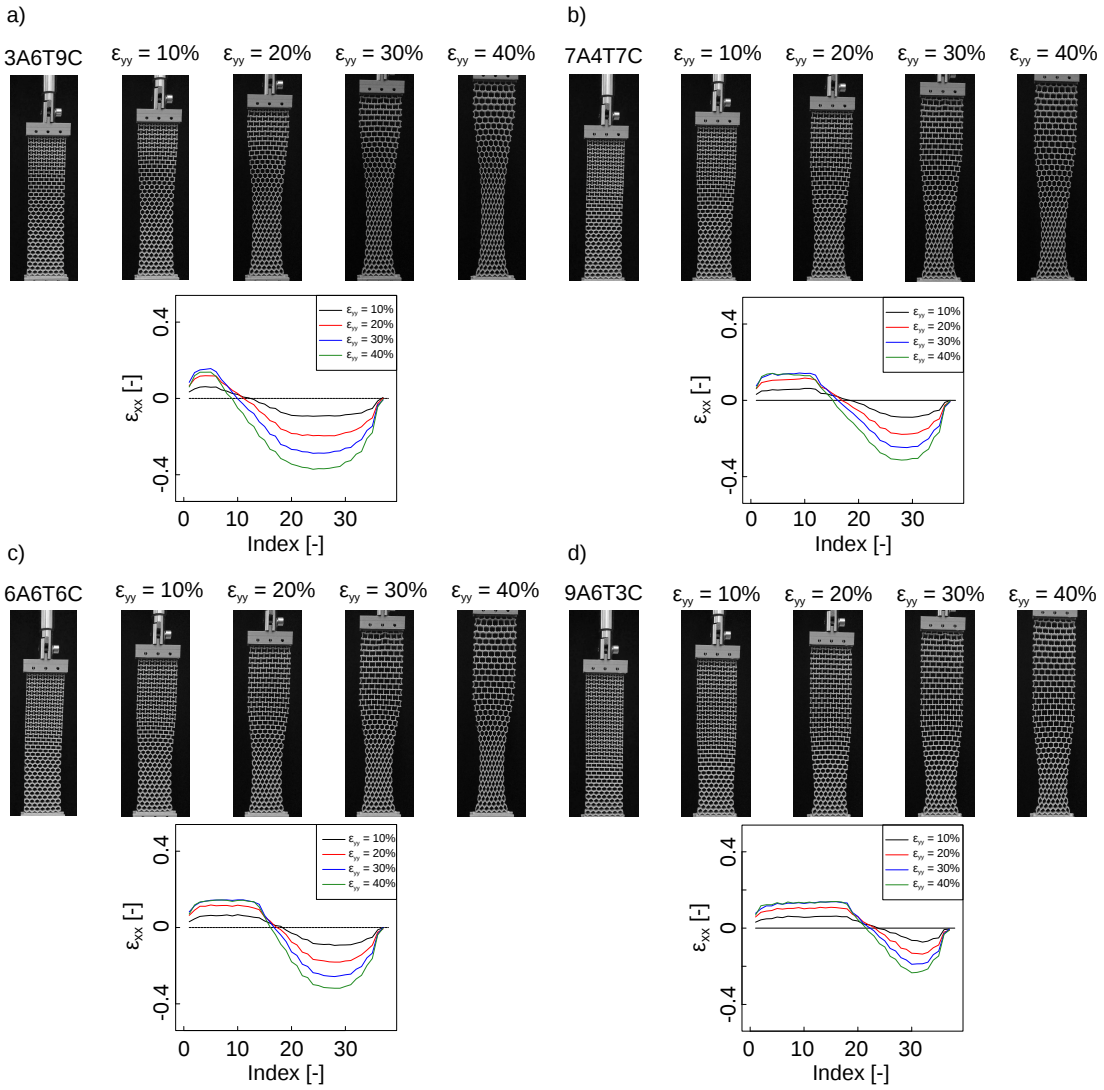

Figure 4.6: *Individual lateral strains at different levels of longitudinal expansions for four combined specimens. a) 3A6T9C, b) 7A4T7C, c) 6A6T6C, d) 9A6T3C. The specimen naming convention follows the NoANoTNoC format where "No" shows the number of unit cells in each region, while A, T, and, C stand for the number of unit cells in the auxetic, transitional, and conventional regions. In the transitional region, unit cells were linearly changed from auxetic to conventional unit cells. In all experimental specimens,* $\frac{c}{w} = 3$.

4.3.4 Comparison of Finite Element and Experimental Results

The lateral strains obtained computationally were found to be in good agreement with experimental observations (Figure 4.1b). Having evaluated the accuracy of the computational models, we expanded them to include other $\frac{c}{w}$ ratios, i.e. 2 and 4, for fully auxetic and conventional lattice structures (Figure 4.1c). In those simulations, the total number of unit cells in the structure was kept the same to enable comparison with

previous results and the lateral strain was calculated at the middle of the cellular structure. Our calculations showed changing this ratio does not drastically change the lateral strains especially for the auxetic unit cells (Figure 4.1c). Therefore, we continued to use $\frac{c}{w} = 3$ as a reference ratio in the following designs. Furthermore, the computational results showed an almost linear relationship between the lateral strains and the angle of the unit cells (Figure 4.1c). This linear relation was used as the basis of our designs in the next steps, where the applied longitudinal strain was fixed at 20 %:

$$\varepsilon = -0.005\theta + 0.39. \tag{4.1}$$

We compared our numerical simulations with the analytical relation found in the literature [224]. Lateral strain in the conventional and the re-entrant honeycombs can be calculated as:

$$\varepsilon_x = -\frac{\delta \sin(\theta)}{b \cos(\theta)}. \tag{4.2}$$

where, b and θ are the geometrical parameters of each unit cell (Figure 4.1a) and $\delta = \frac{0.2}{\cos(\theta)(c-h)}$ as we fixed the applied longitudinal strain at 20 %. The geometrical parameters, i.e. b,θ, c and h, were considered separately for individual unit cells and the final lateral strains were compared with the numerical simulations. This comparison shows a good agreement between the numerical and analytical results (Figure 4.1c).

Prediction of Arbitrarily-Defined Strain (Deformation) Functions

Having verified our computational models against experiments for a number of designs, we developed a rational design platform based on the results of the computational models to achieve lateral deformations that match the countour of an arbitrarily-shaped object. If the contour of the lateral deformation is discretized into a finite number of sub-regions, auxetic and conventional unit cells could be used to create the desired lateral deformation using Equation 4.1. The superposition of the deformations of all unit cells was hypothesized to create the target shape. To assess the validity of that hypothesis, we created a number of arbitrarily-defined strain functions (Y1-Y9) using a three-terms Fourier's-like series:

$$Y = a_1 sin(\alpha\omega(x-1)) + a_2 sin(2\alpha\omega(x-1)) + a_3 sin(3\alpha\omega(x-1)) \tag{4.3}$$

where the parameters $\omega = 0.37$ and a_1,a_2,a_3,α (Table 4.2) were parametrically selected in order to achieve substantially different mode of deformations and covering a wide range of deformed shapes (Figure 4.7). x is the index of each unit cells in the

longitudinal direction and changes between 1 and 18 (the total number of unit cells in the longitudinal direction of the cellular structure). Using Equation 4.1, we selected the angles of the auxetic and conventional unit cells such that their predicted deformation would follow the strain functions generated by Equation 4.3 using the above-mentioned coefficients (Figure 4.7). We then created computational models to determine the actual deformation of the cellular structures that were designed using the predictions of Equation 4.1. Comparison between the actual deformations and the target strain functions showed that the cellular structures designed using Equation 4.1 could closely follow the target shape in all considered cases (Figure 4.7).

Table 4.2: *The random parameters used in the definition of the functions (Y1-Y9).*

Functions	a_1	a_2	a_3	α
Y1	0.15	0	0	0.5
Y2	0	0.15	0	0.5
Y3	0	0	0.15	0.5
Y4	0.068	0.068	0.068	0.5
Y5	0.15	0	0.075	0.5
Y6	0.075	-0.09	0.045	0.5
Y7	0.068	0.068	0.068	1
Y8	0.105	-0.053	-0.053	1
Y9	0.15	0	0.075	1

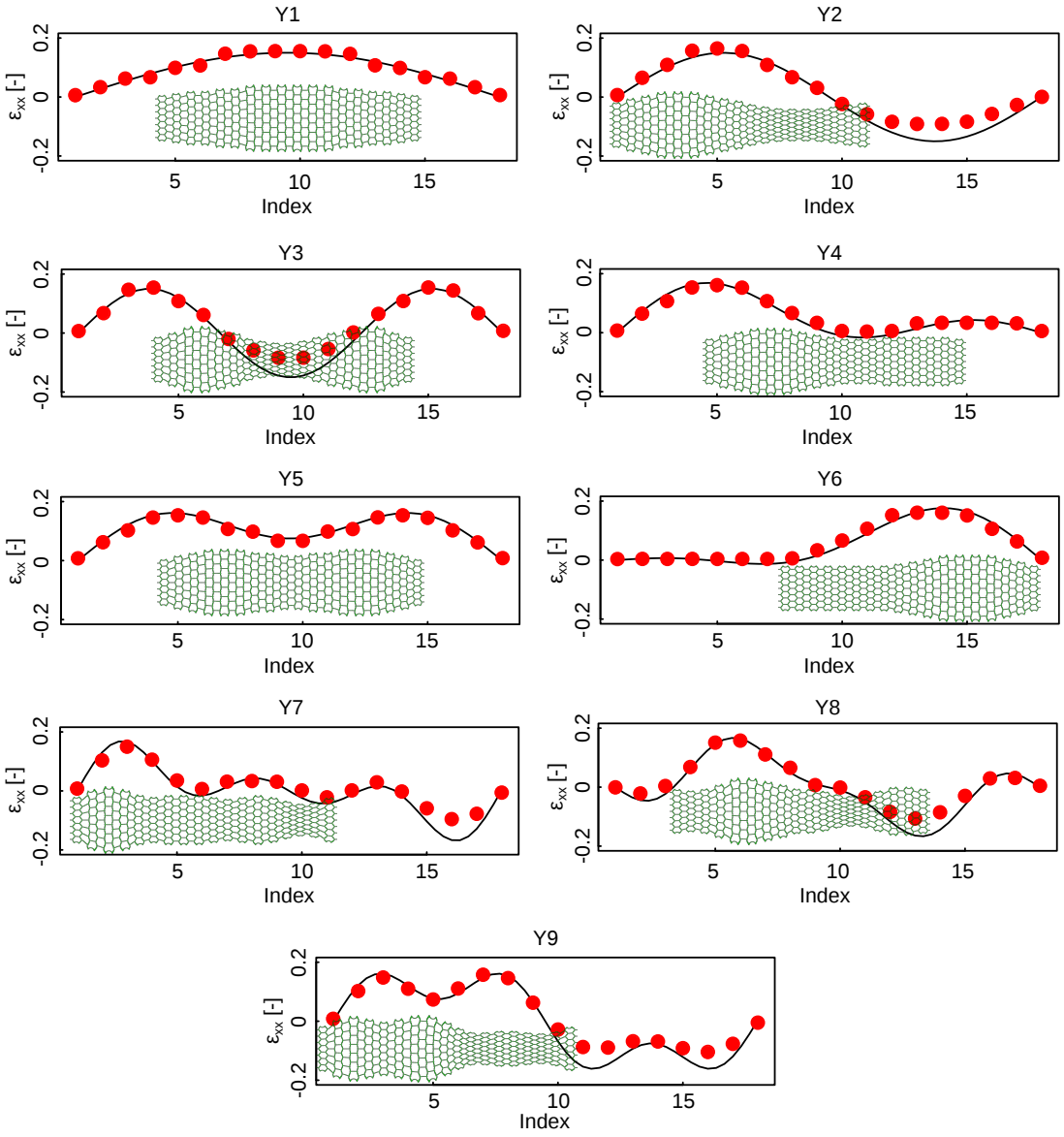

Figure 4.7: *The structures were designed in a way to fit the arbitrary functions (Y1-Y9). The parameters of the functions are listed in Table 4.2. The longitudinal strain for each case is equal to 20 % of the total length. The actual deformations determined using direct numerical simulations are also shown (scaling factor = 3). Index refers to the middle point of each unit cell where the lateral strain is calculated.*

Prediction of Boundaries of Real Objects

In the last step, we aimed to design cellular structures that would match the shapes of three real objects including an anatomical model of the scapula (Sawbones, Vashon Island, USA), a pumpkin, and a piece of Delft Blue pottery (a vase) (Figure 4.8). All objects were photographed from the top view, which were then used to describe the contours of the objects. The resulting contours then served as the target shapes for the design of the cellular structures. We selected the reference angles of the auxetic and conventional unit cells such that, according to Equation 4.1, their lateral deformations match the captured contours as closely as possible. The total number of unit cells in the transverse and longitudinal directions are therefore the only parameters that could be freely chosen with more unit cells along the length of the structure resulting in smoother approximations of the target curve. To use Equation 4.1, the design of the cellular structure needs to satisfy $\frac{c}{w} = 3$, which could be achieved by isotropic scaling of the entire structure. Assuming that we require a 20 % deformation of the metamaterial to match the shape of the objects, the length of the cellular structures could be determined using a deformation ratio of 1.2. Given the total length of the specimen and the parameter c, the maximum number of unit cells along the length of the structure, m, was calculated. Having assumed the number of unit cells in the transverse direction, n+1, the lateral strain could be calculated, which must be in the range of the minimum and maximum strains that fully auxetic and conventional structures could achieve. Finally, the reference angles of the unit cells were selected using Equation 4.1. A flowchart in Figure 4.8d shows the different design steps.

The cellular structures designed to match the shapes of the selected objects achieved good approximations of their target contours (Figure 4.8a-c). The shapes of the objects used here were selected based on the potential applications of shape-matching metamaterials. Moreover, each object represented different types of shape variations. For instance, the contour of the pumpkin requires the highest deformation amplitude. To achieve such high amplitudes, it is necessary to define more unit cells in the lateral direction of the structure (Figure 4.8b). The vase, on the other hand, has the smallest length among three objects. Therefore, application of a scaling factor is required when designing the shape-matching metamaterial (Figure 4.8c).

The fact that a simple equation such as Equation 4.1 and the superposition principle are very effective in designing soft metamaterials (whose deformation is nonlinear in nature) is quite remarkable and enables fast design of shape-matching metamaterials without the need for (nonlinear) optimization algorithms. The presented technique could be expanded for the prediction of the deformations at lower (i.e. micro-) scales. While we used here mechanical loading to deform the specimens, shape-matching

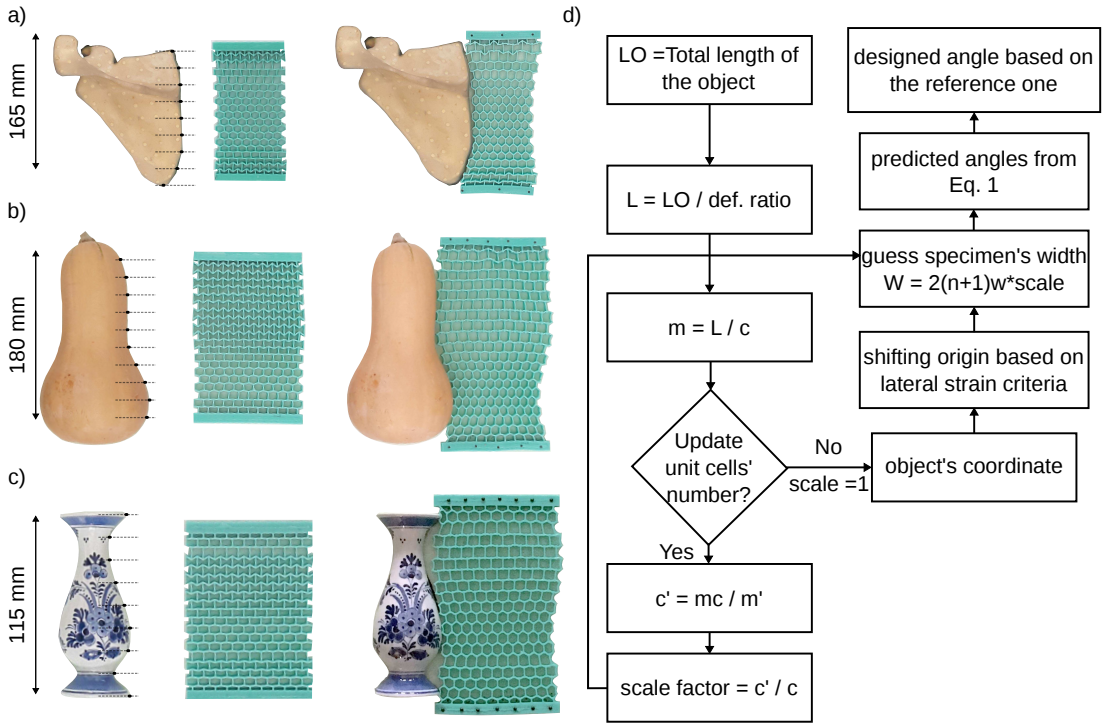

Figure 4.8: *Matching the shapes of three real objects including an anatomical model of the scapula (a), a pumpkin (b), and a Delft Blue pottery piece (a vase) (c). d) The flowchart of the design procedure.*

could be also activated using magnetic, thermal, or electrical stimuli. Shape memory polymers are the other candidates for such designs [225–228].

There are some limitations in the presented approach that are dictated by the maximum strains that could be achieved by conventional and auxetic unit cell. In general, auxetic unit cells tend to deform faster than the conventional ones and reach a level of saturation and robustness at higher longitudinal strains. This affects the connection between conventional and auxetic unit cells and prevents the conventional unit cells from complete deformation (see Figure 4.5 and 4.6). For this reason, we fixed the level of axial strain to 20 % so that we will ensure different unit cells can reach their maximum expansion without being affected by the adjacent unit cells.

The next steps would entail extending the presented technique to the case of three-dimensional shapes such as the shapes described by the surface of human body. One way of creating 3D structure is rolling the proposed 2D lattice structures to create tube-like structures. The shape-matching behavior of such axisymmetric structures is expected to be similar to those of 2D structures. For arbitrary 3D shapes, similar discretization method on surfaces rather than lines can be applied, although the complexity of the problem will increase due to the unknown interaction of individual unit cells. Direct 3D printing with similar elastomeric polymers could be used for the production of

such 3D structures.

In summary, we presented a design platform for the rational design of shape-matching soft mechanical metamaterials that combine functionally graded auxetic and conventional unit cells. The platform is shown to be able to match the arbitrary shapes created by three-term Fourier's series as well as the shape of real objects. Shape-matching materials have potential applications in soft robotics, wearable (medical) devices, and fashion industry.

CHAPTER 5

Crumpling of Porous Sheets

From the manuscript published as[1]

5.1 Introduction

Crumpling and folding of thin-wall objects are frequently encountered in nature, technology, and everyday life. Examples are morphogenesis of brain cortex [229], flower buds [230], and crumpled graphene [231]. The physics of crumpling has recently received increasing attention [232]. In particular, several studies have tried to reveal the relationship between the topological features induced during the crumpling process and the level of compaction and the associated forces [232–237]. The high strength and energy absorbance capabilities of crumpled structures have been studied as well [236, 238].

Crumpling could repeat itself under confined and controlled conditions. Understanding the physics of crumpling in such controlled experiments could be helpful for designing crumpling-based metamaterials, where crumpled structures act as the building blocks. Crumpling a thin sheet create a low weight structure with significant stiffness and robust mechanical response against disorder and noise which are abun-

[1] M. J. Mirzaali, M. Habibi, S. Janbaz, L. Vergani, A. A. Zadpoor, Crumpling-based soft metamaterials: the effects of sheet pore size and porosity, *Scientific Reports*, 7, Article number: 13028 (2017), doi:10.1038/s41598-017-12821-6

dant in real world applications [232]. Inherently random geometric configurations in crumpled-based metamaterials make them less sensitive to topological and geometrical imperfections as compared to ordered metamaterials whose material properties are strongly dependent on precisely controlled topological designs. Moreover, controlled crumpling provides a way for transforming the shape of initially flat structures to a complex three-dimensional topology that gives rise to the desired metamaterial properties. The initially flat state of the matter could then be used to decorate the surface of the sheet with functionality-inducing features [239]. Therefore, crumpled structures are promising candidates for designing bio-metamaterial. However, their morphology and mechanical response need to be studied in order to tailor the desired properties. In the context of meta-biomaterials, i.e. metamaterials used for improving tissue regeneration, the surface features could, for example, be nano-patterned that guide stem cell differentiation and fate [45, 240]. For such applications, however, the crumpled shape of the meta-biomaterial should be porous to allow for cell migration, oxygenation, and nutrition. Starting from a holey thin sheet would allow for obtaining a porous crumpled shape with pore sizes and porosities dependent on the degree of crumpling and the area fraction of the sheet. This could provide a single-step approach for fabricating porous meta-biomaterials with (nano-) patterned surfaces.

In the recent work, the effect of material properties on morphology and mechanical response of a crumpled thin sheet was studied in detail experimentally and has been shown that there is a strong link between the morphology and mechanical response of the crumpled structure [232]. However, introducing holes to a flat sheet before crumpling can considerably change the crumpling mechanism and make it more complex. As far as we know, crumpling behavior of holey thin sheets has never been studied before, and the effects of hole size and hole area fraction on the physics of crumpling are unknown. In this paper, for the first time, we investigate the effects of hole size and area fraction on the crumpling behavior of thin elastic sheets in order to design bio-metamaterials.

5.2 Experimental Procedure

5.2.1 Sample Preparation and Test Setup

We have used Mylar sheets (CLAYRTON'S®) of 30 microns. Samples were divided into four different categories: i) Mylar sheets without any hole, in three different sizes: 300 mm $\times$ 300 mm, 268 mm $\times$ 268 mm, and 232 mm $\times$ 232 mm. The 300 mm by 300 mm samples were regarded as the reference samples while in the other two sizes in this category we have reduction of 20 % and 40 % of the area respect to the reference

sample. ii) Mylar sheets with a hole area fraction of 10 %, meaning that the total sheet area was ten times larger than the area of the holes. For the samples in this group, three unit cells size, L, of 30 mm $\times$ 30 mm, 20 mm $\times$ 20 mm and 10 mm $\times$ 10 mm with different hole sizes were chosen. iii) Mylar sheets with an initial hole area fraction of 20 %. Three different unit cell sizes, i.e. 10 mm by 10 mm, 20 mm by 20 mm, and 30 mm by 30 mm, with various hole sizes were considered. iv) Mylar sheets with an initial hole area fraction of 40 %. Similar to the samples in groups ii and iii, three hole sizes have been taken into account in this group. The total size of the sheet was kept constant (i.e. 300 mm $\times$ 300 mm) for the samples in groups ii to iv. The pores, D, (see Figure 5.1) in the sheets were created using standard arch punch sets. A total number of holes in a sheet are shown by m oriented in a regular pattern. For each group, eight specimens were tested. The number of specimens per group was determined based on a preliminary study.

We used an experimental setup similar to the one previously described in [232] for the crumpling of Mylar sheets to achieve an isotropic crumpling condition. The setup consists of a net of fishing wires uniformly distributed around the crumpled sheet. The wires go through a hole and are attached to a bucket that will be filled with different weights. Eight varying levels of weights were gradually added to the bucket, which resulted in stepwise crumpling of the specimens. The samples were allowed to relax for 3-5 min after adding each weight in order to reach the equilibrium. For every step, images were taken from the crumpled specimens using a digital camera. The images were taken in two perpendicular planes. A circle was fitted to the crumpled specimens to measure their size and, thus, their deformation. The average of the diameters measured in two planes was considered as the size of the sample (Figure 5.1). To validate the robustness of the experiments, Intra- and inter-observer analysis was also performed which will be described in Section 5.2.2.

To find out the maximum number of samples in order to reach a convergence in the crumpling exponent, we created four more specimens and added them to the current eight specimens that were tested in the group UC3030-40. We calculated the crumpling exponent by analyzing different permutations of these twelve specimens. 1000 simulations were performed to take into account all possible combinations. The difference between the mean value for the crumpling exponent calculated from fitting a power-law on twelve specimens and eight specimens were less than 2 %. Similar repetition analyses have been done for the samples in other groups. This analysis justified the maximum number of specimens (eight sample in this study) required to reach a convergence in the crumpling exponent.

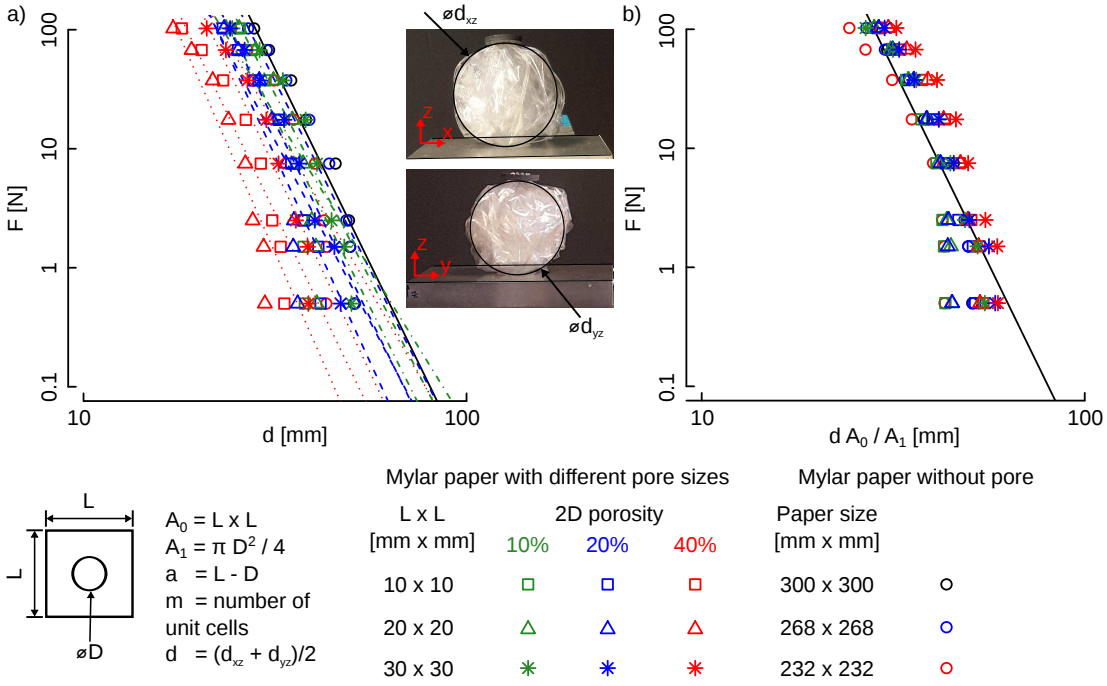

Figure 5.1: *Comparison of force, F, with respect to the deformed dimension, d, (a) and normalized deformation (b) for porous and non-porous Mylar sheets. Data are plotted on the logarithmic scale. Specific geometrical parameters for each unit cell are determined in Table 5.1. Points represent mean value of the compaction level, d, in these plots.*

5.2.2 Intra- and Inter- Observer Analysis

All tests have been done by one observer. As we are not following a standard test set up, and the test procedure seems to be subjective to the observer and initial condition, we performed inter- and intra-observer reliability analysis. For the inter-observer analysis, same experimenter repeated three tests for the samples in group UC1010-40 which this group was randomly selected. The mean± standard deviation for the crumpling exponent showed 0.45 % difference. As for the intra-observer reliability analysis, two more observers were asked to repeat and follow same test protocols this time for the samples in the group UC3030-20. Each observer performed three more tests. The crumpling exponent obtained from the tests of observer 2 and observer 3 was in less than 10 % difference that what obtained by the observer 1.

5.2.3 Micro-CT Scanning and Image Analysis

To study the role of hole edges on crumpling process, we used micro-computed tomography (μCT), where two-hole area fraction, i.e. 20 % and 40 %, were considered and three specimens were tested and scanned for each area fraction. The outer boundaries of the hole in the porous sheets were highlighted by spraying a zinc spray (Motip®).

Table 5.1: *Summary of geometrical parameters for porous, and non-porous Mylar sheets. These parameters are schematically presented in Figure 5.1. Crumpling exponent, n, is calculated by fitting a power-law model in $F \propto d^n$. The absolute value for n is presented in this table.*

Group	Size of the Mylar sheet [mm × mm]	Unit cell size ($L \times L$) [mm × mm]	$D\ [mm]$	$A_0\ [mm^2]$	$A_1\ [mm^2]$	Initial porosity [%]	Number of pores, m	n
No por	300 × 300	300 × 300	0	100	100	0	0	6.59
No por-20	268 × 268	268 × 268	0	100	100	20	0	6.39
No por-40	232 × 232	232 × 232	0	100	100	40	0	5.60
UC1010-10	300 × 300	10 × 10	4	100	87.43	10	900	5.22
UC1010-20	300 × 300	10 × 10	5	100	80.37	20	900	6.13
UC1010-40	300 × 300	10 × 10	7	100	61.52	40	900	6.69
UC2020-10	300 × 300	20 × 20	7	400	361.52	10	225	6.09
UC2020-20	300 × 300	20 × 20	10	400	321.46	20	225	6.97
UC2020-40	300 × 300	20 × 20	15	400	223.29	40	225	7.31
UC3030-10	300 × 300	30 × 30	10	900	821.46	10	100	6.26
UC3030-20	300 × 300	30 × 30	15	900	723.29	20	100	6.60
UC3030-40	300 × 300	30 × 30	20	900	585.84	40	100	6.88

Zinc has a different attenuation coefficient as compared to Mylar, meaning that the pore edges could be distinguished with image analysis and the network of their positions could be tracked during the crumpling process. The sprayed zinc ring was created by offsetting the hole edges by 1 mm. The sprayed zinc remained adherent to the sheet as the crumpling process proceeded. A μCT scanner (Quantum FX, Perkin Elmer, USA) was used with a tube current and voltage of 180 μA and 90 kV, respectively. The acquired images had a spatial resolution of 40 μm. The total imaging time was about 2 minutes. The specimens were crumpled to different degrees (various levels of forces) using the same setup as described above. Their crumpling state was then frozen by wrapping a tape sticker around them. The specimens were then scanned in the μCT scanner. After scanning was completed, the sticker tape was removed from the sample, and the crumpling process was continued. Specimens were tested at five different loads. The orientation of the specimens did not change during scanning and loading.

Image analysis was performed with ImageJ [179]. Using a Gaussian filter (kernel size = 1.5), noises were removed from the image. The Otsu local thresholding method [181] was used for segmentation of images, which resulted in a binary image with a voxel value of 1 for the conductive ring and 0 for the air and plastic sheets (Figure 5.2a-b). Three-dimensional binary images were skeletonized using the relevant plugin in ImageJ [241]. The number of folding lines were measured by averaging the number of particles in the mid-planes of the skeletonized images (Figure 2c).

5.2.4 2D Scanning of Crumpled Samples

The distribution of the ridges and crease lines in both holey and non-holey crumpled sheets was measured by scanning and image analyzing the unfolded crumpled specimens. For that purpose, we scanned five non-holey specimens as well as specimens with 20 % hole area fraction using a laser scanner (Ricoh Afico mp c2050) with a resolution of 300 dots per inch (dpi) (Figure 5.3). The ridges and crease lines were identified in the scanned images using image processing algorithms available in ImageJ. The region of interest (ROI) was a square (240.7 mm $\times$ 240.7 mm) at the center of the unfolded sheets. A Gaussian filter with a kernel size of 1.5 was applied to minimize the noise present in the scanned images. Images were then converted to an 8-bit format, segmented using an Otsu thresholding algorithm, and skeletonized. We assumed that the length of the pixels in the skeletonized image corresponds to the hinge lines in the crumpled structure.

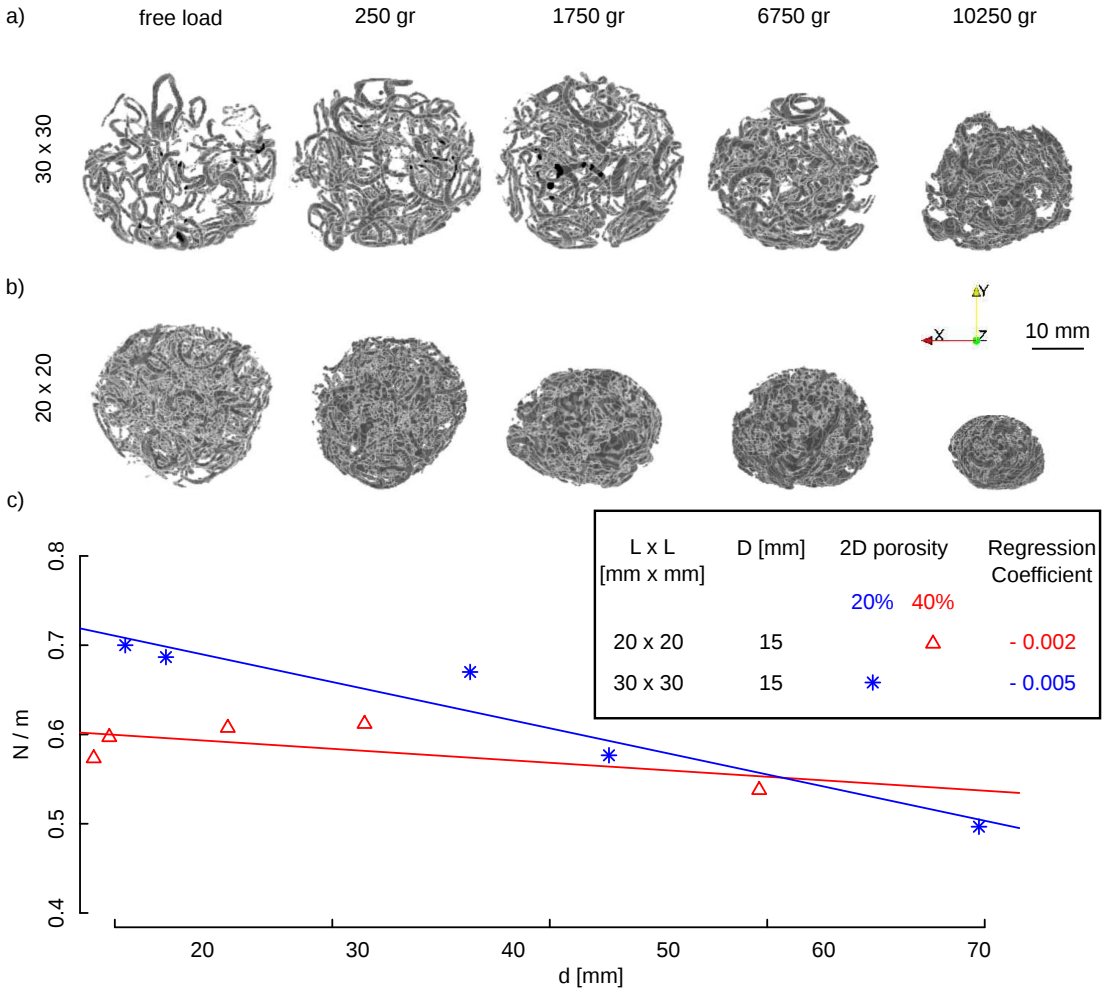

Figure 5.2: *µCT imaging of porous sheets with two levels of porosity of 20 % (a) and 40 % (b). The pores in the sheets were highlighted by a conductive spray. The resolution of the µCT image is 40 µm. c) Average of the number of folds from a skeletonize image calculated from three middle planes in the µCT image. The number of folding lines seem to be constant during the compaction.*

5.3 Results and Discussion

Based on the random nature of the experiments, a variation in the results was observed. The mean ± standard deviation of the compaction level under different level of applied forces for all the specimens are presented in Table 5.2.

The force-size curves measured for the specimens from different groups were generally similar in trend and seemed to be merely shifted (Figure 5.1a). Once scaled with the ratio of the hole area to the unit cell area, i.e. $\frac{A_0}{A_1}$, the shift observed in the absolute force-deformation curves disappeared to a large extent and the majority of the data points collapsed into one single trend-line (Figure 5.1b). We, therefore, concluded that reduction in the area fraction is the most important factor controlling the crumpling be-

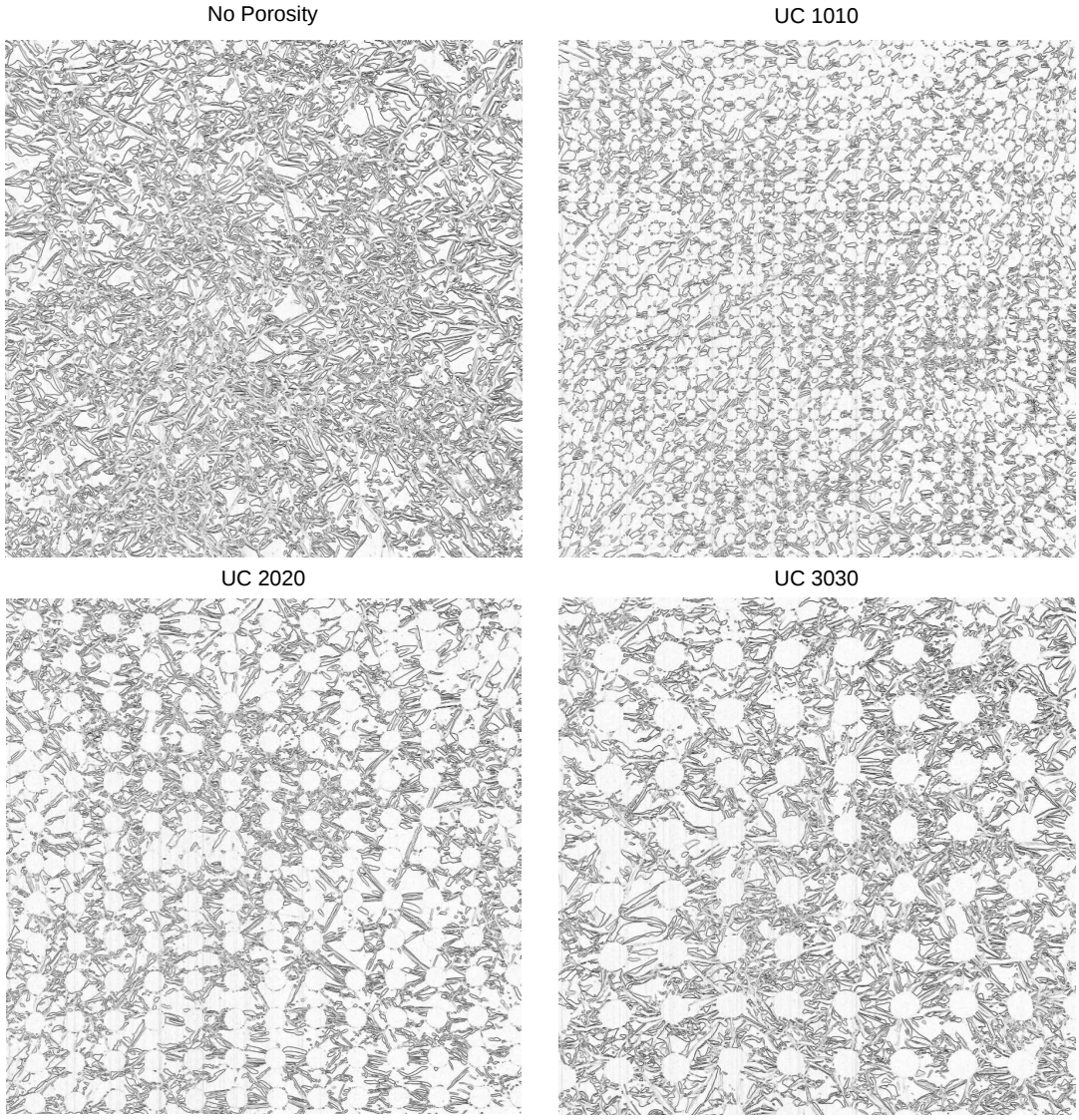

Figure 5.3: *2D scans of Mylar sheets with different pore size.*

havior of the holey Mylar sheet. A linear regression model in the logarithmic scale was fitted to the force-deformation data to obtain the power, n, of the power law ($F \propto d^n$) best describing the compaction behavior of the specimens (Table 5.1). Statistical analysis was performed with R [188].

Crumpling a piece of paper into a ball and crushing the structure increases the density by reducing the radius of the ball. It is well known that the average number of layers increases in a power-law manner with the size which results in a power-law dependence of the force required for the compaction of the structure with its size [232]. It has been shown that a simple folding model could capture the important features of disordered crumpling, including the above-mentioned power-law dependence. For a sheet,

folded n times repeatedly, the number of the layers and the effective bending rigidity of the structure grows exponentially with the number of folding events n. Translating the number of folding events into the final size of the structure explains the power-law dependence of the number of layers and compaction force on the size [236].

We therefore expected to have a power-law dependence between the force and size in our system. By plotting the force and the size in a log-log scale we observed the expected behavior. However, for the first two data points in each series, corresponding to small compaction forces at the beginning of the process, we observed deviations from the expected trend. The exponents are obtained by fitting power law to the experimental data. The fitted curves are represented by straight lines in log-log scales where the slope of the lines give the exponents.

At the beginning of the compaction process, when the compaction force is small, the crumpled structure is not spatially isotropic and the average number of layers is only 2 or 3 layers. Therefore, the force distribution around the structure is not uniform. This causes smaller average size and deviation from the power law expected for the force-size behavior, as shown in Figure 5.1. By increasing the compaction force, the average number of layers increases and we achieve more isotropic structures which consequently satisfy the power-law trend, as it is expected.

The crumpling exponents, n, laid between the relatively limited range of 5.22 to 7.3 (Table 5.1). The crumpling exponents calculated for the normal Mylar sheets in this study are within the range of those reported in [232]. These observations further support the conclusion that the area fraction merely scales the crumpling behavior of holey sheets to a large extent similar to that of the normal sheet. There are, however, some secondary effects that arise due to the presence of the hole edges. For example, there is a clear trend in the crumpling exponents where for a unit cell size, the crumpling exponent increases with both hole area fraction (Figure 5.4a) and the perimeter of the hole edges (Figure 5.4b). The increased crumpling exponents indicate that the force required for crumpling increases more rapidly for the sheets with more holes. This could be attributed to the effects of interlocking of hole edges and increase the frictional contacts that require more force to overcome as compared to the crumpling of normal sheets.

We also defined ligament slenderness ratio as $\frac{a}{L}$ similar to slenderness ratio in the buckling of columns. Ligament slenderness ratio equals to 1 shows a sheet without a hole. This parameter shows an inverse trend with respect to the crumpling exponent (Figure 5.4c).

The number of folds, N, related to the hole edges increased with the compaction level (i.e. the size of crumpled object d) (Figure 5.2). This is expected and is con-

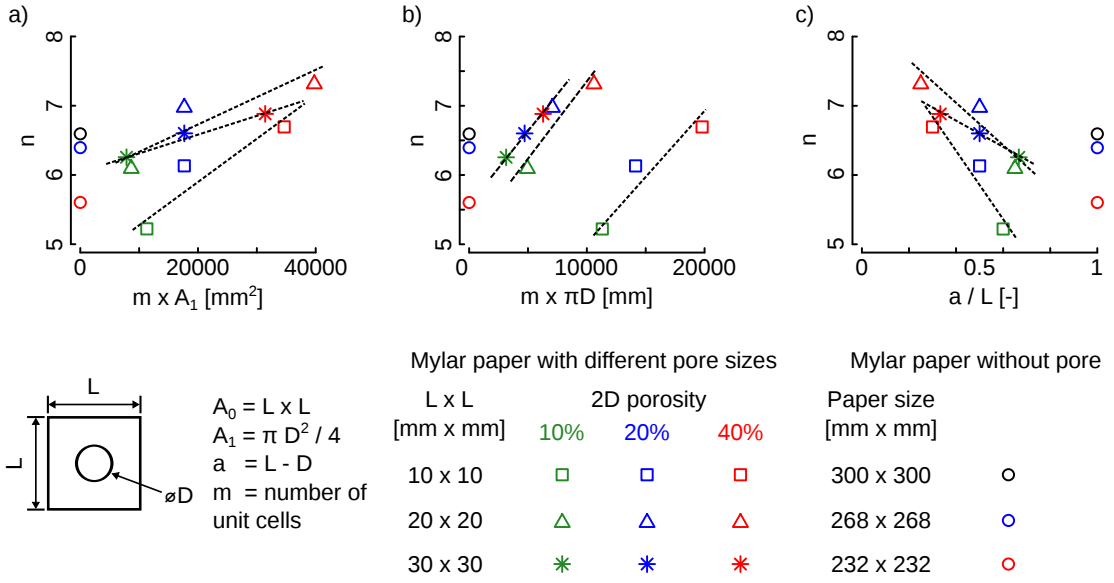

Figure 5.4: *Comparison of the crumpling exponent, n, with respect to a) total area fraction reduction, b) total perimeters of pores in the sheets, c) ligament slenderness ratio, $\frac{a}{L}$. Absolute value for n is presented here. Fitted lines are only drawn to clarify the general trends and as guides for the eye.*

sistent with what has been found before for normal sheets where the total number of layers in the crumpled structure has been found to increase the compaction level [232, 235, 236, 242]. Once scaled with respect to the number of holes in the sheet, m, the trend lines cross each other for large d values (Figure 5.4b), indicating similar starting points. The rate of increase in the number of edge-related folds is, however, around 2.5 times slower in sheets with higher hole area fraction (Figure 5.2b). This indicates that fewer hole edges fold in sheets with higher hole area fraction, while the crumpling process proceeds (Figure 5.2b). Given that increased hole area fraction slows down the process of hole-edge folding, alternative paths that are energetically less favorable have to be found for the crumpling process to proceed. Those less energetically favorable pathways could explain the increase in the crumpling exponent with hole area fraction (Figure 5.4a).

Analysis of the crease line and ridge patterns indicates that the length of the lines is generally smaller in crumpled holey sheets as one expects (Figure 5.5a-d). The hierarchical folding mechanism which occurs during the crumpling process supposed to show log-normal distribution. However, it has been previously shown that at high compaction rate the hierarchical nature of crumpling is influenced by self-avoid interactions [243]. To obtain the distribution of the ridges in different specimens a log-normal distribution was fitted to the histogram of the hinge length using the fitdistplus package in R [244]. The log-normal distribution was computed using the pooled data for each

group as follows:

$$f(l) = \frac{1}{l\sigma\sqrt{2\pi}} e^{-\frac{(ln(l)-\mu)^2}{2\sigma^2}} \tag{5.1}$$

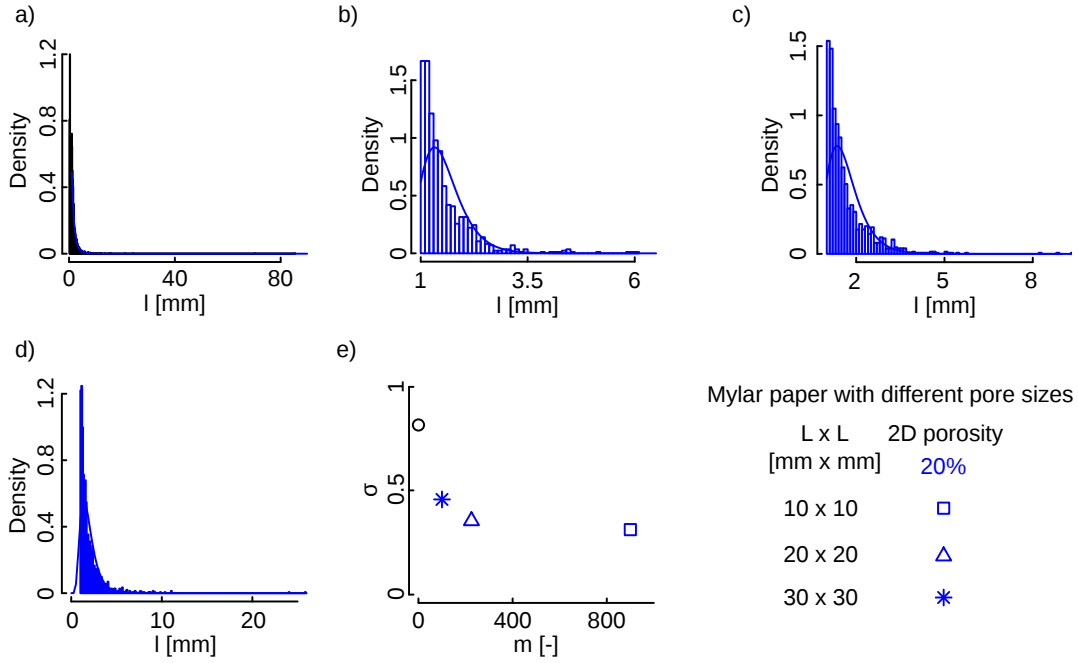

Figure 5.5: *Histogram of distribution of ridges for a) non-porous, b) 10 mm × 10 mm, c) 20 mm × 20 mm, d) 30 mm × 30 mm unit cells. A similar level of areal fraction reduction equal to 20 % was chosen for the holey sheets. Histograms show the pooled data for each specimen which contain five samples. The solid lines overlaid on the histogram show the log-normal distribution fitting. e) The standard deviation calculated from the log-normal fit for different porous and non-porous Mylar sheets.*

where l is the hinge lines, and μ and σ are the mean and standard deviation, respectively. The standard deviation calculated for the log-normal distributions, σ, decreases as the number of holes increases (keeping the initial hole area fraction constant) (Figure 5.5e). Both above-mentioned observations suggest that hole edges act as boundaries limiting and guiding the propagation of crease lines and ridges. Several previous studies have investigated the patterns of crease lines and ridges in normal crumpled sheets [233, 234, 242, 245]. By extrapolating the results of the log-normal distribution reported in [233] to obtain the standard deviation for sheets with a thickness of 30 μm, one could obtain a standard deviation, σ, of 1.14. This value is calculated for a different material (i.e. paper) and could be compared with the value we obtained for our normal Mylar sheets (i.e. 0.82) (Figure 5.5e).

5.4 Conclusion

In summary, we found area fraction of the hole to be the dominant factor influencing the crumpling behavior of holey thin sheets. The force-deformation curves were largely similar when scaled with respect to the hole area fraction and the crumpling exponents laid in a relatively small range. Pore edges were, however, found to affect the crumpling behavior to some extent. In particular, the crumpling exponents increased with increasing the area fraction and total hole perimeter. Moreover, increased hole area fraction limited the formation of the hole edge folds. Finally, hole edges seemed to act as boundaries limiting and guiding the propagation of crease lines and ridges within the sheet.

Table 5.2: *The mean ± standard deviation for the level of compaction at different levels of loading for all specimens.*

$Force\,[N]$	$d\,[mm]$											
	No por	No por-20	No por-40	UC1010-10	UC1010-20	UC1010-40	UC2020-10	UC2020-20	UC2020-40	UC3030-10	UC3030-20	UC3030-40
0.50	50.9± 5.0	51.1± 8.1	43.1± 9.9	37.8± 3.4	41.6± 3.7	33.4± 1.6	40.7± 5.1	36.2± 3.7	29.7± 2.0	50.1± 6.6	46.9± 4.0	38.6± 4.5
1.50	49.7± 4.2	49.6± 7.0	43.0± 8.9	37.5± 3.4	41.0± 3.3	32.7± 0.8	40.4± 4.8	35.3± 4.3	29.5± 1.9	47.9± 5.6	45.2 ± 2.8	38.5± 3.2
2.50	49.3± 2.9	48.5± 6.1	42.5± 8.6	37.2± 3.3	37.6± 4.7	31.1± 2.7	39.4± 3.4	35.4± 3.8	27.6± 2.3	44.4± 3.1	40.2± 3.5	35.8± 3.3
7.50	45.5± 4.3	43.8± 4.4	40.2± 6.2	35.9± 3.4	34.8± 4.8	29.0± 2.7	37.4± 2.5	33.8± 3.3	26.4± 3.0	40.7± 3.8	36.6± 3.1	32.3± 3.1
17.50	38.1± 2.9	38.9± 2.1	35.4± 2.7	32.8± 1.3	32.3± 3.5	26.5± 2.0	35.1± 2.2	31.0± 3.3	23.9± 1.8	38.0± 3.7	33.4± 2.4	30.0± 3.1
37.50	34.8± 2.8	33.8± 2.0	31.4± 2.6	29.9± 1.8	27.9± 3.5	23.1± 2.2	31.3± 2.1	28.7± 2.9	21.7± 1.8	33.1± 2.5	28.8± 3.2	26.8± 1.9
67.50	30.5± 3.4	30.1± 2.3	26.8± 2.1	27.5± 1.9	25.3± 2.9	20.3± 1.8	28.1± 2.0	25.3± 2.7	19.1± 1.2	28.8± 1.2	26.3± 2.5	23.5± 1.4
102.50	28.0± 1.5	26.9± 1.8	24.3± 2.4	25.6± 1.4	23.1± 1.8	18.0± 1.9	25.5± 1.6	23.3± 2.4	17.1± 1.5	24.5± 1.8	24.1± 1.8	21.0± 2.2

CHAPTER 6

Concluding Remarks

Within different studies in this thesis project, we were able to implement two of most important key design elements found in biological substances, known as functional gradient and randomness, in the design of bio-inspired cellular materials. For this purpose, we used and modified different manufacturing techniques such as conventional foaming processes, additive manufacturing and crumpling process. Such an implementation led to various mechanical and functional properties.

We summarize the important remarks obtained in these studies:

- We were able to modify the foaming production technique to reach closed-cell aluminum foam with similar morphological and mechanical properties as trabecular bones. That modification resulted in different pore propagation within the structure including, heterogeneous, anisotropic or gradient pore distribution. That modification can also be considered as a way of achieving various mechanical properties of such materials.
- As a consequence, we showed how proper design of geometrical features in the cellular materials could be used to reach enhanced mechanical properties.
- We used and introduced randomness as a design tool to reach properties that cannot be reached by single uniform (homogeneous) materials. This has importance

as random geometric configurations make the design less sensitive to the topological and geometrical imperfections. That strategy was used for independent tailoring of elastic stiffness and Poisson's ratio in mechanical soft metamaterials.

- It also has been shown that controlling and programming the functionality of advanced materials can be achieved by the rational design of their geometrical features. We used that in shape prediction using metamaterials when such materials are under mechanical loading.
- We also introduced crumpling as an easy method for the fabrication of materials with robust mechanical properties. This manufacturing method is aimed to be used in the design of meta-biomaterials.

Based on the results of these projects, we propose the following plans for the future works. Some of these projects are ongoing at the submission date of this thesis.

- We proposed two modifications for the manufacturing of bone-inspired closed-cell aluminum foams, i.e., positioning of precursor and using hot rolling. These two methods will result in graded and elongated pore distribution in the foam structures, respectively. This can be further studied how mechanical and morphological properties of foam materials can be altered if one combines these two processes consequently.
- Functional gradient in the microstructure of soft metamaterials can be analyzed with the aim of reaching different functional properties. We expect to have different microstructural deformations under macroscopic far-field stimuli.
- 3D production of soft-metamaterials can be another topic for the future analyses. This needs a proper design of unit cell in three-dimensional space.
- The idea of randomness can be extended to various other shapes for the unit cells. That can also be used for reaching other properties.
- With the current multi-materials additive manufacturing techniques, it is also possible to fabricate multi-materials with random (stochastic) mechanical properties where these properties are spatially distributed in the structure.
- Crumpling process can be done under the more controllable experimental procedure. The idea of 2D functionalization and converting to 3D structures can also be investigated more thoroughly by designing experimental packages and works. This process can be used as a platform for designing new scaffolds. Therefore it also requires more investigation from the biological point of view and cell cultural

analysis. All of it needs further collaboration with other sectors such as material scientist, biological engineers, and physicians.

List of Figures

List of Tables

Bibliography

[1] J. F. Vincent, O. A. Bogatyreva, N. R. Bogatyrev, A. Bowyer, and A.-K. Pahl, "Biomimetics: its practice and theory," *Journal of the Royal Society Interface*, vol. 3, no. 9, pp. 471–482, 2006.

[2] J. W. Dunlop and P. Fratzl, "Biological composites," *Annual Review of Materials Research*, vol. 40, pp. 1–24, 2010.

[3] P.-Y. Chen, A. Lin, Y.-S. Lin, Y. Seki, A. Stokes, J. Peyras, E. Olevsky, M. Meyers, and J. McKittrick, "Structure and mechanical properties of selected biological materials," *Journal of the Mechanical Behavior of Biomedical Materials*, vol. 1, no. 3, pp. 208–226, 2008.

[4] Z. Liu, M. A. Meyers, Z. Zhang, and R. O. Ritchie, "Functional gradients and heterogeneities in biological materials: Design principles, functions, and bioinspired applications," *Progress in Materials Science*, vol. 88, pp. 467 – 498, 2017.

[5] K. Oliver, A. Seddon, and R. S. Trask, "Morphing in nature and beyond: a review of natural and synthetic shape-changing materials and mechanisms," *Journal of Materials Science*, vol. 51, no. 24, pp. 10663–10689, 2016.

[6] F. Romei, *Leonardo Da Vinci*. The Oliver Press, 2008. ISBN 978-1-934545-00-3.

[7] W. Howard, Fred and Orville, *A Biography of the Wright Brothers*. Dober Publications, 1998. ISBN 978-0-486-40297-0.

[8] K. Okumura, "Strength and toughness of biocomposites consisting of soft and hard elements: A few fundamental models," *MRS Bulletin*, vol. 40, no. 4, pp. 333–339, 2015.

[9] J. M. Harkness, "In appreciation a lifetime of connections: Otto herbert schmitt, 1913-1998," *Physics in Perspective (PIP)*, vol. 4, no. 4, pp. 456–490, 2002.

[10] M. B. Janine *et al.*, "Biomimicry: Innovation inspired by nature," *Quill, New York*, 1997.

[11] B. Bhushan, "Biomimetics: lessons from nature–an overview," 2009.

[12] A. Nasto, M. Regli, P.-T. Brun, J. Alvarado, C. Clanet, and A. Hosoi, "Air entrainment in hairy surfaces," *Physical Review Fluids*, vol. 1, no. 3, p. 033905, 2016.

[13] S. Velcro, "Improvements in or relating to a method and a device for producing a velvet type fabric," *Swiss patent*, no. 721338, 1955.

[14] E. Snell-Rood, "Bring biologists into biomimetics: engineers, chemists and others taking inspiration from biological systems for human applications must team up with biologists," *Nature*, vol. 529, no. 7586, pp. 277–279, 2016.

[15] B. White, A. Sarkar, and A.-M. Kietzig, "Fog-harvesting inspired by the stenocara beetleâan analysis of drop collection and removal from biomimetic samples with wetting contrast," *Applied Surface Science*, vol. 284, pp. 826–836, 2013.

[16] S.-H. Yoon, J.-E. Roh, and K. L. Kim, "Woodpecker-inspired shock isolation by microgranular bed," *Journal of Physics D: Applied Physics*, vol. 42, no. 3, p. 035501, 2008.

[17] C. Yu, Y. Li, X. Zhang, X. Huang, V. Malyarchuk, S. Wang, Y. Shi, L. Gao, Y. Su, Y. Zhang, *et al.*, "Adaptive optoelectronic camouflage systems with designs inspired by cephalopod skins," *Proceedings of the National Academy of Sciences*, vol. 111, no. 36, pp. 12998–13003, 2014.

[18] M. A. Meyers, J. McKittrick, and P.-Y. Chen, "Structural biological materials: critical mechanics-materials connections," *science*, vol. 339, no. 6121, pp. 773–779, 2013.

[19] A. R. Studart, "Biological and bioinspired composites with spatially tunable heterogeneous architectures," *Advanced Functional Materials*, vol. 23, no. 36, pp. 4423–4436, 2013.

[20] M. A. Meyers, P.-Y. Chen, A. Y.-M. Lin, and Y. Seki, "Biological materials: structure and mechanical properties," *Progress in Materials Science*, vol. 53, no. 1, pp. 1–206, 2008.

[21] F. Libonati, *Bio-inspired Composite Materials: From Human Bone to Bone-like Composites*. PhD thesis, Politecnico di Milano, 2013.

[22] S. E. Naleway, M. M. Porter, J. McKittrick, and M. A. Meyers, "Structural design elements in biological materials: application to bioinspiration," *Advanced Materials*, vol. 27, no. 37, pp. 5455–5476, 2015.

[23] G. M. Genin and S. Thomopoulos, "The tendon-to-bone attachment: Unification through disarray," *Nature Materials*, vol. 16, no. 6, pp. 607–608, 2017.

[24] L. Rossetti, L. Kuntz, E. Kunold, J. Schock, K. Müller, H. Grabmayr, J. Stolberg-Stolberg, F. Pfeiffer, S. Sieber, R. Burgkart, *et al.*, "The microstructure and micromechanics of the tendon-bone insertion," *Nature Materials*, vol. 16, no. 6, pp. 664–670, 2017.

[25] S. P. Ho, S. J. Marshall, M. I. Ryder, and G. W. Marshall, "The tooth attachment mechanism defined by structure, chemical composition and mechanical properties of collagen fibers in the periodontium," *Biomaterials*, vol. 28, no. 35, pp. 5238–5245, 2007.

[26] B. P. Lee, P. B. Messersmith, J. N. Israelachvili, and J. H. Waite, "Mussel-inspired adhesives and coatings," *Annual review of materials research*, vol. 41, pp. 99–132, 2011.

[27] S. Bentov, P. Zaslansky, A. Al-Sawalmih, A. Masic, P. Fratzl, A. Sagi, A. Berman, and B. Aichmayer, "Enamel-like apatite crown covering amorphous mineral in a crayfish mandible," *Nature communications*, vol. 3, p. 839, 2012.

[28] N. Holten-Andersen, T. E. Mates, M. S. Toprak, G. D. Stucky, F. W. Zok, and J. H. Waite, "Metals and the integrity of a biological coating: the cuticle of mussel byssus," *Langmuir*, vol. 25, no. 6, pp. 3323–3326, 2008.

[29] A. Miserez, Y. Li, J. H. Waite, and F. Zok, "Jumbo squid beaks: inspiration for design of robust organic composites," *Acta Biomaterialia*, vol. 3, no. 1, pp. 139–149, 2007.

[30] A. Miserez, T. Schneberk, C. Sun, F. W. Zok, and J. H. Waite, "The transition from stiff to compliant materials in squid beaks," *Science*, vol. 319, no. 5871, pp. 1816–1819, 2008.

[31] G. Marshall, M. Balooch, R. Gallagher, S. Gansky, and S. Marshall, "Mechanical properties of the dentinoenamel junction: Afm studies of nanohardness, elastic modulus, and fracture," *Journal of Biomedical Materials Research Part A*, vol. 54, no. 1, pp. 87–95, 2001.

[32] I. H. Chen, W. Yang, and M. A. Meyers, "Alligator osteoderms: Mechanical behavior and hierarchical structure," *Materials Science and Engineering: C*, vol. 35, pp. 441–448, 2014.

[33] R. Elbaum, L. Zaltzman, I. Burgert, and P. Fratzl, "The role of wheat awns in the seed dispersal unit," *Science*, vol. 316, no. 5826, pp. 884–886, 2007.

[34] E. C. N. Silva, M. C. Walters, and G. H. Paulino, "Modeling bamboo as a functionally graded material: lessons for the analysis of affordable materials," *Journal of Materials Science*, vol. 41, no. 21, pp. 6991–7004, 2006.

[35] M. K. Habibi, A. T. Samaei, B. Gheshlaghi, J. Lu, and Y. Lu, "Asymmetric flexural behavior from bambooâs functionally graded hierarchical structure: underlying mechanisms," *Acta biomaterialia*, vol. 16, pp. 178–186, 2015.

[36] P.-Y. Chen, A. Stokes, and J. McKittrick, "Comparison of the structure and mechanical properties of bovine femur bone and antler of the north american elk (cervus elaphus canadensis)," *Acta Biomaterialia*, vol. 5, no. 2, pp. 693–706, 2009.

[37] K. Buckley, J. G. Kerns, H. L. Birch, P. D. Gikas, A. W. Parker, P. Matousek, and A. E. Goodship, "Functional adaptation of long bone extremities involves the localized âtuningâ of the cortical bone composition; evidence from raman spectroscopy," *Journal of biomedical optics*, vol. 19, no. 11, pp. 111602–111602, 2014.

[38] R. O. Ritchie, M. J. Buehler, and P. Hansma, "Plasticity and toughness in bone," 2009.

[39] Z. Liu, Y. Zhu, D. Jiao, Z. Weng, Z. Zhang, and R. O. Ritchie, "Enhanced protective role in materials with gradient structural orientations: Lessons from nature," *Acta biomaterialia*, vol. 44, pp. 31–40, 2016.

[40] L. J. Gibson and M. F. Ashby, "Cellular solids: Structure and properties," *Cambridge: Cambridge University Press*, no. 2nd edn, 1997.

[41] L. J. Gibson, M. F. Ashby, and B. A. Harley, *Cellular Materials in Nature and Medicine*. Cambridge University Express, 2010.

[42] K. E. Evans and A. Alderson, "Auxetic materials: functional materials and structures from lateral thinking!," *Advanced materials*, vol. 12, no. 9, pp. 617–628, 2000.

[43] Q. Liu, "Literature review: materials with negative poisson's ratios and potential applications to aerospace and defence," tech. rep., DTIC Document, 2006.

[44] A. A. Zadpoor, "Design for additive bio-manufacturing: From patient-specific medical devices to rationally designed meta-biomaterials," *International Journal of Molecular Sciences*, vol. 18, no. 8, p. 1607, 2017.

[45] A. A. Zadpoor, "Mechanical meta-materials," *Materials Horizons*, vol. 3, no. 5, pp. 371–381, 2016.

[46] W. Zhang, P. Soman, K. Meggs, X. Qu, and S. Chen, "Tuning the poisson's ratio of biomaterials for investigating cellular response," *Advanced functional materials*, vol. 23, no. 25, pp. 3226–3232, 2013.

[47] A. Spagnoli, R. Brighenti, M. Lanfranchi, and F. Soncini, "On the auxetic behaviour of metamaterials with re-entrant cell structures," *Procedia Engineering*, vol. 109, pp. 410–417, 2015.

[48] D. Li, L. Dong, and R. S. Lakes, "A unit cell structure with tunable poisson's ratio from positive to negative," *Materials Letters*, vol. 164, pp. 456 – 459, 2016.

[49] Y. Li, "The anisotropic behavior of poisson's ratio, young's modulus, and shear modulus in hexagonal materials," *physica status solidi (a)*, vol. 38, no. 1, pp. 171–175, 1976.

[50] D. J. Gunton and G. A. Saunders, "The young's modulus and poisson's ratio of arsenic, antimony and bismuth," *Journal of Materials Science*, vol. 7, no. 9, pp. 1061–1068, 1972.

[51] J. Williams and J. Lewis, "Properties and an anisotropic model of cancellous bone from the proximal tibial epiphysis," *Journal of biomechanical engineering*, vol. 104, no. 1, pp. 50–56, 1982.

[52] J. C. Matheny, *Understanding the Transition from Positive to Negative Poisson's Ratio Behavior in Cellular Materials and the Potential for Auxeticity in Trabecular Bone*. PhD thesis, The University of Toledo, 2011.

[53] D. Veronda and R. Westmann, "Mechanical characterization of skinâfinite deformations," *Journal of Biomechanics*, vol. 3, no. 1, pp. 111 – 124, 1970.

[54] C. Lees, J. F. Vincent, and J. E. Hillerton, "Poisson's ratio in skin," *Bio-medical materials and engineering*, vol. 1, no. 1, pp. 19–23, 1991.

[55] M. Sanami, *Auxetic materials for biomedical applications*. PhD thesis, University of Bolton, 2015.

[56] O. Levy, S. Krylov, and I. Goldfarb, "Design considerations for negative poisson ratio structures under large deflection for mems applications," *Smart Materials and Structures*, vol. 15, no. 5, p. 1459, 2006.

[57] A. Alderson and K. Alderson, "Auxetic materials," *Proceedings of the Institution of Mechanical Engineers, Part G: Journal of Aerospace Engineering*, vol. 221, no. 4, pp. 565–575, 2007.

[58] L. E. Freed, G. C. Engelmayr, J. T. Borenstein, F. T. Moutos, and F. Guilak, "Advanced material strategies for tissue engineering scaffolds," *Advanced Materials*, vol. 21, no. 32-33, pp. 3410–3418, 2009.

[59] G. C. Engelmayr Jr, M. Cheng, C. J. Bettinger, J. T. Borenstein, R. Langer, and L. E. Freed, "Accordion-like honeycombs for tissue engineering of cardiac anisotropy," *Nature materials*, vol. 7, no. 12, p. 1003, 2008.

[60] H. M. Kolken and A. Zadpoor, "Auxetic mechanical metamaterials," *RSC Advances*, vol. 7, no. 9, pp. 5111–5129, 2017.

[61] Z. Wang and H. Hu, "Auxetic materials and their potential applications in textiles," *Textile Research Journal*, vol. 84, no. 15, pp. 1600–1611, 2014.

[62] A. Bezazi and F. Scarpa, "Mechanical behaviour of conventional and negative poissonâs ratio thermoplastic polyurethane foams under compressive cyclic loading," *International Journal of Fatigue*, vol. 29, no. 5, pp. 922 – 930, 2007.

[63] R. Lakes, "Negative poisson's ratio materials: Response," *Science*, vol. 238, p. 551, 1987.

[64] H. Murakami and G. Hegemier, "Angle-ply laminates," *Mechanics Today: Pergamon Mechanics Today Series*, p. 329, 2014.

[65] R. V. Martinez, C. R. Fish, X. Chen, and G. M. Whitesides, "Elastomeric origami: programmable paper-elastomer composites as pneumatic actuators," *Advanced functional materials*, vol. 22, no. 7, pp. 1376–1384, 2012.

[66] R. Naboni and L. Mirante, "Metamaterial computation and fabrication of auxetic patterns for architecture," *Blucher Design Proceedings*, vol. 2, no. 3, pp. 129–136, 2015.

[67] K. Bertoldi, P. M. Reis, S. Willshaw, and T. Mullin, "Negative poisson's ratio behavior induced by an elastic instability," *Advanced Materials*, vol. 22, no. 3, pp. 361–366, 2010.

[68] Z. G. Nicolaou and A. E. Motter, "Mechanical metamaterials with negative compressibility transitions," *Nature materials*, vol. 11, no. 7, pp. 608–613, 2012.

[69] N. Novak, M. Vesenjak, and Z. Ren, "Computational simulation and optimization of functionally graded auxetic structures made from inverted tetrapods," *physica status solidi (b)*, 2017.

[70] A. Rafsanjani, A. Akbarzadeh, and D. Pasini, "Snapping mechanical metamaterials under tension," *Advanced Materials*, vol. 27, no. 39, pp. 5931–5935, 2015.

[71] O. Abdelaal and S. Darwish, "Analysis, fabrication and a biomedical application of auxetic cellular structures," *Int J Eng Innov Technol*, vol. 2, no. 3, pp. 218–23, 2012.

[72] X. Miao and D. Sun, "Graded/gradient porous biomaterials," *Materials*, vol. 3, no. 1, p. 26, 2010.

[73] I. Eldesouky, O. Abdelaal, and H. El-Hofy, "Femoral hip stem with additively manufactured cellular structures," in *2014 IEEE Conference on Biomedical Engineering and Sciences (IECBES)*, pp. 181–186, Dec 2014.

[74] S. M. Darwish and M. U. Aslam, "Auxetic cellular structures for custom made orthopedic implants using additive manufacturing," *International Journal of Engineering and Advanced Technology*, 2014.

[75] O. Rehme and C. Emmelmann, "Selective laser melting of honeycombs with negative poissonâs ratio," *J. Laser Micro/Nanoeng*, vol. 24, pp. 128–134, 2009.

[76] H. D. Espinosa, J. E. Rim, F. Barthelat, and M. J. Buehler, "Merger of structure and material in nacre and bone perspectives on de novo biomimetic materials," *Materials Science*, vol. 4, pp. 361 – 381, 2009.

[77] U. G. Wegst, H. Bai, E. Saiz, A. P. Tomsia, and R. O. Ritchie, "Bioinspired structural materials," *Nature materials*, vol. 14, no. 1, pp. 23–36, 2015.

[78] P.-Y. Chen, J. McKittrick, and M. A. Meyers, "Biological materials: Functional adaptations and bioinspired designs," *Progress in Materials Science*, vol. 57, pp. 1492 – 1704, 2012.

[79] T. M. Keaveny, E. F. Morgan, G. L. Niebur, and O. C. Yeh, "Biomechanics of trabecular bone," *Annual Review of Biomedical Engineering*, vol. 3, pp. 307 – 333, 2001.

[80] A. G. Reisinger, *Modeling and Validation of Multiscale Lamellar Bone Elasticity*. PhD thesis, Vienna University of Technology, 2011.

[81] J. Currey, "Minimum mass of cancellous bone," *Bone: structure and mechanics*, pp. 224 – 225, 1999.

[82] P. Fratzl and R. Weinkamer, "Nature's hierarchical materials," *Progress in Materials Science*, vol. 52, no. 8, pp. 1263 – 1334, 2007.

[83] N. Wachter, P. Augat, G. Krischak, M. Sarkar, M. Mentzel, L. Kinzl, and L. Claes, "Prediction of strength of cortical bone in vitro by microcomputed tomography," *Clinical Biomechanics*, vol. 16, no. 3, pp. 252–256, 2001.

[84] P. Zioupos, R. B. Cook, and J. R. Hutchinson, "Some basic relationships between density values in cancellous and cortical bone," *Journal of biomechanics*, vol. 41, no. 9, pp. 1961–1968, 2008.

[85] D. B. Burr, M. B. Schaffler, and R. G. Frederickson, "Composition of the cement line and its possible mechanical role as a local interface in human compact bone," *Journal of Biomechanics*, vol. 21, no. 11, pp. 939943–941945, 1988.

[86] T. M. Keaveny, E. F. Morgan, and O. C. Yeh, *Bone Mechanics*, ch. 8, pp. 8.1 – 8.17. 2004.

[87] M. Amling, S. Herden, M. Püsl, M. Hahn, H. Ritzel, and G. Delling, "Heterogeneity of the skeleton: Comparison of the trabecular microarchitecture of the spine, the iliac crest, the femur, and the calcaneus," *Journal of bone and mineral research*, vol. 11, no. 1, pp. 36 – 45, 1996.

[88] T. Hildebrand, A. Laib, R. Müller, J. Dequeker, and Rüesegger, "Direct three-dimensional morphometric analysis of human cancellous bone: Microstructural data from spine, femur, iliac crest, and calcaneus," *Journal of Bone and Mineral Research*, vol. 14, no. 7, pp. 1167 – 1174, 1999.

[89] I. H. Parkinson and N. L. Fazzalari, "Characterisation of trabecular bone structure," *Studies in Mechanobiology, Tissue Engineering and Biomateria*, vol. 5, pp. 31 – 51, 2013.

[90] J. Wolff, "The law of bone remodelling," *(English Edition) (Berlin: Springer)*, pp. 81 – 83, 1986.

[91] H. M. Frost, "Wolff's law and bone's structural adaptations to mechanical usage: an overview for clinicians," *The Angle Orthodontist*, vol. 64, no. 3, pp. 175 – 188, 1994.

[92] C. Öhman, M. Baleani, E. Perilli, E. Dall'Ara, S. Tassani, F. Baruffaldi, and M. Viceconti, "Mechanical testing of cancellous bone from the femoral head: Experimental errors due to off-axis measurements," *Journal of Biomechanics*, vol. 40, no. 11, pp. 2426 – 2433, 2007.

[93] K. Ün, G. Bevill, and T. M. Keaveny, "The effects of side-artifacts on the elastic modulus of trabecular bone," *Journal of Biomechanics*, vol. 39, no. 11, pp. 1955 – 1963, 2006.

[94] W. J. Whitehouse, "The quantitative morphology of anisotropic trabecular bone.," *Journal of Microscopy*, vol. 101, no. 2, pp. 153–168, 1974.

[95] R. Moreno, Ö. Smedby, and M. Borga, "On the efficiency of the mean intercept length tensor," in *SSBA Symposium*, 2011.

[96] T. P. Harrigan and R. W. Mann, "Characterisation of microstructural anisotropy in orthotropic materials using a second rank tensor," *Journal of Materials Sciences*, vol. 19, pp. 761 – 767, 1984.

[97] P. K. Zysset, "A review of morphology-elasticity relationships in human trabecular bone: Theories and experiments," *Journal of Biomechanics*, vol. 36, no. 10, pp. 1469 – 1485, 2003.

[98] S. C. Cowin, "The relationship between the elasticity tensor and the fabric tensor," *Mechanics of Materials*, vol. 4, pp. 137 – 147, 1985.

[99] M. F. Souzanchi, P. Palacio-Mancheno, Y. A. Borisov, L. Cardoso, and S. C. Cowin, "Microarchitecture and bone quality in the human calcaneus: Local variations of fabric anisotropy," *Journal of bone and mineral research*, vol. 27, no. 12, pp. 2562 – 2572, 2012.

[100] C. M. Gdyczynski, S. Hashemi, A. Manbachi, B. Lashkari, and R. S. C. Cobbold, "On estimating the directionality distribution in pedicle trabecular bone from micro-ct images," *Physiological Measurement*, vol. 35, pp. 2415 – 2428, 2014.

[101] T. Hildebrand and P. Rüegesegger, "A new method for the model-independent assessment of thickness in three-dimensional images," *Journal of Microscopy*, vol. 185, no. 1, pp. 67 – 75, 1997.

[102] T. Hildebrand and P. Rüegesegger, "Quantification of bone microarchitecture with the structure model index," *Computer Methods in Biomechanics and Biomedical Engineering*, vol. 1, pp. 15 – 23, 1997.

[103] E. X. Guo, *Bone Mechanics*, ch. Mechanical Properties of Cortical Bone and Cancellous Bone Tissue, pp. 10–1 – 10–23. CRC Press LLC, 2001.

[104] H. S. Hosseini, D. H. Pahr, and Z. P. K., "Modeling and experimental validation of trabecular bone damage, softening and densification under large compressive strains.," *Journal of the Mechanical Behavior of Biomedical Materials*, vol. 15, pp. 93 – 102, 2012.

[105] D. L. Kopperdahl and T. M. Keaveny, "Yield strain behaviour of trabecular bone," *Journal of Biomechanics*, vol. 31, no. 7, pp. 601 –608, 1998.

[106] M. Fondrk, E. Bahniuk, D. T. Davy, and C. Michaels, "Some viscoplastic characteristics of bovine and human cortical bone," *Journal of Biomechanics*, vol. 21, no. 8, pp. 623 – 630, 1988.

[107] U. Wolfram, H.-J. Wilke, and P. K. Zysset, "Damage accumulation in vertebral trabecular bone depends on loading mode and direction," *Journal of Biomechanics*, vol. 44, no. 6, pp. 1164 – 1169, 2011.

[108] M. J. Mirzaali, A. Bürki, J. Schwiedrzik, P. K. Zysset, and U. Wolfram, "Contiuum damage interactions between tension and compression in osteonal bone," *Journal of the Mechanical Behavior of Biomedical Materials*, vol. 49, pp. 355 – 369, 2015.

[109] N. Kelly and J. P. McGarry, "Experimental and numerical characterisation of the elasto-plastic properties of bovine trabecular bone and a trabecular bone analogue.," *Journal of the mechanical behavior of biomedical materials*, vol. 9, pp. 184–97, May 2012.

[110] L. J. Gibson, "Biomechanics of cellular solids," *Journal of Biomechanics*, vol. 38, pp. 377 – 399, 2005.

[111] T. Guillén, Q.-H. Zhang, G. Tozzi, a. Ohrndorf, H.-J. Christ, and J. Tong, "Compressive behaviour of bovine cancellous bone and bone analogous materials, microCT characterisation and FE analysis.," *Journal of the mechanical behavior of biomedical materials*, vol. 4, pp. 1452–61, Oct. 2011.

[112] H. H. Bayraktar, E. F. Morgan, G. L. Niebur, G. E. Morris, E. K. Wong, and T. M. Keaveny, "Comparison of the elastic and yield properties of human femoral trabecular and cortical bone tissue," *Journal of Biomechanics*, vol. 37, no. 1, pp. 27 – 35, 2004.

[113] J. Rho, T. Y. Tsui, and G. M. Pharr, "Elastic properties of microstructural components of human bone tissue as measured by nanoindentation," *Journal of Biomedical Materials Research*, vol. 45, no. 1, pp. 48 – 58, 1999.

[114] G. L. Niebur, M. J. Feldstein, J. C. Yuen, T. J. Chen, and T. M. Keaveny, "High-resolution finite element models with tissue strength asymmetry accurately predict failure of trabecular bone," *Journal of Biomechanics*, vol. 33, no. 12, pp. 1575 – 1583, 2000.

[115] C. H. Turner, S. C. Cowin, J. Y. Rho, R. B. Ashman, and J. C. Rice, "The fabric dependence of the orthotropic elastic constants of cancellous bone," *Journal of Biomechanics*, vol. 23, no. 6, pp. 549 – 561, 1990.

[116] P. K. Zysset and L. Rincón-Kohli, *An Alternative Fabric-based Yield and Failure Criterion for Trabecular Bone*, ch. Part V, pp. 457 – 470. Springer-Verlag Berlin Heidelberg, 2006.

[117] L. Rincón-Kohli and P. Zysset, "Multi-axial mechanical properties of human trabecular bone," *Journal of Biomechanics and Modelling in Mechanobiology*, vol. 8, no. 3, pp. 195 – 208, 2009.

[118] M. J. Wald, J. F. Magland, C. S. Rajapakse, Y. A. Bhagat, and F. W. Wehrli, "Predicting trabecular bone elastic properties from measures of bone volume fraction and fabric on the basis of micromagnetic resonance images," *Magnetic Resonance in Medicine*, vol. 68, pp. 463 – 473, 2012.

[119] M. Matsuura, F. Eckstein, E. Lochmüller, and P. Zysset, "The role of fabric in the quasi-static compressive mechanical properties of human trabecular bone from various anatomical locations," *Biomechanics and Modelling in Mechanobiology*, vol. 7, no. 1, pp. 27 – 42, 2007.

[120] M. Charlebois, M. Pretterklieber, and P. K. Zysset, "The role of fabric in the large strain compressive behavior of human trabecular bone.," *Jounral of Biomechanical Engineering*, vol. 132, no. 12, pp. 121006–1 – 121006–10, 2010.

[121] U. Wolfram, T. Gross, D. Pahr, J. Schwiedrzik, H.-J. Wilke, and P. K. Zysset, "Fabric based tsai-wu yield criteria for vertebral trabecular bone in stress and strain space.," *Journal of the Mechanical Behavior of Biomedical Materials*, vol. 15, no. 15C, pp. 218 – 228, 2012.

[122] J. J. Schwiedrzik, U. Wolfram, and P. K. Zysset, "A generalized anisotropic quadric yield criterion and its application to bone tissue at multiple length scales.," *Biomech Model Mechanobiol*, vol. 12, pp. 1155 – 1168, 2013.

[123] M. J. Mirzaali, J. J. Schwiedrzik, S. Thaiwichai, J. P. Best, J. Michler, P. K. Zysset, and U. Wolfram, "Mechanical properties of cortical bone and their relationships with age, gender, composition and microindentation properties in the elderly.," *Journal of Bone*, 2015.

[124] P. K. Zysset and A. Curnier, "A 3d damage model for trabecular bone based on fabric tensors," *Journal of Biomechanics*, vol. 29, pp. 1549 – 1558, 1996.

[125] C. M. Fenech and T. M. Keaveny, "A cellular solid criterion for predicting the axial-shear failure properties of bovine trabecular bone," *Journal of Biomechanical Engineering*, vol. 121, no. 4, pp. 414 – 422, 1999.

[126] T. M. Keaveny, E. F. Wachtel, S. P. Zadesky, and Y. P. Arramon, "Application of the tsai-wu quadratic multiaxial failure criterion to bovine trabecular bone," *Journal of Biomechanical Engineering*, vol. 121, no. 1, pp. 99 – 107, 1999.

[127] Y. Chevalier, D. Pahr, and P. K. Zysset, "The role of cortical shell and trabecular fabric in finite element analysis of the human vertebral body," *Journal of Biomechanical Engineering*, vol. 131, no. 11, pp. 111003–1 – 111003–12, 2009.

[128] F. Libonati and M. J. Buehler, "Advanced structural materials by bioinspiration," *Advanced Engineering Materials*, 2017.

[129] G. X. Gu, I. Su, S. Sharma, J. L. Voros, Z. Qin, and M. J. Buehler, "Three-dimensional-printing of bio-inspired composites," *Journal of biomechanical engineering*, vol. 138, no. 2, p. 021006, 2016.

[130] S. Deville, E. Saiz, R. K. Nalla, and A. P. Tomsia, "Freezing as a path to build complex composites," *Science*, vol. 311, no. 5760, pp. 515–518, 2006.

[131] E. Munch, M. E. Launey, D. H. Alsem, E. Saiz, A. P. Tomsia, and R. O. Ritchie, "Tough, bio-inspired hybrid materials," *Science*, vol. 322, no. 5907, pp. 1516–1520, 2008.

[132] M. M. Porter, *Bioinspired Design: Magnetic Freeze Casting*. University of California, San Diego, 2014.

[133] M. Mirkhalaf, A. K. Dastjerdi, and F. Barthelat, "Overcoming the brittleness of glass through bio-inspiration and micro-architecture," *Nature communications*, vol. 5, 2014.

[134] M. Taufik and P. K. Jain, "Additive manufacturing: Current scenario," 2016.

[135] C. K. Chua and W. Y. Yeong, *Bioprinting: principles and applications*, vol. 1. World Scientific Publishing Co Inc, 2014.

[136] H. Tseng, L. R. Balaoing, B. Grigoryan, R. M. Raphael, T. Killian, G. R. Souza, and K. J. Grande-Allen, "A three-dimensional co-culture model of the aortic valve using magnetic levitation," *Acta biomaterialia*, vol. 10, no. 1, pp. 173–182, 2014.

[137] J. J. Martin, B. E. Fiore, and R. M. Erb, "Designing bioinspired composite reinforcement architectures via 3d magnetic printing," *Nature communications*, vol. 6, 2015.

[138] L. S. Dimas, G. H. Bratzel, I. Eylon, and M. J. Buehler, "Tough composites inspired by mineralized natural materials: Computation, 3d printing, and testing," *Advanced Functional Materials*, vol. 23, pp. 4629 – 4638, 2013.

[139] G. X. Gu, F. Libonati, S. Wettermark, and M. J. Buehler, "Printing nature: Unraveling the role of nacre's mineral bridges," *Journal of the Mechanical Behavior of Biomedical Materials*, 2017.

[140] A. K. Rajasekharan, R. Bordes, C. Sandström, M. Ekh, and M. Andersson, "Hierarchical and heterogeneous bioinspired compositesâmerging molecular self-assembly with additive manufacturing," *Small*, 2017.

[141] T. A. Pham, D.-P. Kim, T.-W. Lim, S.-H. Park, D.-Y. Yang, and K.-S. Lee, "Three-dimensional sicn ceramic microstructures via nano-stereolithography of inorganic polymer photoresists," *Advanced Functional Materials*, vol. 16, no. 9, pp. 1235–1241, 2006.

[142] M. Mott, J.-H. Song, and J. R. Evans, "Microengineering of ceramics by direct ink-jet printing," *Journal of the American Ceramic Society*, vol. 82, no. 7, pp. 1653–1658, 1999.

[143] M. M. Porter and J. McKittrick, "Itâs tough to be strong: Advances," *Am. Ceram. Soc. Bull*, vol. 93, pp. 18–24, 2014.

[144] P. M. Hunger, A. E. Donius, and U. G. Wegst, "Platelets self-assemble into porous nacre during freeze casting," *Journal of the mechanical behavior of biomedical materials*, vol. 19, pp. 87–93, 2013.

[145] M. E. Launey and R. O. Ritchie, "On the fracture toughness of advanced materials," *Advanced Materials*, vol. 21, no. 20, pp. 2103–2110, 2009.

[146] F. Libonati, C. Colombo, and L. Vergani, "Design and characterization of a biomimetic composite inspired to human bone," *Fatigue and Fracture of Engineering Materials and Structures*, vol. 37, pp. 772 – 781, 2014.

[147] F. Libonati, G. X. Gu, Z. Qin, L. Vergani, and M. J. Buehler, "Bone-inspired materials by design: Toughness amplification observed using 3d printing and testing," *Advanced Engineering Materials*, vol. 18, no. 8, pp. 1354–1363, 2016.

[148] X. Jin, B. Shi, L. Zheng, X. Pei, X. Zhang, Z. Sun, Y. Du, J. H. Kim, X. Wang, S. Dou, K. Liu, and L. Jiang, "Bio-inspired multifunctional metallic foams through the fusion of different biological solutions," *Advanced Functional Materials*, vol. 14, pp. 2721 – 2726, 2014.

[149] M. M. Porter, M. Yeh, J. Strawson, T. Goehring, S. Lujan, P. Siripasopsotorn, M. A. Meyers, and J. McKittrick, "Magnetic freeze casting inspired by nature," *Materials Science and Engineering: A*, vol. 556, pp. 741 – 750, 2012.

[150] H. Le Ferrand, F. Bouville, T. P. Niebel, and A. R. Studart, "Magnetically assisted slip casting of bioinspired heterogeneous composites," *Nature materials*, vol. 14, no. 11, pp. 1172–1179, 2015.

[151] L. Cheng, A. Thomas, J. L. Glancey, and A. M. Karlsson, "Mechanical behavior of bio-inspired laminated composites," *Composites Part A: Applied Science and Manufacturing*, vol. 42, no. 2, pp. 211 – 220, 2011.

[152] D. Kokkinis, M. Schaffner, and A. R. Studart, "Multimaterial magnetically assisted 3d printing of composite materials," *Nature communications*, vol. 6, 2015.

[153] R. Lakes, "Materials with structural hierarchy," *Nature*, vol. 361, no. 6412, pp. 511–515, 1993.

[154] J.-Y. Rho, L. Kuhn-Spearing, and P. Zioupos, "Mechanical properties and the hierarchical structure of bone," *Medical engineering & physics*, vol. 20, no. 2, pp. 92–102, 1998.

[155] J. D. Currey, "Hierarchies in biomineral structures," *Science*, vol. 309, no. 5732, pp. 253–254, 2005.

[156] U. G. Wegst, "Bending efficiency through property gradients in bamboo, palm, and wood-based composites," *Journal of the mechanical behavior of biomedical materials*, vol. 4, no. 5, pp. 744–755, 2011.

[157] M. Thielen, C. N. Z. Schmitt, S. Eckert, T. Speck, and R. Seidel, "Structureâfunction relationship of the foam-like pomelo peel (citrus maxima)âan inspiration for the development of biomimetic damping materials with high energy dissipation," *Bioinspiration & Biomimetics*, vol. 8, no. 2, p. 025001, 2013.

[158] J. Qin, Q. Chen, C. Yang, and Y. Huang, "Research process on property and application of metal porous materials," *Journal of Alloys and Compounds*, vol. 654, pp. 39 – 44, 2016.

[159] J. Banhart, "Manufacturing routes for metallic foams," *JOM*, vol. 52, no. 12, pp. 22–27, 2000.

[160] J. Banhart, "Light-metal foamsâhistory of innovation and technological challenges," *Advanced Engineering Materials*, vol. 15, no. 3, pp. 82–111, 2013.

[161] L.-P. Lefebvre, J. Banhart, and D. Dunand, "Porous metals and metallic foams: current status and recent developments," *Advanced Engineering Materials*, vol. 10, no. 9, pp. 775–787, 2008.

[162] M. F. Ashby, A. G. Evans, N. A. Fleck, L. J. Gibson, J. W. Hutchinson, and H. N. G. Wadley, *Metal Foams: A Design Guide*. Butterworth-Heinemann, 2000.

[163] P. Pinnoji, P. Mahajan, N. Bourdet, C. Deck, and R. Willinger, "Impact dynamics of metal foam shells for motorcycle helmets: Experiments & numerical modeling," *International Journal of Impact Engineering*, vol. 37, no. 3, pp. 274 – 284, 2010.

[164] P. Heinl, L. MÃ¼ller, C. KÃ¶rner, R. F. Singer, and F. A. MÃ¼ller, "Cellular tiâ6alâ4v structures with interconnected macro porosity for bone implants fabricated by selective electron beam melting," *Acta Biomaterialia*, vol. 4, no. 5, pp. 1536 – 1544, 2008.

[165] M. Strano, A. Villa, and V. Mussi, "Design and manufacturing of anti-intrusion bars made of aluminium foam filled tubes," *International journal of material forming*, vol. 6, no. 1, pp. 153–164, 2013.

[166] B. v. Rietbergen, A. Odgaard, J. Kabel, and R. Huiskes, "Relationships between bone morphology and bone elastic properties can be accurately quantified using high-resolution computer reconstructions," *Journal of Orthopaedic Research*, vol. 16, pp. 23 – 28, 1998.

[167] L. Rincón-Kohli, *Identification of a multiaxial failure criterion for human trabecular bone*. PhD thesis, École Polytechnique Fédérale de Laussanne, 2003.

[168] S. A. Goldstein, R. Goulet, and D. McCubbrey, "Measurement and significance of three-dimensional architecture to the mechanical integrity of trabecular bone," *Calcified Tissue International*, vol. 53, pp. 127 – 133, 1993.

[169] R. W. Goulet, S. A. Goldstein, M. J. Ciarelli, J. L. Kuhn, M. B. Brown, and L. A. Feldkamp, "The relationship between the structural and orthogonal compressive properties of trabecular bone," *Journal of Biomechanics*, vol. 27, no. 4, pp. 375 – 389, 1994.

[170] A. Odgaard, *Bone Mechanics*, ch. Quantification of Cancellous Bone Architecture, pp. 14–1 – 14–19. CRC Press LLC, 2001.

[171] F. BaumgÃ¤rtner, I. Duarte, and J. Banhart, "Industrialization of powder compact foaming process," *Advanced Engineering Materials*, vol. 2, no. 4, pp. 168 – 174, 2000.

[172] J. Banhart, "Manufacture, characterisation and application of cellular metals and metal foams," *Progress in Materials Science*, vol. 46, no. 6, pp. 559 – 632, 2001.

[173] D. Lehmhus, C. Marschner, J. Banhart, and H. Bomas, "Influence of heat treatment on compression fatigue of aluminium foams," *Journal of materials science*, vol. 37, no. 16, pp. 3447–3451, 2002.

[174] D. Lehmhus, J. Banhart, and M. A. Rodriguez-Perez, "Adaptation of aluminium foam properties by means of precipitation hardening," *Materials Science and Technology*, vol. 18, no. 5, pp. 474–479, 2002.

[175] D. Lehmhus and J. Banhart, "Properties of heat-treated aluminium foams," *Materials Science and Engineering: A*, vol. 349, no. 1, pp. 98–110, 2003.

[176] T. M. Keaveny, T. P. Pinilla, R. P. Crawford, D. L. Kopperdahl, and A. Lou, "Systematic and random errors in compression testing of trabecular bone," *Journal of Orthopaedic Research*, vol. 15, no. 1, pp. 101 – 110, 1997.

[177] J. D. Currey, "The effects of drying and re-wetting on some mechanical properties of cortical bone," *Journal of biomechanics*, vol. 21, no. 5, pp. 439–441, 1988.

[178] J. Currey, "Measurement of the mechanical properties of bone: a recent history," *Clinical Orthopaedics and Related Research®*, vol. 467, no. 8, pp. 1948–1954, 2009.

[179] M. Abramoff, P. Magelhaes, and S. Ram, "Image processing with imagej," *Biophotonics International*, vol. 11, no. 7, pp. 36 – 42, 2004.

[180] M. Doube, M. M. Kłosowski, I. Arganda-Carreras, C. F. P., R. P. Dougherty, J. S. Jackson, B. Schmid, J. R. Hutchinson, and S. J. Shefelbine, "BoneJ: Free and extensible bone image analysis in ImageJ," *Bone*, vol. 47, no. 6, pp. 1076 – 1079, 2010.

[181] N. Otsu, "A threshold selection method from gray-level histograms," *IEEE Transactions on Systems, Man, and Cybernetics*, vol. 9, no. 1, pp. 62 – 66, 1979.

[182] W. E. Lorensen and H. E. Cline, "Marching cubes: A high-resolution 3d surface construction algorithm," *SIGGRAPH Comput. Graph.*, vol. 21, no. 4, pp. 163 – 169, 1987.

[183] C. Geuzaine and J.-F. Remacle, "Gmsh: A 3-d finite element mesh generator with built-in pre- and post-processing facilities," *International Journal for Numerical Methods in Engineering*, vol. 79, pp. 1309 – 1331, 2009.

[184] P. Cignoni, M. Callieri, M. Corsini, M. Dellepiane, F. Ganovelli, and G. Ranzuglia, "Meshlab: an open-source mesh processing tool," pp. 129 – 136, The Eurographics Association, 2008.

[185] GeomagicsDesingX, *User Guide, Geomagics XOS*. 3D Systems, Inc., 2013.

[186] D. SystÃ¨mes, *Abaqus v6.12 DocumentationâABAQUS Analysis User's Manual*. ABAQUS Inc, 2012. ISBN 3-900051-07-0.

[187] B. Jähne, *Digital Image Processing*. Springer-Verlag Berlin Heidelberg New York, 2005.

[188] R Development Core Team, *R: A Language and Environment for Statistical Computing*. R Foundation for Statistical Computing, Vienna, Austria, 2008. ISBN 3-900051-07-0.

[189] L. H. Le, C. Zhang, D. Ta, and E. Lou, "Measurement of tortuosity in aluminum foams using airborne ultrasound," *Ultrasonics*, vol. 50, no. 1, pp. 1 – 5, 2010.

[190] G. G. Moraes, I. E. F. Pozzobom, and A. P. Fernandes, Novaes de Oliveira, "Mgal2o4 foams obtained by combustion synthesis," *Chemical Engineering Transaction*, vol. 43, 2015.

[191] V. KrÃ¡lÃk and J. NÄmeÄek, "Comparison of nanoindentation techniques for local mechanical quantification of aluminium alloy," *Materials Science and Engineering: A*, vol. 618, pp. 118 – 128, 2014.

[192] P. K. Zysset, E. X. Guo, E. C. Hoffler, K. E. Moore, and S. A. Goldstein, "Elastic modulus and hardness of cortical and trabecular bone lamellae measured by nanoindentation in the human femur," *Journal of Biomechanics*, vol. 32, no. 10, pp. 1005 – 1012, 1999.

[193] J. N. Grima and R. Caruana-Gauci, "Mechanical metamaterials: materials that push back," *Nature materials*, vol. 11, no. 7, pp. 565–566, 2012.

[194] X. Zheng, H. Lee, T. H. Weisgraber, M. Shusteff, J. DeOtte, E. B. Duoss, J. D. Kuntz, M. M. Biener, Q. Ge, J. A. Jackson, *et al.*, "Ultralight, ultrastiff mechanical metamaterials," *Science*, vol. 344, no. 6190, pp. 1373–1377, 2014.

[195] M. Kadic, T. Bückmann, N. Stenger, M. Thiel, and M. Wegener, "On the practicability of pentamode mechanical metamaterials," *Applied Physics Letters*, vol. 100, no. 19, p. 191901, 2012.

[196] J. T. Overvelde and K. Bertoldi, "Relating pore shape to the non-linear response of periodic elastomeric structures," *Journal of the Mechanics and Physics of Solids*, vol. 64, pp. 351–366, 2014.

[197] J. T. B. Overvelde, S. Shan, and K. Bertoldi, "Compaction through buckling in 2d periodic, soft and porous structures: effect of pore shape," *Advanced Materials*, vol. 24, no. 17, pp. 2337–2342, 2012.

[198] S. Janbaz, H. Weinans, and A. A. Zadpoor, "Geometry-based control of instability patterns in cellular soft matter," *RSC Advances*, vol. 6, no. 24, pp. 20431–20436, 2016.

[199] R. Hedayati, A. Leeflang, and A. Zadpoor, "Additively manufactured metallic pentamode meta-materials," *Applied Physics Letters*, vol. 110, no. 9, p. 091905, 2017.

[200] J. Whitty, F. Nazare, and A. Alderson, "Modelling the effects of density variations on the in-plane poisson's ratios and young's moduli of periodic conventional and re-entrant honeycombs–part 1: Rib thickness variations," *Cellular polymers*, vol. 21, no. 2, pp. 69–98, 2002.

[201] D. Yang, S. Lee, and F. Huang, "Geometric effects on micropolar elastic honeycomb structure with negative poisson's ratio using the finite element method," *Finite elements in analysis and design*, vol. 39, no. 3, pp. 187–205, 2003.

[202] H. Wan, H. Ohtaki, S. Kotosaka, and G. Hu, "A study of negative poisson's ratios in auxetic honeycombs based on a large deflection model," *European Journal of Mechanics-A/Solids*, vol. 23, no. 1, pp. 95–106, 2004.

[203] A. Alderson, J. Rasburn, S. Ameer-Beg, P. G. Mullarkey, W. Perrie, and K. E. Evans, "An auxetic filter: a tuneable filter displaying enhanced size selectivity or defouling properties," *Industrial & engineering chemistry research*, vol. 39, no. 3, pp. 654–665, 2000.

[204] R. Gatt, D. Attard, P.-S. Farrugia, K. M. Azzopardi, L. Mizzi, J.-P. Brincat, and J. N. Grima, "A realistic generic model for anti-tetrachiral systems," *physica status solidi (b)*, vol. 250, no. 10, pp. 2012–2019, 2013.

[205] K. Wang, Y.-H. Chang, Y. Chen, C. Zhang, and B. Wang, "Designable dual-material auxetic metamaterials using three-dimensional printing," *Materials & Design*, vol. 67, pp. 159–164, 2015.

[206] K. R. Olympio and F. Gandhi, "Zero poissonâs ratio cellular honeycombs for flex skins undergoing one-dimensional morphing," *Journal of intelligent material systems and structures*, vol. 21, no. 17, pp. 1737–1753, 2010.

[207] K. K. Saxena, R. Das, and E. P. Calius, "Three decades of auxetics research- materials with negative poisson's ratio: a review," *Advanced Engineering Materials*, vol. 18, no. 11, pp. 1847–1870, 2016.

[208] Y. Prawoto, "Seeing auxetic materials from the mechanics point of view: a structural review on the negative poissonâs ratio," *Computational Materials Science*, vol. 58, pp. 140–153, 2012.

[209] B. Florijn, C. Coulais, and M. van Hecke, "Programmable mechanical metamaterials," *Physical review letters*, vol. 113, no. 17, p. 175503, 2014.

[210] M. Mirzaali, R. Hedayati, P. Vena, L. Vergani, M. Strano, and A. Zadpoor, "Rational design of soft mechanical metamaterials: Independent tailoring of elastic properties with randomness," *Applied Physics Letters*, vol. 111, no. 5, p. 051903, 2017.

[211] Y. Chen, T. Li, F. Scarpa, and L. Wang, "Lattice metamaterials with mechanically tunable poissonâs ratio for vibration control," *Physical Review Applied*, vol. 7, no. 2, p. 024012, 2017.

[212] T. Li, X. Hu, Y. Chen, and L. Wang, "Harnessing out-of-plane deformation to design 3d architected lattice metamaterials with tunable poissonâs ratio," *Scientific Reports*, vol. 7, p. 8949, 2017.

[213] R. M. Neville, F. Scarpa, and A. Pirrera, "Shape morphing kirigami mechanical metamaterials," *Scientific reports*, vol. 6, p. 31067, 2016.

[214] Y. Cho, J.-H. Shin, A. Costa, T. A. Kim, V. Kunin, J. Li, S. Y. Lee, S. Yang, H. N. Han, I.-S. Choi, *et al.*, "Engineering the shape and structure of materials by fractal cut," *Proceedings of the National Academy of Sciences*, vol. 111, no. 49, pp. 17390–17395, 2014.

[215] R. M. Neville, J. Chen, X. Guo, F. Zhang, W. Wang, Y. Dobah, F. Scarpa, J. Leng, and H.-X. Peng, "A kirigami shape memory polymer honeycomb concept for deployment," *Smart Materials and Structures*, vol. 26, no. 5, p. 05LT03, 2017.

[216] J. Hu, Y. Zhou, Z. Liu, and T. Y. Ng, "Pattern switching in soft cellular structures and hydrogel-elastomer composite materials under compression," *Polymers*, vol. 9, no. 6, p. 229, 2017.

[217] R. H. Baughman, "Auxetic materials: Avoiding the shrink," *Nature*, vol. 425, no. 6959, pp. 667–667, 2003.

[218] C. Laschi and M. Cianchetti, "Soft robotics: New perspectives for robot bodyware and control," *Frontiers in Bioengineering and Biotechnology*, vol. 2, p. 3, 2014.

[219] A. G. Mark, S. Palagi, T. Qiu, and P. Fischer, "Auxetic metamaterial simplifies soft robot design," in *Robotics and Automation (ICRA), 2016 IEEE International Conference on*, pp. 4951–4956, Ieee, 2016.

[220] L. N. Awad, J. Bae, K. O'Donnell, S. M. M. De Rossi, K. Hendron, L. H. Sloot, P. Kudzia, S. Allen, K. G. Holt, T. D. Ellis, and C. J. Walsh, "A soft robotic exosuit improves walking in patients after stroke," *Science Translational Medicine*, vol. 9, no. 400, 2017.

[221] C. Coulais, E. Teomy, K. de Reus, Y. Shokef, and M. van Hecke, "Combinatorial design of textured mechanical metamaterials," *arXiv preprint arXiv:1608.00625*, 2016.

[222] B. Charlot, W. Sun, K. Yamashita, H. Fujita, and H. Toshiyoshi, "In-plane bistable nanowire for memory devices," in *Design, Test, Integration and Packaging of MEMS/MOEMS, 2008. MEMS/MOEMS 2008. Symposium on*, pp. 254–258, IEEE, 2008.

[223] M. Konaković, K. Crane, B. Deng, S. Bouaziz, D. Piker, and M. Pauly, "Beyond developable: computational design and fabrication with auxetic materials," *ACM Transactions on Graphics (TOG)*, vol. 35, no. 4, p. 89, 2016.

[224] L. J. Gibson and M. F. Ashby, *Cellular solids: structure and properties*. Cambridge university press, 1999.

[225] M. Bianchi, F. Scarpa, and C. Smith, "Shape memory behaviour in auxetic foams: mechanical properties," *Acta Materialia*, vol. 58, no. 3, pp. 858–865, 2010.

[226] J. Rossiter, K. Takashima, F. Scarpa, P. Walters, and T. Mukai, "Shape memory polymer hexachiral auxetic structures with tunable stiffness," *Smart Materials and Structures*, vol. 23, no. 4, p. 045007, 2014.

[227] S. Janbaz, R. Hedayati, and A. A. Zadpoor, "Programming the shape-shifting of flat soft matter: from self-rolling/self-twisting materials to self-folding origami," *Materials Horizons*, vol. 3, no. 6, pp. 536–547, 2016.

[228] T. van Manen, S. Janbaz, and A. A. Zadpoor, "Programming 2d/3d shape-shifting with hobbyist 3d printers," *Materials Horizons*, 2017.

[229] B. Mota and S. Herculano-Houzel, "Cortical folding scales universally with surface area and thickness, not number of neurons," *Science*, vol. 349, no. 6243, pp. 74–77, 2015.

[230] H. Furuya, H. Kobayashi, S. Pellegrino, K. Horikawa, Y. Morita, M. Nakazawa, I. Ario, A. Watson, C. H. Jenkins, J. J. Larsen, *et al.*, "Deployable structures and biological morphology," 2008.

[231] A. Baimova, E. Korznikova, S. Dmitriev, B. Liu, and K. Zhou, "Review on crumpled graphene: Unique mechanical properties.," *Reviews on Advanced Materials Science*, vol. 39, no. 1, 2014.

[232] M. Habibi, M. Adda-Bedia, and D. Bonn, "Effect of material properties on the crumpling of a thin sheet," *Soft Matter*, 2017.

[233] D. L. Blair and A. Kudrolli, "Geometry of crumpled paper," *Physical review letters*, vol. 94, no. 16, p. 166107, 2005.

[234] C. A. Andresen, A. Hansen, and J. Schmittbuhl, "Ridge network in crumpled paper," *Physical review E*, vol. 76, no. 2, p. 026108, 2007.

[235] A. S. Balankin, A. H. Rangel, G. G. Pérez, F. G. Martinez, H. S. Chavez, and C. L. Martínez-González, "Fractal features of a crumpling network in randomly folded thin matter and mechanics of sheet crushing," *Physical Review E*, vol. 87, no. 5, p. 052806, 2013.

[236] S. Deboeuf, E. Katzav, A. Boudaoud, D. Bonn, and M. Adda-Bedia, "Comparative study of crumpling and folding of thin sheets," *Physical review letters*, vol. 110, no. 10, p. 104301, 2013.

[237] E. Korznikova, J. Baimova, S. Dmitriev, A. Korznikov, and R. Mulyukov, "Mechanical behavior of crumpled sheet materials subjected to uniaxial compression," *Reviews on Advanced Materials Science*, vol. 39, no. 1, 2014.

[238] A. S. Balankin, M. M. Cruz, L. A. Caracheo, O. S. Huerta, C. D. Rivas, C. Martínez, D. S. Ochoa, L. M. Ruiz, S. M. Gutiérrez, J. P. Ortiz, *et al.*, "Mechanical properties and relaxation behavior of crumpled aluminum foils," *Journal of Materials Science*, vol. 50, no. 13, pp. 4749–4761, 2015.

[239] P. Kang, M. C. Wang, P. M. Knapp, and S. Nam, "Crumpled graphene photodetector with enhanced, strain-tunable, and wavelength-selective photoresponsivity," *Advanced Materials*, vol. 28, no. 23, pp. 4639–4645, 2016.

[240] M. F. Griffin, P. E. Butler, A. M. Seifalian, and D. M. Kalaskar, "Control of stem cell fate by engineering their micro and nanoenvironment," *World journal of stem cells*, vol. 7, no. 1, p. 37, 2015.

[241] I. Arganda-Carreras, R. Fernández-González, A. Muñoz-Barrutia, and C. Ortiz-De-Solorzano, "3d reconstruction of histological sections: application to mammary gland tissue," *Microscopy research and technique*, vol. 73, no. 11, pp. 1019–1029, 2010.

[242] A. S. Balankin and O. S. Huerta, "Entropic rigidity of a crumpling network in a randomly folded thin sheet," *Physical Review E*, vol. 77, no. 5, p. 051124, 2008.

[243] M. R. Shaebani, J. Najafi, A. Farnudi, D. Bonn, and M. Habibi, "Compaction of quasi-one-dimensional elastoplastic materials," *Nature Communications*, vol. 8, 2017.

[244] M. L. Delignette-Muller and C. Dutang, "fitdistrplus: An R package for fitting distributions," *Journal of Statistical Software*, vol. 64, no. 4, pp. 1–34, 2015.

[245] T. Tallinen, J. Åström, and J. Timonen, "The effect of plasticity in crumpling of thin sheets," *Nature materials*, vol. 8, no. 1, pp. 25–29, 2009.